

Old Dominion University

## ODU Digital Commons

---

Chemistry & Biochemistry Theses & Dissertations

Chemistry & Biochemistry


---

Summer 2017

# Observations of Greenhouse Gas Isotopologues with ACE-FTS and WACCM

Eric Michael Buzan  
*Old Dominion University*

Follow this and additional works at: [https://digitalcommons.odu.edu/chemistry\\_etds](https://digitalcommons.odu.edu/chemistry_etds)

 Part of the [Atmospheric Sciences Commons](#), [Environmental Chemistry Commons](#), and the [Environmental Sciences Commons](#)

---

### Recommended Citation

Buzan, Eric M.. "Observations of Greenhouse Gas Isotopologues with ACE-FTS and WACCM" (2017). Doctor of Philosophy (PhD), dissertation, Chemistry and Biochemistry, Old Dominion University, DOI: 10.25777/hjtz-s745  
[https://digitalcommons.odu.edu/chemistry\\_etds/44](https://digitalcommons.odu.edu/chemistry_etds/44)

This Dissertation is brought to you for free and open access by the Chemistry & Biochemistry at ODU Digital Commons. It has been accepted for inclusion in Chemistry & Biochemistry Theses & Dissertations by an authorized administrator of ODU Digital Commons. For more information, please contact [digitalcommons@odu.edu](mailto:digitalcommons@odu.edu).

**OBSERVATIONS OF GREENHOUSE GAS ISOTOPOLOGUES**

**WITH ACE-FTS AND WACCM**

by

Eric Michael Buzan  
B.S. May 2011, Old Dominion University

A Dissertation Submitted to the Faculty of  
Old Dominion University in Partial Fulfillment of the  
Requirements for the Degree of

DOCTOR OF PHILOSOPHY

CHEMISTRY

OLD DOMINION UNIVERSITY  
August 2017

Approved by:

Peter Bernath (Director)

Ken Brown (Member)

John Cooper (Member)

John Donat (Member)

Charles Sukenik (Member)

## **ABSTRACT**

### **OBSERVATIONS OF GREENHOUSE GAS ISOTOPOLOGUES WITH ACE-FTS AND WACCM**

Eric Michael Buzan  
Old Dominion University, 2017  
Director: Dr. Peter Bernath

Increases in greenhouse gas concentrations in the atmosphere are the major driver of climate change. Quantifying the sources and sinks of these gases is a major focus of research. Measuring isotopologues, or molecules that differ in isotopic composition, is one useful way of constraining the budget of a molecule as they are highly sensitive to different sources and sinks. However, measurements above the surface have been restricted to a few locations and have only reached the lower stratosphere. Satellite-based remote sensing can achieve nearly global measurement coverage, but so far no satellites have measured isotopologues.

Presented here are measurements of isotopologues of CH<sub>4</sub>, CO, CO<sub>2</sub>, and N<sub>2</sub>O in the stratosphere and mesosphere collected using the Atmospheric Chemistry Experiment Fourier transform spectrometer (ACE-FTS). These measurements are complemented by model runs using the Whole Atmosphere Community Climate Model (WACCM). Both data sets show the strong influence of transport in the upper atmosphere on the isotopic distribution of these molecules. In addition, WACCM accurately calculates the abundances of isotopologues previously measured via balloon and aircraft. These data sets show the usefulness of satellite-based measurements of isotopologues in the upper atmosphere.

## TABLE OF CONTENTS

	Page
LIST OF TABLES.....	v
LIST OF FIGURES.....	vi
Chapter	
1. INTRODUCTION .....	1
2. SCIENCE BACKGROUND .....	3
2.1. Atmospheric structure and composition.....	3
2.2. Atmospheric circulation.....	5
2.3. Isotope chemistry .....	12
3. THE ATMOSPHERIC CHEMISTRY EXPERIMENT .....	17
3.1. Measuring the atmosphere .....	17
3.2. Fourier transform spectroscopy.....	19
3.3. Overview of ACE .....	21
3.4. The ACE-FTS Instrument.....	24
3.5. ACE-FTS data analysis .....	25
4. ATMOSPHERIC MODELING.....	30
4.1. Introduction .....	30
4.2. The box model.....	30
4.3. Multi-box models .....	32
4.4. Multi-dimensional models.....	33
4.5. The Whole Atmosphere Community Climate Model .....	35
5. METHANE ISOTOPOLOGUES IN THE STRATOSPHERE .....	37
5.1. Introduction .....	37
5.2. Methods.....	39
5.3. Results .....	43
5.4. Discussion.....	49
5.5. Conclusions .....	62
6. <sup>13</sup> CO MEASUREMENTS IN THE STRATOSPHERE AND MESOSPHERE .....	63
6.1. Introduction .....	63
6.2. Methods.....	66
6.3. Results and Discussion.....	69
6.4. Conclusions .....	77

	Page
7. CO <sub>2</sub> MASS-INDEPENDENT FRACTIONATION IN THE UPPER ATMOSPHERE .....	78
7.1. Introduction .....	78
7.2. Methods.....	83
7.3. Results and Discussion.....	84
7.4. Conclusions .....	92
8 ISOTOPOLOGUES OF N <sub>2</sub> O IN THE STRATOSPHERE.....	93
8.1. Introduction .....	93
8.2. Methods.....	96
8.3. Results and Discussion.....	99
8.4. Conclusions .....	108
9. SUMMARY.....	109
REFERENCES .....	110
APPENDIX .....	131
VITA.....	147

## LIST OF TABLES

Table	Page
1. Mixing ratios of the major gases in Earth's atmosphere.....	4
2. Isotope ratios of recommended standards .....	15
3. List of molecules and isotopologues routinely retrieved by ACE-FTS.....	27
4. Kinetic isotope effect ratios of methane with OH, O <sup>1</sup> D, and Cl .....	38
5. Summary of microwindows used by ACE for retrieval of CH <sub>4</sub> .....	40
6. Reactions and kinetic constants of reactions for the CH <sub>4</sub> WACCM run. ....	42
7. Reactions important to CO isotopic chemistry and corresponding KIE values....	68
8. Summary of CO <sub>2</sub> microwindows used .....	84
9. Summary of triple isotope slopes from the ACE CO <sub>2</sub> dataset .....	89
10. Microwindow summary for N <sub>2</sub> O and its daughter isotopologues.....	96
11. Interfering species for N <sub>2</sub> O and its daughter isotopologues.....	97
12. Summary of N <sub>2</sub> O isotopologue modifications made to WACCM.....	98
13. Microwindow list for CH <sub>4</sub> .....	131
14. Microwindow list for CH <sub>3</sub> D.....	132
15. Microwindow list for <sup>13</sup> CH <sub>4</sub> .....	134
16. Microwindow list for CO .....	135
17. Microwindow list for <sup>13</sup> CO.....	136
18. Microwindow list for CO .....	137
19. Microwindow list for OC <sup>18</sup> O.....	140
20. Microwindow list for OC <sup>17</sup> O.....	141
21. Microwindow list for N <sub>2</sub> O.....	142
22. Microwindow list for N <sup>15</sup> NO ( <sup>15</sup> N <sup>α</sup> ).....	144
23. Microwindow list for <sup>15</sup> NNO ( <sup>15</sup> N <sup>β</sup> ).....	145
24. Microwindow list for N <sub>2</sub> <sup>18</sup> O .....	146

## LIST OF FIGURES

Figure	Page
1. Atmospheric properties as a function of altitude .....	3
2. Illustration of the Coriolis force in the Northern Hemisphere .....	6
3. Diagram of idealized geostrophic flow .....	6
4. Vertical motion caused by non-ideal geostrophic flow.....	7
5. Major tropospheric circulation patterns .....	8
6. Diagram of Brewer-Dobson circulation .....	9
7. The quasi-biennial oscillation as seen over the Equator .....	10
8. The tropical QBO and mid-latitude seasonal winds detected by the High Resolution Doppler Imager (HRDI). .....	11
9. Morse potential and dissociation energy of a C-H/C-D bond .....	13
10. Reaction coordinate diagrams in 3D (left) and 2D (right) for a hydrogen abstraction reaction .....	14
11. Diagram of the parts of a Michelson interferometer.....	19
12. Schematic of ACE with major components labeled .....	22
13. ACE occultation method. ....	23
14. ACE measurement latitude for sunrise and sunset and beta angle as a function of time of year .....	23
15. Internals of ACE-FTS showing the interferometer (left) and input optics (right) .....	24
16. Schematic of ACE-FTS optics.....	25
17. Series of transmission spectra measured by ACE-FTS during one occultation .	26
18. Diagram of a box model .....	30
19. A two-box model. ....	32
20. Isotopic composition of surface methane sources .....	38
21. Location of all ACE CH <sub>4</sub> measurements by season.....	41
22. ACE total CH <sub>4</sub> VMR by season.....	43
23. ACE δD by season. ....	44
24. ACE δ <sup>13</sup> C by season. ....	45

Figure	Page
25. Total CH <sub>4</sub> VMR by season from the ACE-sampled WACCM data set. ....	46
26. δD by season from the ACE-sampled WACCM data set. ....	47
27. δ <sup>13</sup> C by season from the ACE-sampled WACCM data set. ....	48
28. Keeling plots of ACE data for δD (left) and δ <sup>13</sup> C (right) .....	50
29. The difference in δD between ACE and WACCM .....	52
30. The difference in δ <sup>13</sup> C between ACE and WACCM .....	53
31. Results of ACE calibration compared to WACCM.....	55
32. Comparison of δD profiles from ACE before and after calibration, WACCM, and balloon profiles from Röckmann et al. (2011).....	58
33. Comparison of δ <sup>13</sup> C profiles from ACE before and after calibration, WACCM, and balloon profiles from Röckmann et al. (2011).....	59
34. Dominant oxidizing species of CH <sub>4</sub> by location and season (left) and total methane oxidation (right).....	61
35. δ <sup>13</sup> C and δ <sup>18</sup> O isotopic signature of CO sources in the troposphere .....	64
36. Total CO VMR by season from ACE.....	70
37. Seasonal variation of δ <sup>13</sup> CO as a function of latitude observed by ACE.....	71
38. Total CO VMR by season from the full WACCM data set .....	72
39. δ <sup>13</sup> CO by season from the full WACCM data set .....	73
40. Total CO VMR by season from the ACE-sampled WACCM data set .....	74
41. δ <sup>13</sup> CO by season from the ACE-sampled WACCM data set .....	74
42. Residual in δ <sup>13</sup> CO between ACE and WACCM .....	76
43. The Keeling Curve: CO <sub>2</sub> concentration from Mauna Loa Observatory, Hawaii ..	78
44. Three isotope plot of stratospheric CO <sub>2</sub> from several sources .....	82
45. ACE-FTS CO <sub>2</sub> δ <sup>18</sup> O mission average (top) and standard deviation (bottom) by season. ....	86
46. ACE-FTS CO <sub>2</sub> δ <sup>17</sup> O mission average (top) and standard deviation (bottom) by season. ....	86
47. Altitude profiles of CO <sub>2</sub> isotopic abundance in the 60°N - 70°N latitude bin ....	87
48. Triple isotope plots of mesospheric CO <sub>2</sub> by 30° latitude bins.....	88



Figure	Page
49. Triple isotope plots of mesospheric CO <sub>2</sub> by season and hemisphere .....	89
50. ACE δ <sup>18</sup> O compared to previous stratospheric measurements .....	91
51. ACE-FTS δ <sup>15</sup> N <sup>α</sup> (top), δ <sup>15</sup> N <sup>β</sup> (middle), and δ <sup>18</sup> O (bottom) mission median by season. ....	100
52. ACE-FTS δ <sup>15</sup> N <sup>α</sup> (top), δ <sup>15</sup> N <sup>β</sup> (middle), and δ <sup>18</sup> O (bottom) mission standard deviation by season. ....	101
53. WACCM δ <sup>15</sup> N <sup>α</sup> (top), δ <sup>15</sup> N <sup>β</sup> (middle), and δ <sup>18</sup> O (bottom) mean by season. ....	103
54. δ <sup>15</sup> N <sup>β</sup> monthly average from WACCM.....	104
55. Comparison of ACE and WACCM to balloon profiles over Sweden (top), France (middle), and the Equator (bottom) .....	105
56. N <sub>2</sub> O vs CH <sub>4</sub> mixing ratios in the ACE dataset .....	107

## INTRODUCTION

The increase in greenhouse gases due to anthropogenic activity since the beginning of the Industrial Revolution is the major driver of climate change. These gases absorb thermal infrared radiation, trapping it within Earth's atmosphere. Climate change has numerous consequences including increasing temperatures in the troposphere, rising sea levels from the melting of land ice, and ocean acidification from the dissolution of CO<sub>2</sub>.

One of the major focuses of research on greenhouse gases is characterizing their budget of sources and sinks. Most greenhouse gases have both natural and anthropogenic sources. To constrain the budget, measurements of these gases in the atmosphere are crucial. Almost all greenhouse gases are long-lived and so have a near uniform concentration in the troposphere, the lowest layer of the atmosphere.

The long life of these gases also enables them to propagate upward into the higher layers of the atmosphere. Measurements of gases in the upper atmosphere are sparser than those in the troposphere due to the difficulty of sampling and in-situ measurement. Remote sensing, especially from orbiting satellites, is often used to observe the upper atmosphere and is the primary means of obtaining widespread measurement coverage. Modeling is also beneficial as it can be used to analyze reaction studies in the lab and atmospheric measurements.

Additional information can be obtained by measuring the abundance of isotopologues, or molecules that differ in isotopic composition. The different isotopologues of a molecule undergo chemical reactions at different rates, causing their relative abundances to change over time. This information can be further used to constrain atmospheric budgets.

The following research focuses on isotopic measurements in the upper atmosphere of four gases important to the greenhouse effect: CH<sub>4</sub>, CO, CO<sub>2</sub>, and N<sub>2</sub>O. Chapters 1-3 give background information on related science, remote sensing via satellite, and atmospheric modeling. Chapters 4-7 report observations of these four gases from the Atmosphere Chemistry Experiment Fourier transform

spectrometer (ACE-FTS) and modeling results from the Whole Atmosphere Community Climate Model (WACCM) and the significance of these data sets.

## SCIENCE BACKGROUND

### 2.1 Atmospheric structure and composition

A diagram of the vertical temperature and pressure structure of the atmosphere is given in Figure 1. Pressure decreases exponentially with altitude, while temperature shows a more complex structure due to the absorption of sunlight at different altitudes. These changes in temperature mark the edges of the layers of the atmosphere.

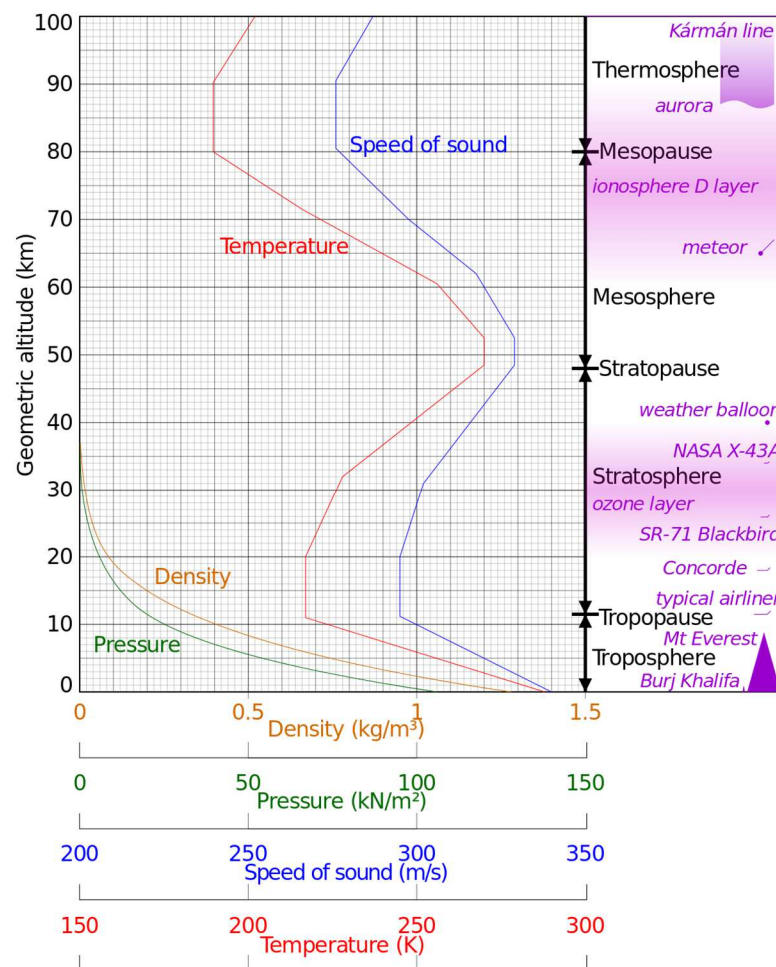


Figure 1: Atmospheric properties as a function of altitude. From CMGLee (2015).

The lowest layer is the troposphere, where the majority of the atmosphere by mass is located. The temperature here decreases up to the tropopause at around 9

km over the poles and 17 km near the Equator. In the next layer, the stratosphere, absorption of ultraviolet light by the ozone layer causes the temperature to increase with altitude. This temperature inversion stratifies the stratosphere, making vertical transport slow. At around 50 km, temperature again decreases through the mesosphere. The coldest temperatures are found at the mesopause, around 85 km. Above there in the thermosphere, temperature increases again in the thermosphere from absorption of vacuum UV (<200 nm) by molecular oxygen and nitrogen.

Table 1: Mixing ratios of the major gases in Earth's atmosphere. Values except for water vapor are given for dry air.

Nitrogen (N <sub>2</sub> )	78.1%	Helium (He)	5.2 ppm
Oxygen (O <sub>2</sub> )	20.9%	Methane (CH <sub>4</sub> )	1.7 ppm
Argon (Ar)	0.93%	Krypton (Kr)	1.1 ppm
Carbon Dioxide (CO <sub>2</sub> )	400 ppm	Hydrogen (H <sub>2</sub> )	0.55 ppm
Neon (Ne)	18 ppm	Nitrous Oxide (N <sub>2</sub> O)	0.32 ppm
Ozone (O <sub>3</sub> )	0.01-10 ppm	Water vapor	0-2%

Table 1 lists the mixing ratios of the most abundant gases in Earth's atmosphere. It is mainly composed of four gases: molecular nitrogen (78% in dry air) and oxygen (21%), argon (1%), and water vapor. A large variety of gases, known as trace gases, are present at the parts per million level to the parts per trillion level and below. Some trace gases not listed above include nitrogen oxides, sulfur oxides and other sulfur compounds, many different volatile organic compounds (VOCs), short-lived radical species, and manmade gases like chlorofluorocarbons (CFCs). Though the concentrations of these gases are very low, they are very important to atmospheric phenomena such as the greenhouse effect, the ozone layer, and pollution.

Gas concentrations are typically reported as a volume mixing ratio (VMR), the fraction of a certain species in air by volume. It can also be reported as a number density, the number of atoms or molecules per spatial volume. Number density is affected by the pressure of the gas, while mixing ratio is not.

Some gases such as  $N_2$  and argon are inert in most parts of the atmosphere and so have a constant VMR in these areas, while others can vary by location and altitude. The concentration of water vapor is highly dependent on temperature; at the surface, a mixing ratio of 1% is possible, while in the colder stratosphere and mesosphere water vapor is a trace gas. Ozone concentrations are controlled by photolysis; it is most abundant in the middle stratosphere in the ozone layer. Methane and other organic compounds oxidize in the atmosphere and have decreasing mixing ratios with altitude. In the thermosphere, the high levels of UV radiation photolyze many gases, producing exotic species like atomic oxygen and nitrogen and ions.

## **2.2 Atmospheric circulation**

The concentration and distribution of atmospheric gases are controlled by two broad categories: chemistry and circulation. Chemistry is specific to each molecule and will be discussing in subsequent chapters. Circulation, the physical movement of air masses, affects all gases equally.

### *2.2.1 Tropospheric circulation*

Since the Earth is a rotating system, horizontally moving air is deflected by an apparent force called the Coriolis force. Consider the Northern Hemisphere, where the Earth rotates counterclockwise as seen from overhead, and an air mass moving toward the Equator. When it begins moving, the air has a certain eastward velocity that does not change as it moves. However, Earth's surface is moving faster closer to the Equator, so from the surface the air appears to curve to the west, or right. Figure 2 illustrates this effect. A poleward moving air mass moves faster than the surface as it travels north, so it appears to curve east, also to the right. In the Southern Hemisphere, the directions are reversed and air deflects to the left.

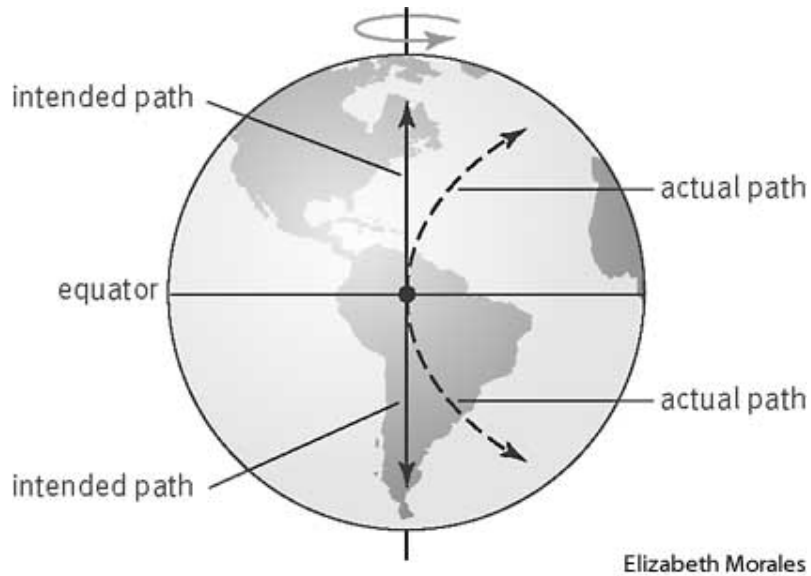


Figure 2: Illustration of the Coriolis force in the Northern Hemisphere. From Hall et al. (2013).

Air masses also move along pressure gradients from high to low pressure. However, once it begins to move, it also incurs a Coriolis force. Eventually the two forces balance when the air mass moves perpendicularly to the pressure gradient; the Coriolis force pulls on the right side and pressure on the left side. This is known as geostrophic flow, shown in Figure 3. In the Northern Hemisphere, air flows counterclockwise around areas of low pressure and clockwise around high pressure.

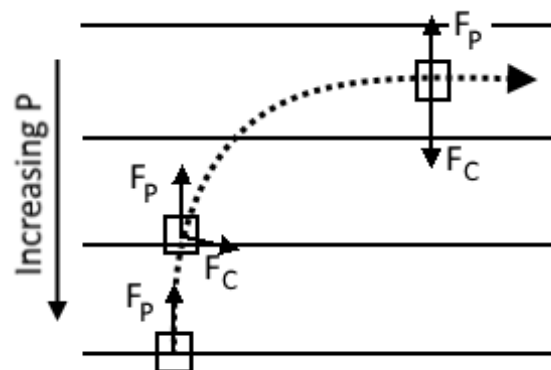


Figure 3: Diagram of idealized geostrophic flow. Adapted from Jacob (2000).

Friction also comes into play near the surface. This weakens the Coriolis force but not the pressure gradient, causing the air to flow partially in the direction of the pressure gradient. This causes air to move vertically in the pressure center; high pressure creates downwelling while low pressure creates upwelling (Figure 4).

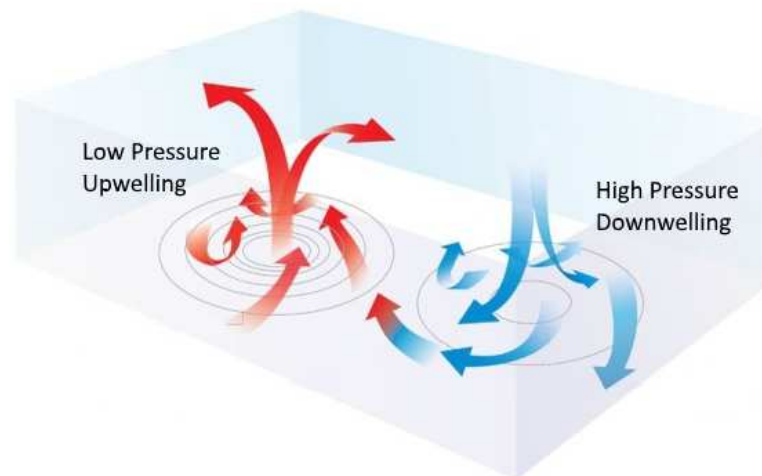


Figure 4: Vertical motion caused by non-ideal geostrophic flow. Adapted from Met Office (2013).

Meridional airflow is largely affected by the temperature difference between the Equator and poles. Warm air at the Equator rises and turns poleward at the top of the troposphere. Without the Coriolis force, this air would flow to the poles before sinking. However, the Coriolis force disrupts this flow, causing the air to sink around 30 degrees before returning toward the Equator. This circulation pattern is known as a Hadley cell. At high latitudes, a similar circulation cell forms from the rising of air around 60 degrees and the sinking of air at the pole. This is a polar cell. In between, a third cell known as the Ferrell cell or mid-latitude cell exists, partially driven by the circulation of the Hadley and polar cells. Air currents within this cell are more complex than the other two, but meridional flow is generally the opposite of the Harley and polar cells: air high in the troposphere moves toward the Equator while surface air moves toward the poles. Figure 5 illustrates the airflow in these cells.



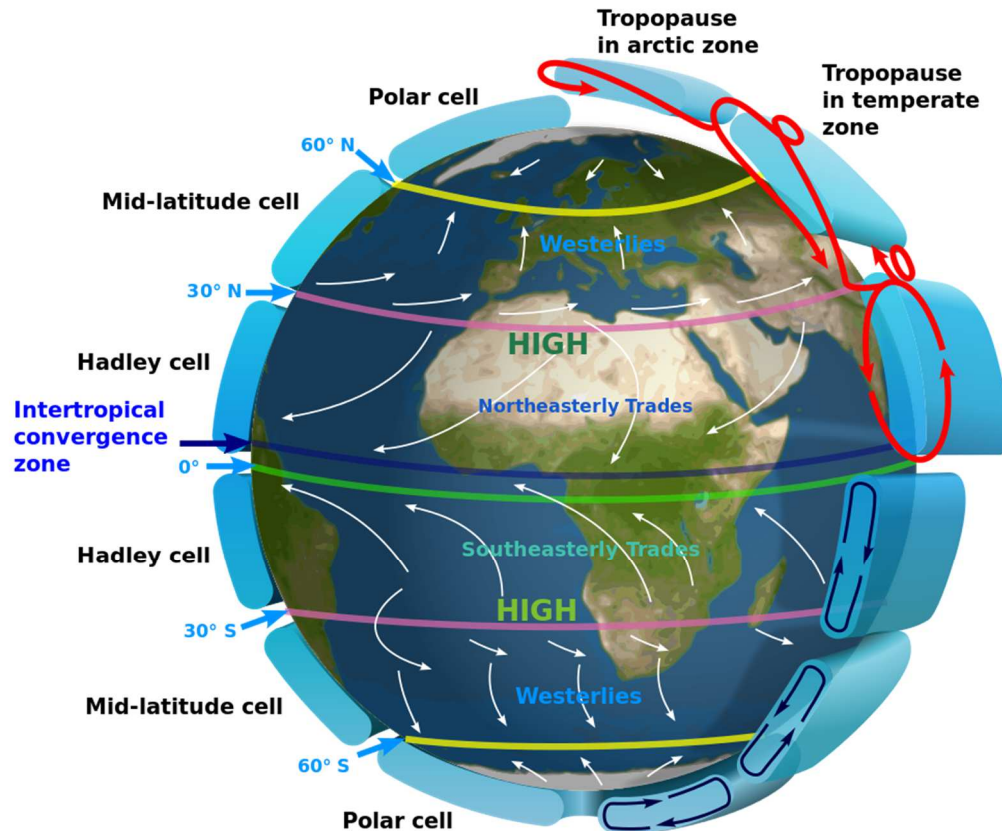


Figure 5: Major tropospheric circulation patterns. From Kaidor (2015).

These circulation cells affect the mixing time of tropospheric air. Longitudinal mixing is the fastest, driven by geostrophic flow within each cell; air can circumnavigate the Earth in a couple weeks. Transport between cells is somewhat slower; mid-latitude air takes 1-2 months to exchange with the poles or tropics. Mixing between the hemispheres is slowest, about 1 year, as there is no thermal forcing across the Equator. Seasonal movement of the Intertropical Convergence Zone between the Hadley cells is the primary driver.

### 2.2.2 Upper atmospheric circulation

The main circulation pattern in the stratosphere is Brewer-Dobson circulation, shown in Figure 6. Similar to the tropospheric cells, air rises from the tropopause over the Equator, moves poleward, then sinks over the higher latitudes. However, the origin of this circulation is more complicated than the thermally-driven

tropospheric cells. The major driver is the dissipation of gravity waves, waves whose restoring force is buoyancy, that originate from the troposphere. Large mountain ranges that force surface air upward are one source of gravity waves. Since mountains are more common in the Northern Hemisphere, Brewer-Dobson circulation is stronger here. There is also a strong seasonal dependence; sinking cold air over the winter pole strengthens the circulation while circulation over the summer pole is very weak (NASA, 2000).

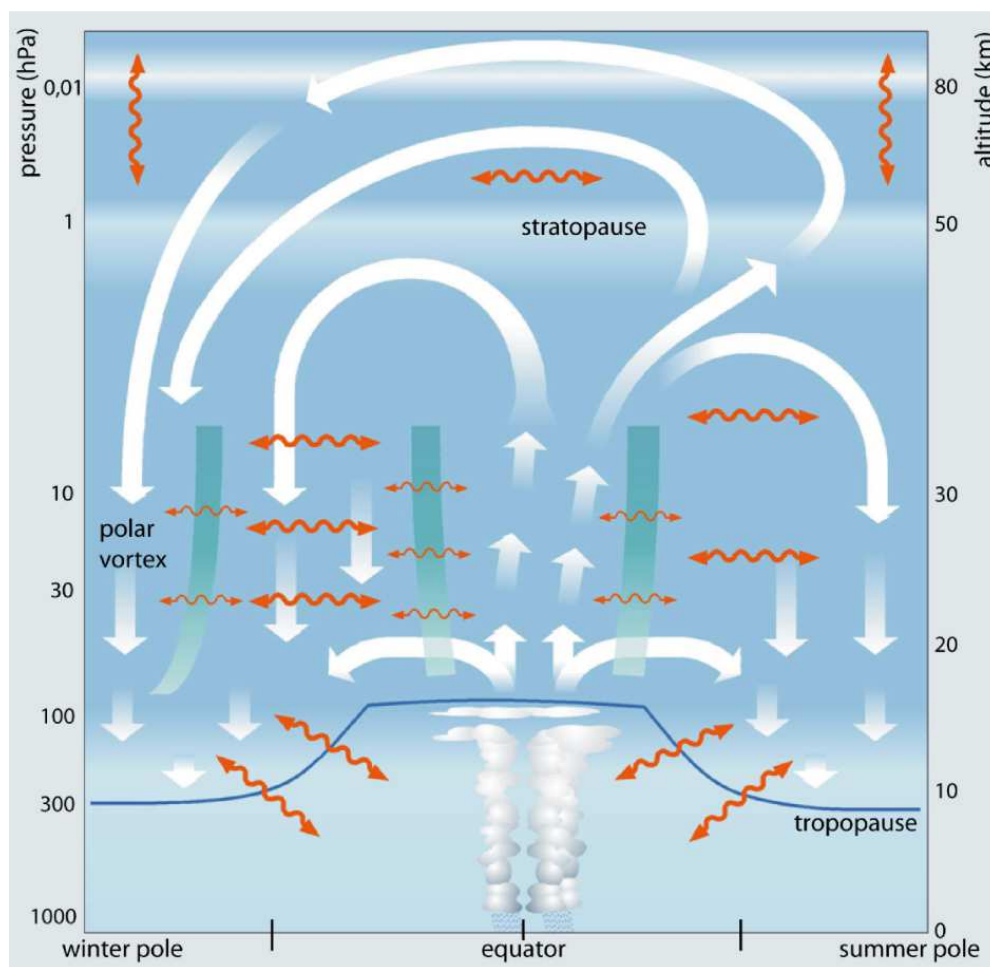


Figure 6: Diagram of Brewer-Dobson circulation. From Bönisch et al. (2011).

Another major stratospheric circulation pattern is the quasi-biennial oscillation (QBO), an east-west oscillation of tropical winds. The oscillation originates from the

upper stratosphere and descends downward over a few months (Figure 7). The QBO is generally observed between 20 and 35 km, with stronger easterly winds than westerly winds. Internal dynamics of tropical gravity waves rather than seasonal variation are the source of the QBO, causing a period ranging from 22 to 34 months. Outside of the tropics, the QBO breaks down and seasonal east-west oscillations of the wind occur (Figure 8). The QBO alters the temperature structure of the tropical stratosphere which affects photochemistry in this region. It also perturbs the Brewer-Dobson circulation; upward motion over the Equator is strengthened during the descending easterlies phase, and the opposite occurs during the descending westerlies phase (NASA, 2000).

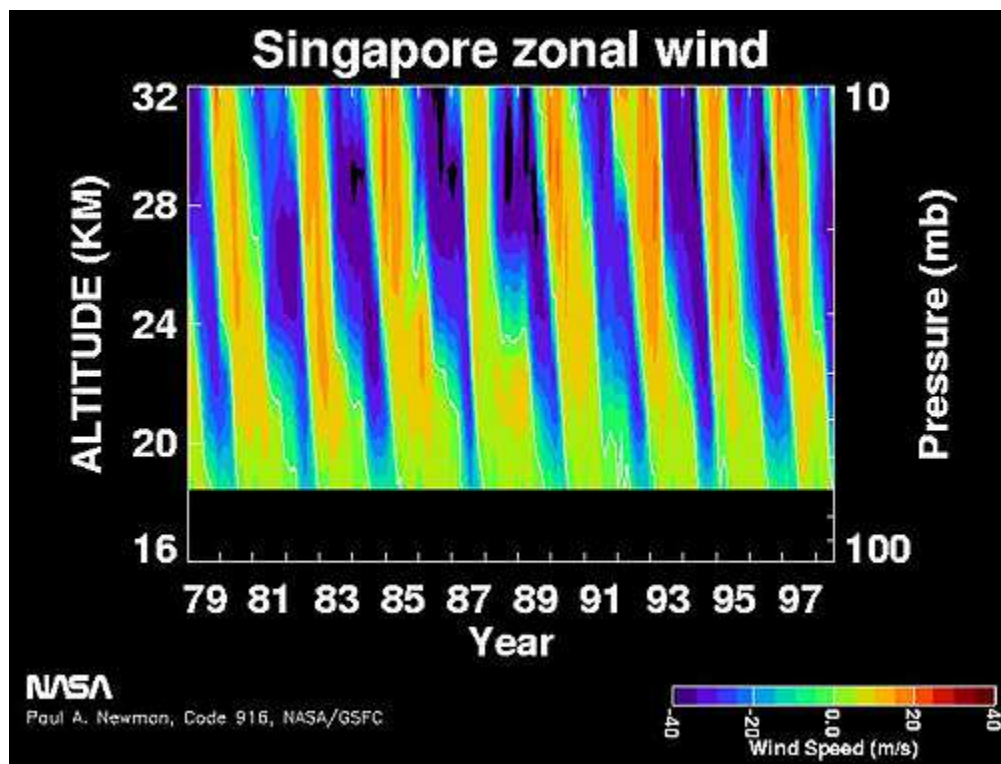


Figure 7: The quasi-biennial oscillation as seen over the Equator. Easterly winds are shown in blue while westerly winds are shown in orange. From NASA (2000).

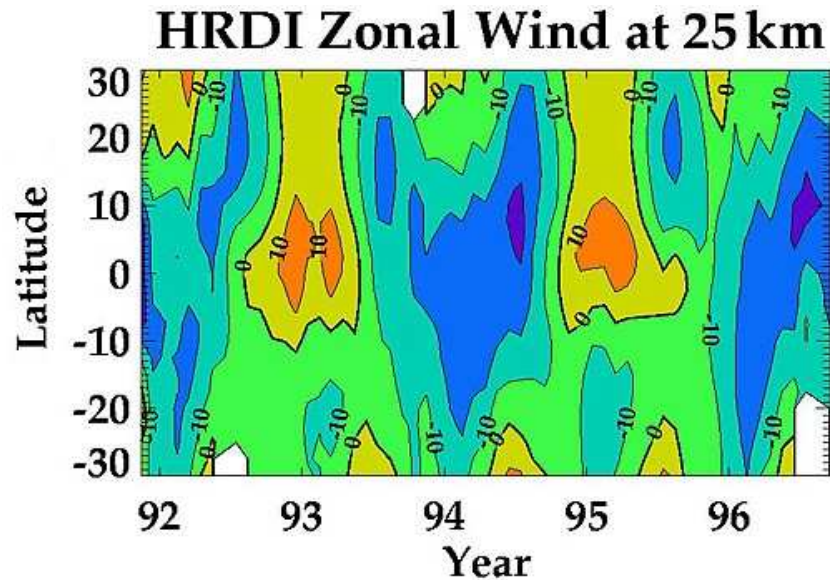


Figure 8: The tropical QBO and mid-latitude seasonal winds detected by the High Resolution Doppler Imager (HRDI). Adapted from NASA (2000).

The final major feature of the stratosphere is the polar vortex. Over the winter pole, strong westerly winds form a vortex that traps air. Temperatures can dip below  $-78\text{ }^{\circ}\text{C}$ , the temperature needed to form polar stratospheric clouds from nitric acid, sulfuric acid, and water. These temperatures and clouds, along with the low amount of sunlight, allow chemistry such as the decomposition of the Cl-containing reservoir molecules HCl and  $\text{ClONO}_2$  to  $\text{Cl}_2$  to occur, while the vortex traps the products. As springtime arrives in each hemisphere, the vortex breaks down, releasing the trapped air mass. In particular, the trapped chlorine catalyzes ozone destruction via the formation of ClO, leading to the annual ozone hole over the Antarctic and depleted ozone over the Arctic.

Mesospheric transport is dominated by a single circulation cell where air rises in the summer hemisphere, travels high to the winter hemisphere, sinks, and returns low to the summer hemisphere. This causes the summer hemisphere to be colder than expected by thermal equilibrium and the winter hemisphere to be warmer (Vincent, 2015).

In the thermosphere, transport is similar to that in the mesosphere with upwelling over the summer pole and downwelling over the winter pole. Energy from

the solar wind and magnetosphere strongly influence these dynamics (Forbes, 2007). In addition, molecular diffusion becomes important; the very thin air allows species to separate by mass. The lightest gases, hydrogen and helium, can escape from the atmosphere.

## **2.3 Isotope chemistry**

Observing the distribution of isotopically-substituted molecules gives additional information about the behavior of a gas in the atmosphere. In the following sections, "isotopologue" is used to refer to a molecule containing one or more heavy isotopes of an atom.

### *2.3.1 The kinetic isotope effect*

The presence of a heavy isotope in a molecule can alter the rate of a reaction. This is known as a kinetic isotope effect (KIE). KIEs are normally reported as a ratio of the rates with and without the heavy isotope. For hydrogen and deuterium, this is denoted as  $k_H/k_D$ , and for carbon-12 and carbon-13, typically  $k_{12}/k_{13}$ . For most reactions, the heavy isotopologue reacts more slowly than the light isotopologue, giving a KIE greater than 1, a normal isotope effect. If the KIE is less than 1, meaning the heavy isotopologue reacts more quickly, it is an inverse isotope effect. Isotope effects that occur at a bond containing a heavy isotope are called primary isotope effects, while those involving bonds adjacent to a heavy isotope are known as secondary isotope effects. In atmospheric reactions, secondary isotope effects are very small and will not be discussed further.

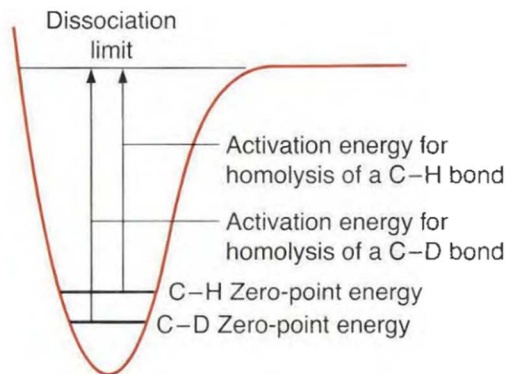


Figure 9: Morse potential and dissociation energy of a C-H/C-D bond. From Anslyn and Dougherty (2006).

The origin of kinetic isotope effects is the difference in vibrational frequencies of a bond due to the presence of a heavy or light isotope. We first consider a simple bond breaking event between a C and an H or D atom. While the potential energy surface of the bond is not affected by isotopic substitution, the vibrational energy levels are. Using a simple diatomic model, the bond's vibrational frequency is inversely proportional to its effective reduced mass:

$$\nu = \frac{1}{2\pi} \sqrt{\frac{k}{m_r}}, \quad m_r = \frac{m_1 m_2}{m_1 + m_2} \quad (1)$$

The zero-point energy, or the energy of the ground vibrational state, is  $e_0 = \frac{1}{2} h\nu$ .

Since the heavier isotopologue has a higher reduced mass, its vibrational frequency and its zero point energy is lower. The result of these equations is shown in Figure 9. The activation energy of the bond breaking reaction is the difference in the zero point and dissociation energies. The heavy isotopologue has a higher energy barrier, so the reaction proceeds more slowly according to the Arrhenius equation:

$$k = A \exp\left(\frac{-E_a}{kT}\right) \quad (2)$$

where  $E_a$  is the activation energy. The above equations can be combined to calculate a theoretical KIE for a reaction. A C-H bond, which has a vibrational frequency of about  $3000 \text{ cm}^{-1}$ , would have a KIE of about 6.5 (Anslyn and Dougherty, 2006).

In reality, the KIEs of reactions are much smaller since bonds are not fully broken at the transition state. For a more realistic picture, we consider a hydrogen abstraction reaction such as  $\text{CH}_4 + \text{OH} \rightarrow \text{CH}_3 + \text{H}_2\text{O}$ . The potential energy surface can be visualized as a reaction coordinate with a series of perpendicular potential energy wells (Figure 10). The activated complex has vibrational modes as shown in each well. Here the energy barrier difference for C-H versus C-D also depends on the zero point energy of the transition state (Anslyn and Dougherty, 2006).

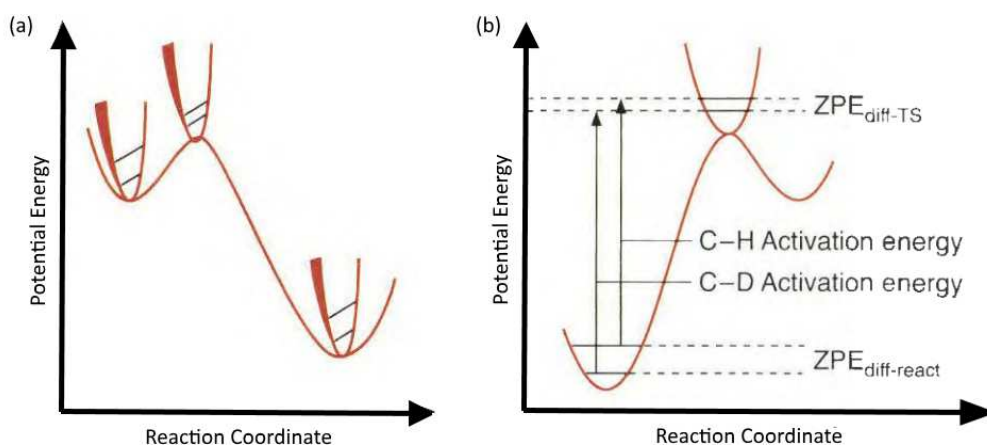


Figure 10: Reaction coordinate diagrams in 3D (left) and 2D (right) for a hydrogen abstraction reaction. From Anslyn and Dougherty (2006).

As the zero point energies of the bonds are affected by the reduced mass, the relative masses of the atom undergoing isotopic substitution has a large effect on the KIE. Substituting H (1 amu) for D (2 amu) approximately doubles the reduced mass, causing the KIE to be large. In contrast, carbon-12 for carbon-13 only increases the reduced mass by about 8%, so the KIE is relatively smaller. Oxygen and nitrogen substitutions yield similarly small KIEs. For example, the  $\text{CH}_4 + \text{OH}$  reaction,  $k_{\text{H}}/k_{\text{D}} = 1.25$  at 298 K (Gierczak et al., 1997), while  $k_{12}/k_{13} = 1.005$  (Burkholder et al., 2015).

### 2.3.2 Reporting isotopologue measurements

Abundances of heavy isotopologues are usually not reported as an absolute concentration but a relative number using delta notation. The formula for delta notation using carbon as an example is:

$$\delta^{13}\text{C} = \left( \frac{R_{\text{samp}}}{R_{\text{std}}} - 1 \right) \times 1000\text{‰} \quad (3)$$

$$R = \frac{[^{13}\text{C}]}{[^{12}\text{C}]} \quad (4)$$

The ratio of the light and heavy isotopologues is compared to that of a standard with a precisely known isotopic composition. Each isotope has one or more standards; the recommended ones and the ones used here are given in Table 2 (Slater et al., 2001). Note that delta values can be negative if the sample is less enriched in the heavy isotopologue compared to the standard. In addition, delta values for different isotopes have no significance compared to each other.  $\delta\text{D}$  in particular has higher ranges of values due to the larger KIEs of D/H. Finally, the value of the isotope ratio used depends on the number of atoms of an element in the molecule. For example, the standard ratio of  $\text{CH}_3\text{D}/\text{CH}_4$  is multiplied by about 4 (though not exactly 4 to account to the existence of multiply-substituted isotopologues).

Table 2: Isotope ratios of recommended standards

Isotope	Standard	Isotope ratio
D/H	Vienna Standard Mean Ocean Water (VSMOW)	$1.5576 \times 10^{-4}$
$^{18}\text{O}/^{16}\text{O}$	Vienna Standard Mean Ocean Water (VSMOW)	$2.00520 \times 10^{-3}$
$^{17}\text{O}/^{16}\text{O}$	Vienna Standard Mean Ocean Water (VSMOW)	$3.73 \times 10^{-4}$
$^{13}\text{C}/^{12}\text{C}$	Pee Dee Belemnite (PDB)	$1.12372 \times 10^{-2}$
$^{15}\text{N}/^{14}\text{N}$	Atmospheric $\text{N}_2$	$3.6765 \times 10^{-3}$



### *2.3.3 Importance of atmospheric isotopic measurements*

One major goal of atmospheric chemistry is to constrain the budgets of gases. Due to the kinetic isotope effect, reactions that involve a given gas will cause it to undergo isotopic fractionation. Therefore, information on isotopic composition is useful for determining the relative strengths of sources and sinks.

For example, each surface source of a gas has its own isotopic signature. Each sink reaction also has its own KIE. In the troposphere, long-lived gases are well-mixed and so have a uniform abundance and isotopic composition. If a gas has no major sinks in this region, the isotopic composition will be the weighted average of the signatures of each of its sources. If a gas has both sources and sinks in a given region, budget determination is not as simple. Nonetheless, the isotopic data is an additional constraint that can be used.

A similar process occurs in the upper atmosphere for gases with only surface sources. Air entering the stratosphere initially has the composition of tropospheric air. Over time, its sinks modify its composition. If the KIEs of all sink reactions are known, their relative strengths can be determined from the measured fractionation of the gas. Since transport in the upper atmosphere is also much slower than in the troposphere, isotopic measurements can be used as sensitive tracers of upper atmospheric circulation patterns.

## THE ATMOSPHERIC CHEMISTRY EXPERIMENT

### 3.1 Measuring the atmosphere

Two major methods are used to measure the chemical composition of the atmosphere. The first method involves direct measurement of air samples. Samples are collected in the field, either on the surface or in the air via balloon or aircraft. They are then analyzed in a laboratory; gas chromatography and mass spectrometry are the most common techniques, though optical spectrometers are also used. Alternatively, the instrument can make continuous measurements in situ. The most famous atmospheric data set is the record of CO<sub>2</sub> from Mauna Loa Observatory in Hawaii, which makes hourly measurements using an infrared spectrometer (Komhyr et al., 1989). Instruments have also been mounted in mobile platforms, such as ships and aircraft. The CARIBIC mission uses instruments carried commercial aircraft to measure the upper troposphere (Brenninkmeijer et al., 2007). Similarly, the TROICA-5 mission made in situ measurements from trains along the Trans-Siberian railroad (Oberlander, 2002). The controlled environment of a laboratory and the use of high-precision techniques such as mass spectrometry produce very precise measurements. However, these measurements are spatially restricted to locations where samples can be physically collected.

The other major method is remote sensing; optical spectrometers are the instrument of choice here. Instruments can be placed in the same locations as those used for direct measurement: on the surface, either stationary or ship-based, or in the air on aircraft or balloons. Observations are made in the microwave, infrared, visible, and ultraviolet regions depending on the target species. Land- and aircraft-based remote sensing gives additional information beyond what is possible with direct sampling such as column density and vertical profiles into the stratosphere and mesosphere. Still, measurements are restricted to the location of the instrument.

Remote sensing can also be performed on orbiting spacecraft. This allows for coverage of large parts of the Earth with a single instrument. The orbital parameters and instrumental setup determine the horizontal and vertical coverage

of the instrument and the frequency at which measurements are made. The main drawbacks of satellite-based instruments are lower sensitivity compared to laboratory techniques and the high cost of placing satellites in orbit.

The orbit of the satellite determines the areas of the Earth the instrument can measure. In a geosynchronous orbit, at an orbital radius of about 35,786 km above Earth's surface, the satellite's orbital period matches the rotational period of Earth so the satellite remains at the same longitude. A special case of this is a geostationary orbit where the satellite has a fixed location over the Equator. Few trace gas observing satellites use this orbit; one example is the European satellite Sentinel 4 (Stark et al., 2013).

Most trace gas observing satellites use low Earth orbits with an altitude of 200 to 2000 km. The orbital period is approximately 90 to 120 minutes and gets longer at high altitudes. The inclination, or tilt of the orbit compared to the equator, can vary from equatorial to polar orbits to change the region of Earth observed at a given time. Certain combinations of altitude and inclinations create a sun-synchronous orbit where the satellite passes over a given point on Earth's surface at the same time each day. A few of the many satellites in low Earth orbit include Envisat, which carried the gas monitoring instruments SCIAMACHY (Bovensmann et al., 1999), MIPAS (Fischer et al., 2008), and GOMOS (Kyrölä et al., 2004); Aura (Schoeberl et al., 2006), carrying HIRDLS, OMI, MLS, and TES, and the MetOp series of satellites (Kramer, 2002).

Satellite instruments can observe the atmosphere in two directions, limb and nadir, each offering different spatial resolutions. Nadir instruments look straight down at the Earth, giving a high horizontal resolution but poor vertical resolution, often just a column density rather than a vertical profile. IASI on MetOp (George et al., 2009) and TES observe in the nadir direction. Limb instruments look across the atmosphere parallel to the ground. This direction gives better vertical resolution but lower horizontal resolution, and clouds are more probable to interfere. Limb sounders can measure continuously or at sunrise and sunset, using the sun as a light source. Instruments that use this viewing geometry include HALOE on UARS (Russell et al., 1993) and MIPAS. A few instruments like SCIAMACHY are able to measure in both the nadir and limb directions.

## 3.2 Fourier transform spectroscopy

### 3.2.1 The Michelson interferometer

When observing in the infrared region, Fourier transform spectrometers are the typical choice for satellites. The main component of an FTS is the Michelson interferometer, shown in Figure 11. Incoming light is split by a beamsplitter; half of the light travels to a movable mirror while the other half travels to a fixed mirror. The returning light is recombined at the beamsplitter and sent to a detector.

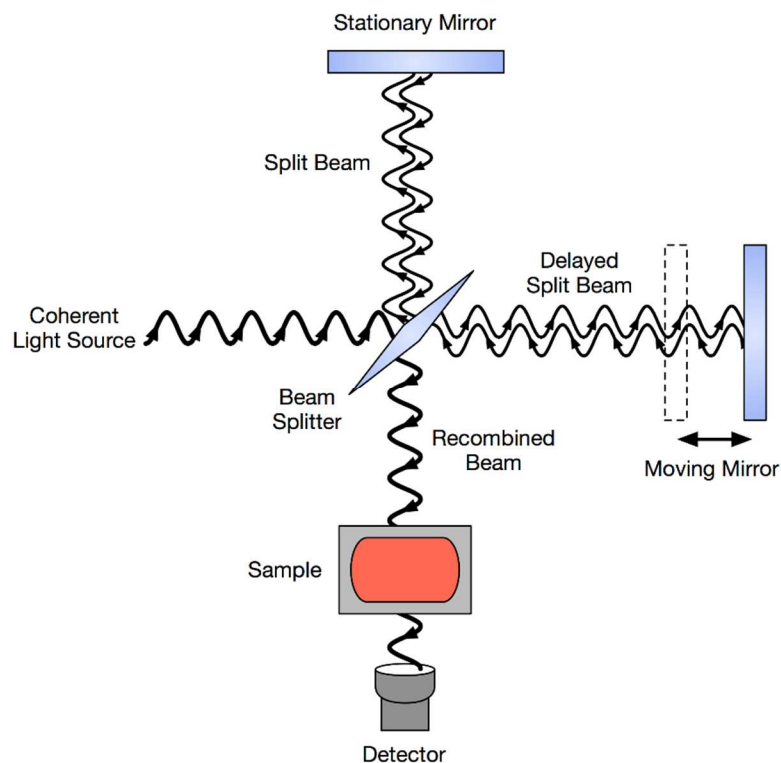


Figure 11: Diagram of the parts of a Michelson interferometer. From Gans (2011).

The two beams of light have traveled different lengths to and from the beamsplitter, the optical path difference (OPD)  $\delta$ . For a monochromatic light source, the two beams interfere constructively when the OPD is an integer multiple

of the wavelength:  $\lambda = 0, \delta, 2\delta, \dots$ . At half-integer OPDs,  $\lambda = \delta/2, 3\delta/2, 5\delta/2, \dots$ , the beams interfere destructively, and no signal is detected. If the movable mirror is smoothly scanned, the detected intensity  $I(\delta)$  varies as a cosine wave. When a broadband light source is considered, the intensity is integrated over the wavenumber range of the light:

$$I(\delta) = \int_0^{\infty} B(\tilde{\nu}) \cos(2\pi\tilde{\nu}\delta) d\tilde{\nu} \quad (5)$$

where  $\tilde{\nu}$  is the wavenumber ( $\text{cm}^{-1}$ ) and  $B(\tilde{\nu})$  is the intensity at that wavenumber. The desired output is not the intensity as a function of OPD (the time domain, as the OPD changes linearly over time) but as a function of wavenumber (the frequency domain). Performing a Fourier transform converts  $I(\delta)$  to  $B(\tilde{\nu})$ :

$$B(\tilde{\nu}) = \int_{-\infty}^{+\infty} I(\delta) \cos(2\pi\tilde{\nu}\delta) d\delta \quad (6)$$

In practice, the limits of integration in Equation 28 are the maximum OPD of the instrument. This determines the resolution of the final spectrum, given by

$$\Delta\tilde{\nu} = \frac{1}{\delta_{max}} \quad (7)$$

Conversely, the resolution of  $I(\delta)$ , controlled by the speed of the moving mirror and data acquisition speed of the detector, determines the spectral range of the final spectrum.

An FTS has some advantages over a traditional spectrometer that uses a diffraction grating or prism. The FTS detects a broad band of light simultaneously, while a grating spectrometer only detects the narrow band of light that is diffracted to the detector. This is known as the multiplex advantage or Fellgett advantage. In addition, a grating spectrometer uses a narrow slit aperture, allowing only a small amount of light from the source to reach the detector. An FTS can use a larger aperture, allowing it to use more of the source light. This is known as the Jacquinot advantage.

### 3.2.2 Lineshape functions

The spectrum of a molecule is made of a large number of spectral features known as lines. In the infrared region, lines are grouped together into bands, corresponding to a particular vibrational transition; each line within a band

corresponds to a particular rotational transition. At high resolution, these lines have a distinct width and lineshape due to various effects. In the atmosphere, lines are primarily broadened by two effects: pressure broadening and Doppler broadening (Bernath, 2016).

Pressure broadening arises from the collision of molecules in a gas. Ignoring collisions, a vibrational mode has an oscillating dipole that can be represented by an infinite sine wave. A strong collision can change the phase of the dipole, breaking the sine wave into finite lengths. Fourier transforming the infinite sine wave gives an infinitely narrow line at the vibration frequency; transforming the finite sine wave broadens the line. Since all molecules in the gas experience a similar collisional environment, pressure broadening results in a homogeneous lineshape function, a Lorentzian:

$$g_P(\nu - \nu_0) = \frac{\Delta\nu_{1/2}/(2\pi)}{(\Delta\nu_{1/2}/2)^2 + (\nu - \nu_0)^2} \quad (8)$$

where  $\nu - \nu_0$  represents the distance from the line center and  $\Delta\nu_{1/2}$  is the full width at half maximum (FWHM).

Doppler broadening results from the velocities of molecules in a gas. The frequency of light absorbed or emitted from molecules moving away or toward the detector is altered by the Doppler Effect. As different molecules move at different velocities, Doppler broadening results in an inhomogeneous lineshape function, a Gaussian:

$$g_D(\nu - \nu_0) = \frac{2}{\Delta\nu_{1/2}} \sqrt{\frac{\ln(2)}{\pi}} \exp\left(-4 \ln 2 \left(\frac{\nu - \nu_0}{\Delta\nu_{1/2}}\right)^2\right) \quad (9)$$

The combination of a Lorentzian and a Gaussian lineshape gives a Voigt lineshape. The Voigt lineshape function typically is able to represent well the lineshape of atmospheric gases.

### 3.3 Overview of ACE

The Atmospheric Chemistry Experiment (ACE), also known as SCISAT, is a Canadian satellite launched in 2003 to perform remote sensing on Earth's Atmosphere. The primary mission objective is to understand the dynamics and chemistry of ozone in the troposphere and stratosphere. The observational

capabilities of ACE have allowed it to study a large number of atmospheric gases in addition to ozone. The ACE mission follows in the footsteps of ATMOS (Atmospheric Trace MOlecule Spectroscopy), an infrared spectrometer that flew onboard four Space Shuttle missions between 1985 and 1994 (Gunson et al., 1996).

ACE carries two major instruments: a high resolution ( $0.02\text{ cm}^{-1}$ ) Fourier transform infrared spectrometer with a spectral range of  $750 - 4400\text{ cm}^{-1}$  and MAESTRO, a dual optical spectrograph that measures  $285 - 550\text{ nm}$  and  $525 - 1020$  primarily for the monitoring of ozone, nitrogen dioxide, and aerosols. ACE also carries a star tracker that assisted in orienting the satellite; it failed in 2015 with no effect on instrument performance (Bernath, 2017). Figure 12 gives a schematic of ACE with these instruments labeled.

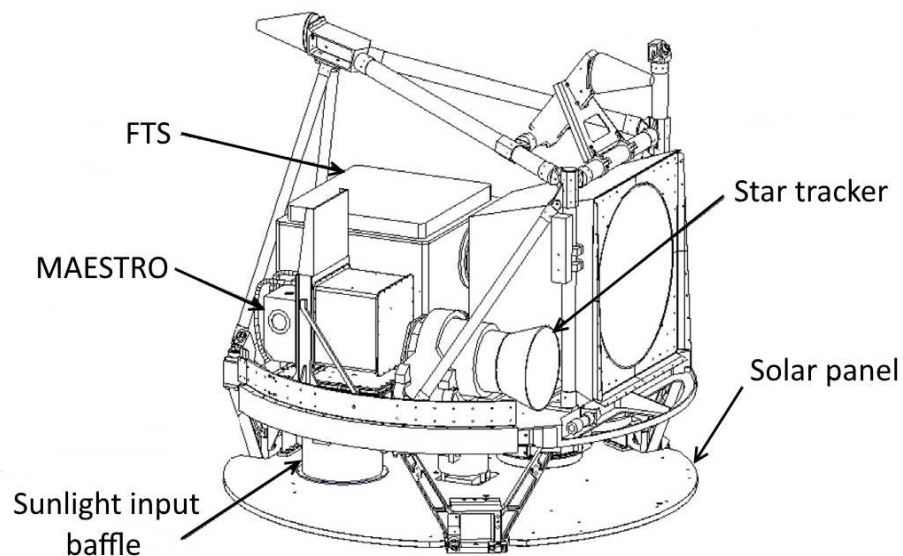


Figure 12: Schematic of ACE with major components labeled. Adapted from Walkty and Kohut (2013).

ACE orbits the Earth at an inclination of  $74^\circ$  and at a height of  $650\text{ km}$ , giving it coverage of the Earth from  $85^\circ\text{S}$  to  $85^\circ\text{N}$ .

The satellite makes limb measurements as its view of the sun passes through the atmosphere (an occultation). A series of infrared spectra are collected, each corresponding to a layer of the atmosphere. (Figure 13) From these spectra, profiles of its target molecules, pressure, and temperature are retrieved (Section

3.5). The satellite has an orbital period of 97.6 minutes, allowing it to make measurements about every 49 minutes. The latitude of the measurement tangent point varies slowly with time (Figure 14) but accumulates a set of global measurements in about two months. The geographic measurement cycle repeats in latitude annually which provides a framework for determining trends as a function of time.

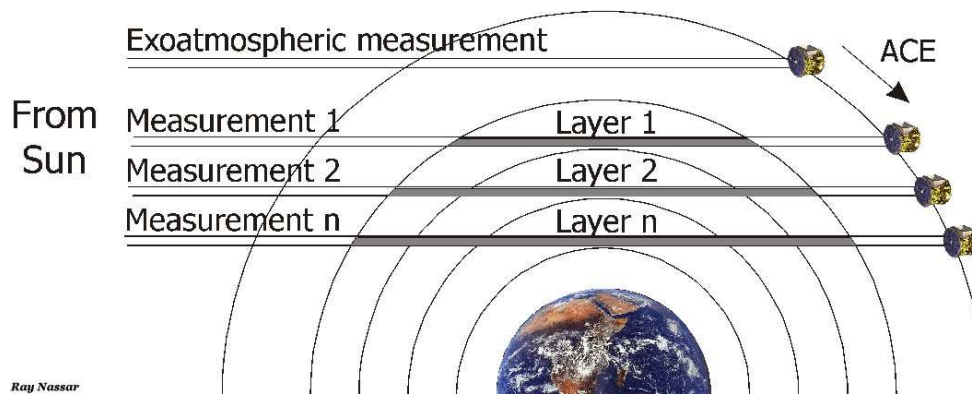


Figure 13: ACE occultation method.

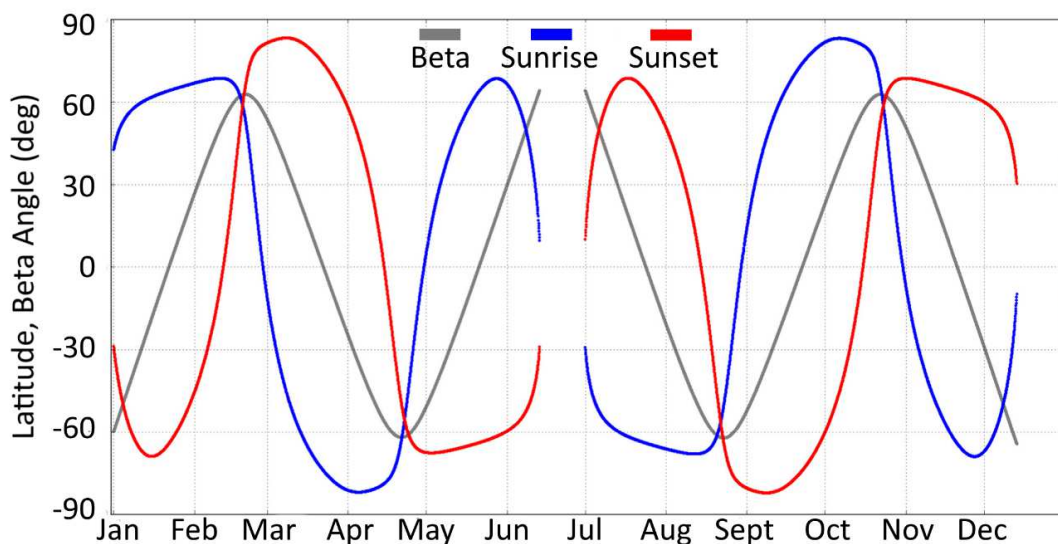


Figure 14. ACE measurement latitude for sunrise and sunset and beta angle as a function of time of year. For a brief time around each solstice ACE is unable to make measurements due to the position of its orbit. Adapted from Bernath (2017).



### 3.4 The ACE-FTS Instrument

The ACE-FTS is a Michelson interferometer custom built by ABB for the mission. The instrument has two photovoltaic detectors, indium antimonide (InSb) and mercury tellurium telluride (MCT), that provide a spectral range of 750 to 4400  $\text{cm}^{-1}$  at a resolution of 0.02  $\text{cm}^{-1}$  resolution. This resolution requires an optical path difference of 25 cm in both directions is needed. To accomplish this in a compact form factor, the instrument uses two cube-corner mirrors attached to a double pendulum (Figure 15, lower left) that pivots to change the optical path difference. Moving both arms simultaneously and double passing the light beam reduces the mechanical movement by a factor of 8, so the cube corners only need to move a distance of  $\pm 3.125$  cm. ACE-FTS has a mass of 41 kg and uses 37 W of power on average.

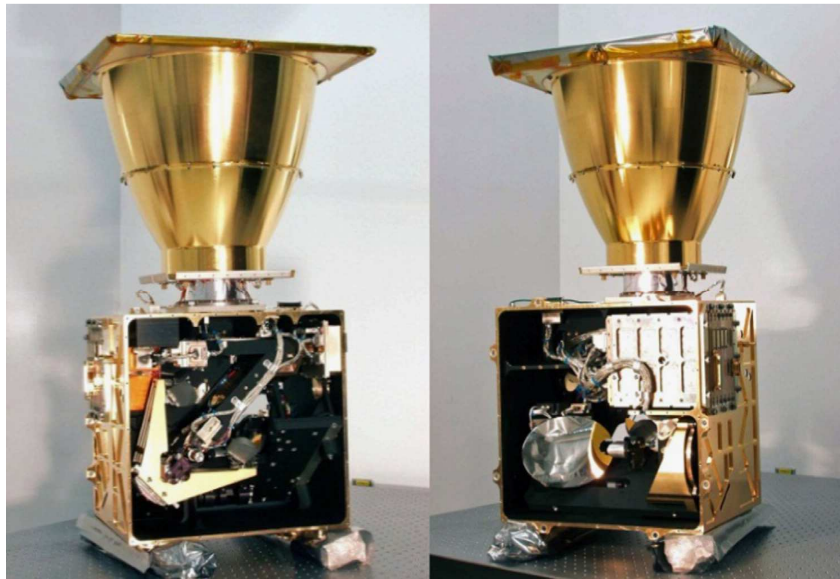


Figure 15: Internals of ACE-FTS showing the interferometer (left) and input optics (right). From Buijs et al. (2013).

A diagram of the internal optics of ACE-FTS is given in Figure 16. Collimated light enters the instrument via the servo-controlled sun tracker mirror (1) that continuously locks onto the sun. A small filter (19) in the primary mirror (3)

transmits 1.52 – 1.59  $\mu\text{m}$  light to a quad cell (21) used as the sensor to adjust the sun tracker mirror. A secondary mirror (6) collimates the light again and passes it to the ZnSe beamsplitter (9). Two corner-cube mirrors (10, 11) double passes the light back to the beamsplitter and the fixed end mirror (13). The modulated light passes through a gap in the end mirror and is passed on to the cooling subsystem and the detectors (16-18).

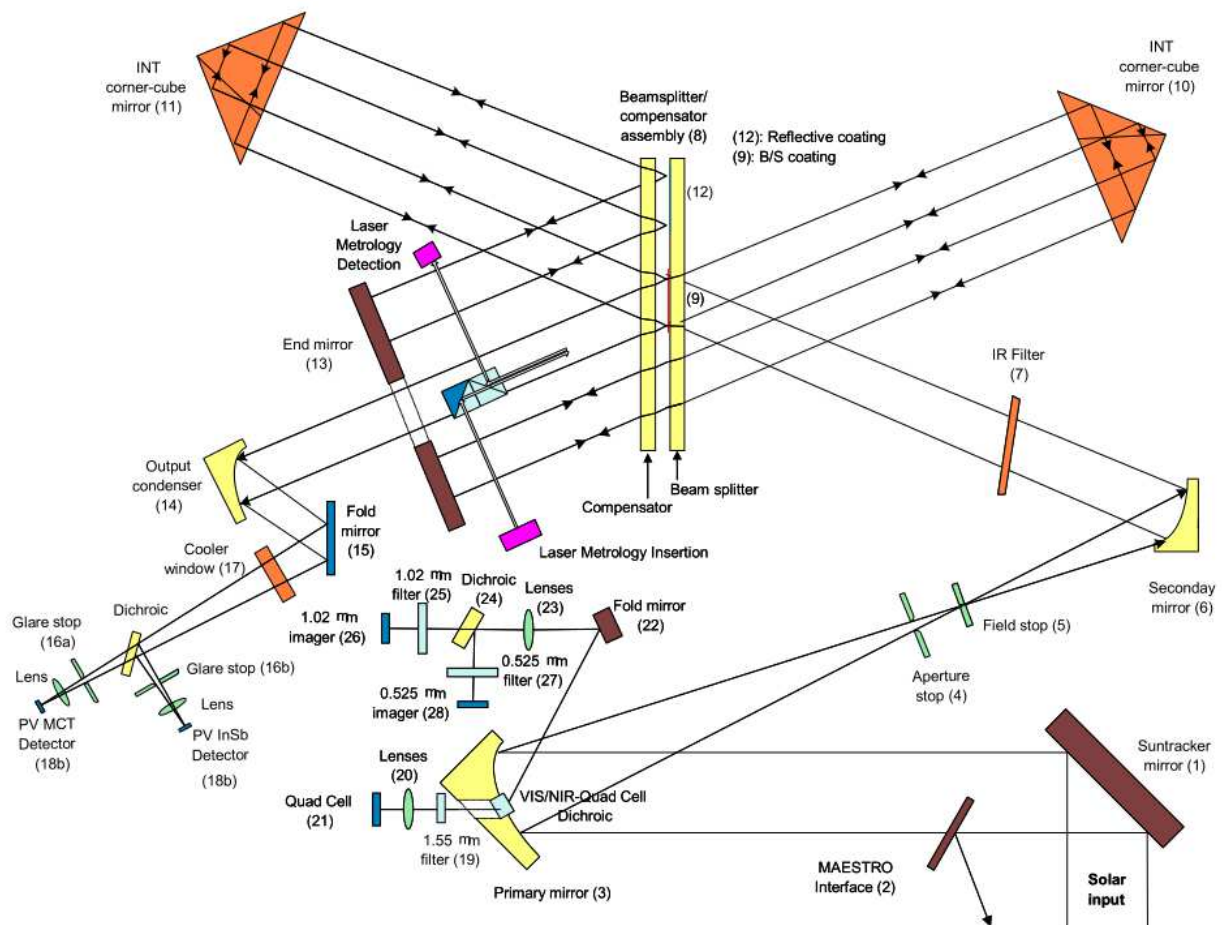


Figure 16: Schematic of ACE-FTS optics. From Buijs et al. (2013).

### 3.5 ACE-FTS data analysis

ACE transmits Level 0 data, the raw interferogram from the two instruments, to the ground. This is converted to Level 1 data, the calibrated atmospheric

transmission spectrum, using software provided by ABB that corrects for instrumental bias. Figure 17 shows a series of these spectra taken from one occultation. The Level 2 data for ACE-FTS: profiles, of temperature, pressure, and VMRs of atmospheric species, are retrieved using software produced by Boone et al. (2013). This software has gone through several versions that have added more target species, expanded the time range of occultation data used, and incorporated improvements to the retrieval. The current version is 3.5/3.6 which provides routine data products for 37 molecules and 21 of their isotopologues (Table 3) from 2004 to 2013. Research profiles for ClO, acetone, peroxyacetyl-nitrate, HFC-23, and acetonitrile are also produced.

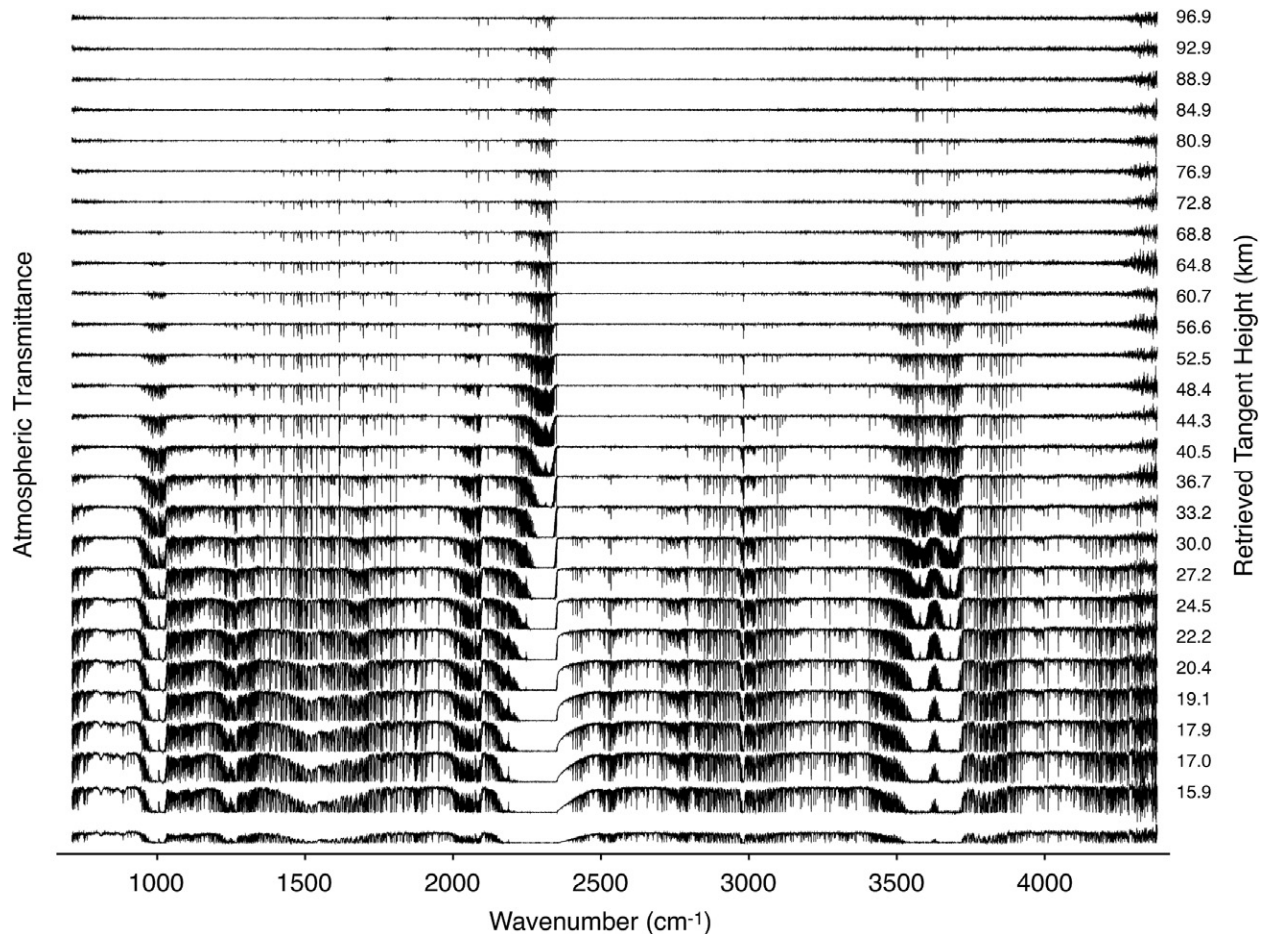


Figure 17: Series of transmission spectra measured by ACE-FTS during one occultation

Table 3: List of molecules and isotopologues routinely retrieved by ACE-FTS

H <sub>2</sub> O	O <sub>3</sub>	N <sub>2</sub>	O <sub>2</sub>	N <sub>2</sub> O	NO
NO <sub>2</sub>	HNO <sub>3</sub>	N <sub>2</sub> O <sub>5</sub>	H <sub>2</sub> O <sub>2</sub>	HO <sub>2</sub> NO <sub>2</sub>	ClONO <sub>2</sub>
CO	CO <sub>2</sub>	CH <sub>4</sub>	C <sub>2</sub> H <sub>2</sub>	C <sub>2</sub> H <sub>6</sub>	CH <sub>3</sub> OH
H <sub>2</sub> CO	HCOOH	OCS	HCN	HCl	HF
COF <sub>2</sub>	COCl <sub>2</sub>	COFCl	CF <sub>4</sub>	SF <sub>6</sub>	CH <sub>3</sub> Cl
CCl <sub>4</sub>	CFC-11	CFC-12	CFC-113	HCFC-22	HCFC-141b
HCFC-142b					
HDO	H <sub>2</sub> <sup>17</sup> O	H <sub>2</sub> <sup>18</sup> O	<sup>18</sup> OO <sub>2</sub>	O <sup>18</sup> OO	O <sup>17</sup> OO
N <sup>15</sup> NO	<sup>15</sup> NNO	N <sub>2</sub> <sup>18</sup> O	N <sub>2</sub> <sup>17</sup> O	<sup>13</sup> CO	C <sup>17</sup> O
C <sup>18</sup> O	<sup>13</sup> CO <sub>2</sub>	OC <sup>17</sup> O	OC <sup>18</sup> O	O <sup>13</sup> C <sup>18</sup> O	CH <sub>3</sub> D
<sup>13</sup> CH <sub>4</sub>	OC <sup>34</sup> S	O <sup>13</sup> CS			

The retrievals are done in two parts. First, pressure and temperature are retrieved using absorption lines of CO<sub>2</sub>. Then, these profiles are used to retrieve VMRs of the target species. Each species has a set of microwindows, small sections of the spectrum (typically 0.3-1 cm<sup>-1</sup>) that contain spectral features from the target species with minimal interference from other molecules. These microwindows are fitted to a spectrum calculated from an atmospheric model. All parameters for a given retrieval are fitted simultaneously using the Levenberg–Marquardt nonlinear least-squares method.

The model used for ACE-FTS retrievals divides the atmosphere into 150 1 km-thick layers. The calculated spectrum has a wavenumber spacing 16 times higher than the 0.02 cm<sup>-1</sup> resolution of ACE-FTS. Spectroscopic line parameters and absorption cross sections are taken from the HITRAN 2004 database (Rothman et al., 2005). Voigt lineshape functions and an empirically determined instrument lineshape are also used.

To start the pressure and temperature retrievals, a priori profiles are generated from the Global Environmental Multiscale (GEM) and NRLMSISE-00 (MISIS) models. These profiles are used as initial guesses and do not influence the final measurement. Each measurement in a profile has four variables: P, T, VMR of the target species, and the tangent height z. Two pieces of information come from the

absolute and relative intensities of the observed lines. In the middle atmosphere, from about 45 km to 65-75 km, CO<sub>2</sub> VMR is fixed, T and z are retrieved, and P is calculated using hydrostatic equilibrium:

$$\frac{dP(z)}{dz} = g(z)\rho(z) = \frac{g(z)m_a(z)P(z)}{kT(z)} \quad (10)$$

where g is acceleration due to gravity, ρ is density, m<sub>a</sub> is the average molecular mass, and k is the Boltzmann constant. Above 65-75 km, CO<sub>2</sub> begins to decrease with altitude. At this height, atmospheric refraction is negligible, so z can be calculated from geometry using accurate knowledge of the satellite's orbit and timing. CO<sub>2</sub> VMR and T are retrieved at these altitudes. Below 45 km, CO<sub>2</sub> is again fixed, P and T are retrieved, and tangent height spacing is calculated using hydrostatic equilibrium down to 15 km. GEM a priori data is used to determine the absolute tangent height. Below 15 km, lines from OC<sup>18</sup>O are used to calculate z.

Once pressure and temperature as a function of tangent height have been determined, VMRs of the target species can be retrieved. First guess profiles of VMRs are taken from the ATMOS missions; again these profiles have no effect on the final retrieval. The retrieval employs a non-linear least-squares global fitting approach, where the VMR profiles for the target species and all significant interferers (other species that appear within the microwindows) are determined simultaneously. Isotopologues of a molecular species are retrieved independently. For heavy molecules (SF<sub>6</sub>, CFCs) that have no line-by-line information in the HITRAN database, cross-sections are instead used and interpolated to the appropriate pressure and temperature. In version 3.5, altitude ranges for each species are pushed to their limits such that the signal from lines used approaches the noise level.

After the retrievals of the full set of occultations is complete, the data is analyzed to remove unphysical outliers (Sheese et al., 2015). First, profiles with known errors during data collection or processing are marked. Then, two statistical methods are used to identify extreme and moderate outliers.

Extreme outliers are marked using probability distribution functions (PDF). Data is binned by species, altitude, hemisphere, and above or below 60° latitude. For each bin, a PDF composed of three Gaussian distributions in logarithmic space is calculated. This multiplied by the number of data points in each bin to give an

expectation distribution function (EDF). The integral of the EDF over a finite range is the expected number of data points within that range. A value  $x$  where the integral  $\int_x^\infty EDF(x') dx'$  or  $\int_{-\infty}^x EDF(x') dx'$  is less than 1 is likely a statistical outlier as no data points are expected to be measured in this range. A tolerance level for this integral of 0.025 is used, corresponding to a 97.5% chance that the data point is an outlier.

Moderate outliers are marked using the mean average deviation, defined as

$$MeAD = \text{mean}_i(|x_i - \text{median}_j(x_j)|) \quad (11)$$

The bins used above are further separated into 15 day sections from which the median and MeAD are calculated. Data points that like more than 10 MeADs from the median are marked.

Profiles for a given molecule containing one or more data points tagged by the above methods are discarded as other altitude levels in that profile may be compromised. This removes between 1% and 5% of profiles from the full data set depending on the molecule analyzed.

## ATMOSPHERIC MODELING

### 4.1 Introduction

While direct measurements are very beneficial to studying the atmosphere and its constituents, they are limited in space, time, and precision. Models of the atmosphere help fill in the gaps present in observational datasets, constrain budgets of gases using atmospheric and laboratory data, and allow the effects of various perturbations in the atmosphere to be tested. The following is a brief overview of some of the concepts involved in atmospheric modeling. The final section discusses the Whole Atmospheric Community Climate Model (WACCM), an atmospheric model used in the following chapters.

### 4.2 The box model

The simplest atmospheric model is a box model which represents the atmosphere or a section of the atmosphere as a single air mass. Figure 18 shows a diagram of this type of model. The abundance of a gas  $M$  in this box is controlled by several effects: transport in ( $F_{in}$ ) and out ( $F_{out}$ ) of the box, chemical production ( $P$ ) and loss ( $L$ ), emission ( $E$ ) if the box is on the ground, and deposition ( $D$ ). The box is assumed to be well mixed, having molecular abundances that do not vary in space. The model can be at either steady state or have effects that vary with time (Jacob, 2000).

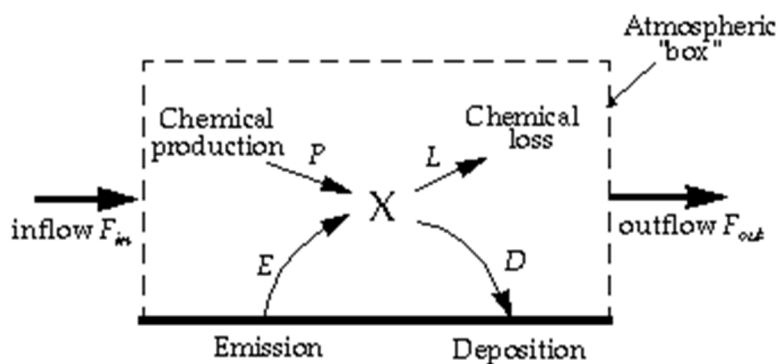


Figure 18: Diagram of a box model. From Jacob (2000).

In a box with dimensions  $l_x$ ,  $l_y$ , and  $l_z$ , the gas M has a concentration  $\rho_M$  and a mass  $m_M = \rho_M l_x l_y l_z$ . The outflow of M from the box due to wind with a speed U in the x direction is

$$F_{out} = \rho_M U_x l_y l_z \quad (12)$$

While inflow of air with a concentration of  $\rho'_m$  is

$$F_{in} = \rho'_m U_x l_y l_z \quad (13)$$

Chemical production and losses are equal to the sum of each source and sink reaction. The rates in source reactions are usually independent of the concentration of M, while sink reactions are usually first order in M:

$$L = \sum_i k_i \rho_M \quad (14)$$

The mass balance equation, representing the total change of  $m_M$  in the box, is

$$\frac{\partial m}{\partial t} = F_{in} + E + P - F_{out} - D - L \quad (15)$$

$$\frac{\partial m}{\partial t} = U_x l_y l_z (\rho'_m - \rho_M) + \sum_i k_i^P - \sum_i k_i^L \rho_M + E - D \quad (16)$$

At steady state,  $\partial M/\partial t = 0$ . If all terms in Equation (E5) are known, and all sinks are first order in M, this equation can be easily solved in terms of  $m_M$ . All sources are combined into the term S, and all sinks are combined into the term km:

$$\frac{\partial m}{\partial t} = S - km \quad (17)$$

Rearranging and integrating from 0 to t gives

$$\frac{\partial m}{S - km} = \partial t \quad (18)$$

$$\frac{-\ln(S - km)}{k} \Big|_0^t = t \Big|_0^t \quad (19)$$

$$\left(-\frac{1}{k}\right) \ln\left(\frac{S - km_t}{S - km_0}\right) = t \quad (20)$$

which rearranges to

$$m_t = m_0 e^{-kt} - \frac{S}{k} (1 - e^{-kt}) \quad (21)$$

The lifetime of M in the box is proportional to the sum of the rates of sinks:

$$\tau_M = \frac{m_M}{F_{out} + L + D} \quad (22)$$

The lifetimes of each sink can be calculated and are related to the total lifetime as

$$\frac{1}{\tau_M} = \frac{1}{\tau_{Fout}} + \frac{1}{\tau_L} + \frac{1}{\tau_D} \quad (23)$$



If the sinks are first order in  $M$ , the lifetime of  $M$  is independent of its concentration in the box (Jacob, 2000).

### 4.3 Multi-box models

A single box model is often too simple to describe real atmospheric phenomenon. The next step up is a multi-box model, where the atmosphere is simulated as a number of boxes that can exchange gases with each other. This type of model can be used to separate the layers of the atmosphere into distinct air masses, or to separate the atmosphere over urban and rural areas, or land and ocean areas.

In a simple case, two boxes are connected with each other and the outside, as show in Figure 19:

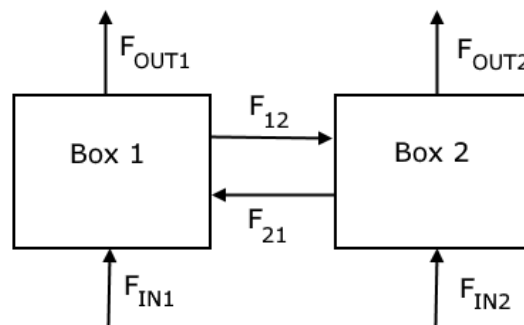


Figure 19: A two-box model.

The mass balance equation for a box in this model remains mostly the same, but the determination of  $F_{in}$  and  $F_{out}$  differ. For box 1,

$$\frac{\partial m}{\partial t} = F_{in1} + F_{21} + E + P - F_{out1} - F_{12} - D - L \quad (24)$$

If  $F_{out1}$  and  $F_{12}$  are first order in  $m_M$ , this equation can be solved analytically.

Additional boxes can be added to the model to improve its accuracy;  $F_{in}$  and  $F_{out}$  then change to account for all adjacent boxes. One-dimensional models, composed

of a vertical stack of boxes that represent thin slices of the atmosphere, are commonly used for fast calculations of vertical structure. Vertical resolution is typically on the order of 1 km when considering the whole atmosphere (Jacob, 2000).

#### 4.4 Multi-dimensional models

When information on horizontal structure is desired, two-dimensional and three-dimensional grids of boxes can be used. The horizontal scale of global 2-D and 3-D models is typically between 1 and 10 degrees. Due to the number of “boxes” at this point, solving the model equations analytically becomes difficult, so they are instead advanced through a series of time steps  $\Delta t$  and solved numerically.

Models that used a fixed grid in space and determine the abundance of gas inside each grid element are known as Eulerian models. In contrast, Lagrangian models do not use a grid track the motion and composition of individual air masses; these models are typically regional in scale. Almost all global Eulerian models use a longitude-latitude horizontal grid and a vertical grid based on pressure levels. Alternative grids such as a cubed sphere or various geodesic polyhedrons eliminate the “singularity” present at the poles on a latitude-longitude grid (Washington et al., 2009).

As with 1D models, the continuity equation has terms for both transport and chemical processes. Since transport only depends only on coupling between adjacent boxes in the grid and chemistry depends only on the species within the same box, the two sets of terms can be separated:

$$\frac{\partial n}{\partial t} = \left[ \frac{\partial n}{\partial t} \right]_{trans} + \left[ \frac{\partial n}{\partial t} \right]_{chem} \quad (25)$$

Transport can further be separated into the three orthogonal directions which are calculated in parallel. This separation is known as operator splitting and allows full set of equations used by the model to be broken down into smaller groups that are faster to solve. This technique depends on the assumption that the coupling between transport and chemistry is negligible during over the time step, typically between 15 and 60 minutes for global models. One way to confirm this assumption

is to solve the terms in one order, then solve in the reverse order, and check if the output is acceptably close (Jacob, 2007).

In 3D models, transport can be considered in a more realistic fashion rather than being parametrized. The overall transport term in three dimensions is

$$\left[\frac{\partial n}{\partial t}\right]_{trans} = -\frac{\partial F_x}{\partial x} - \frac{\partial F_y}{\partial y} - \frac{\partial F_z}{\partial z} = -\nabla \cdot \vec{F} \quad (26)$$

The flux  $\vec{F}$  can be broken down into molecular diffusion,  $\vec{F}_{diff}$ , and advection due to winds,  $\vec{F}_{adv}$ . Flux from diffusion is given by Fick's first law:

$$\vec{F}_{adv} = -D \left( \frac{\partial n}{\partial x} + \frac{\partial n}{\partial y} + \frac{\partial n}{\partial z} \right) = -D \nabla n \quad (27)$$

where  $D$  is the molecular diffusion coefficient with units  $\text{cm}^2 \text{s}^{-1}$ . The advective flux is equal to  $n\vec{U}$ , where  $\vec{U}$  is the local velocity of wind. Inserting these two terms into Equation 15 gives

$$\left[\frac{\partial n}{\partial t}\right]_{trans} = -\nabla \cdot (n\vec{U}) + D \nabla^2 n \quad (28)$$

In the lower atmosphere, diffusion is slow compared to wind and can be neglected. However, it becomes important in the thermosphere (Jacob, 2007).

Winds in the atmosphere are due to pressure and thermal gradients and are complicated to model. To simplify for atmospheric models, overall wind can be broken down into two terms: the mean wind velocity and turbulence. On the spatial scale of an atmospheric model, turbulent mixing can be approximated as a process similar to diffusion. This approximation is known as eddy diffusion. Neglecting molecular diffusion, the equation for transport then becomes

$$\frac{\partial n}{\partial t}_{trans} = -\nabla \cdot n \langle \vec{U} \rangle - \nabla \cdot \vec{F} \quad (29)$$

where  $\langle \vec{U} \rangle$  is the average wind speed over the time step. Several techniques available to numerically solve for the above equation (Jacob, 2007).

Solving for the chemistry of the model involves a system of differential equations of the form

$$\frac{\partial \vec{n}}{\partial t}_{chem} = P(\vec{n}) - L(\vec{n}) \quad (30)$$

where  $\vec{n}$  is a vector containing the number densities of all relevant species. These species can have lifetimes that vary from seconds to years. Several methods can be used to solve for a certain species based on its lifetime.

The simplest and fastest methods are explicit solvers which calculate concentrations solely from the concentrations from the previous time step. Consider the reactions  $Y \rightarrow X$  (source of X) and  $X \rightarrow \text{products}$  (sink of X). The concentration of X at each time step using the forward Euler method is calculated as

$$n_X(t + \Delta t) = n_X(t) + k_1 n_Y \Delta t - k_2 n_X \Delta t \quad (31)$$

However, if the time step is longer than the lifetime of X, this method will give unrealistic results (Jacob, 2007).

Implicit solvers predict the concentration at  $t + \Delta t$  by converging to a numerical solution rather than calculating it explicitly. Although these methods are slower than using an explicit solver, they work on any species regardless of its lifetime. The following example uses the backward Euler method. Equation 19 is expressed using a time step  $\Delta t$  and all terms are moved to one side:

$$\frac{n_i(t + \Delta t) - n_i(t)}{\Delta t} = P(\vec{n}(t + \Delta t)) - L(\vec{n}(t + \Delta t)) \quad (32)$$

$$f_i(\vec{n}) = n_i(t + \Delta t) - n_i(t) - P(\vec{n}(t + \Delta t))\Delta t + L(\vec{n}(t + \Delta t))\Delta t = 0 \quad (33)$$

A first guess for  $\vec{n}(t + \Delta t)$  is made, and closer estimates are made using Newton's method until the values converge to within an acceptable error.

#### 4.5 The Whole Atmosphere Community Climate Model

The Whole Atmosphere Community Climate Model (WACCM) is a comprehensive atmospheric model and part of the Community Earth System Model (CESM). The current version 4 of WACCM is built upon the Community Atmospheric Model version 4 while extending the maximum height of the model to the lower thermosphere.

CESM contains additional models for land, ocean, sea ice, and land ice that interact with WACCM. Each of these components runs forward in time, then exchanges data after each time step. In the model runs performed in the following chapters, the land and sea ice modules are active and provide information such as albedo and fluxes for emissions and deposition. The ocean module is run as a pure data model that reads in and shares sea surface temperatures. The land ice module is inactive.

The physical aspects of the atmosphere that WACCM models are divided into two groups, the dynamic core and physics parametrizations. The dynamic core solves for large scale motion within the atmosphere driven by pressure and temperature. The parameterization package includes several processes that occur on a scale smaller than the model grid: precipitation, radiative transfer, surface exchange of heat and moisture, and turbulent mixing (Neale et al., 2012). WACCM uses a grid that contains 66 vertical levels from the surface to  $5.1 \times 10^{-6}$  hPa, or about 140 km; vertical resolution ranges from 1 km in the troposphere to 3.5 km in the mesosphere. The horizontal grid is adjustable.

The chemistry component of WACCM is based on MOZART, a model of tropospheric chemistry (Emmons et al., 2010). A total of 52 species are modeled including members of the  $O_x$ ,  $NO_x$ ,  $HO_x$ ,  $ClO_x$ ,  $BrO_x$  families plus  $CH_4$  and its oxidation products. The mechanism set contains over 200 reactions that cover neutral gas-phase reactions, photolysis, heterogeneous reactions on the surface of aerosols, and ionic reactions. Some species have additional sources and sinks that are modeled such as surface emissions represented by boundary conditions, wet and dry deposition, and in-situ flux from lightning or aircraft. Both explicit and implicit solvers are available and can be set on a per-molecule basis. WACCM does not natively support molecular isotopologues, but they can be treated as separate species and duplicating the chemistry and other processes these species are involved in. The specific changes made for each isotopologue studied are given in the following chapters.

## METHANE ISOTOPOLOGUES IN THE STRATOSPHERE

### 5.1 Introduction

Methane is the second most important greenhouse gas behind CO<sub>2</sub> with a 20-year global-warming potential (GWP) of 72 (Ciais et al., 2013). In the troposphere, concentrations of methane have increased since the Industrial Revolution, from mixing ratios of about 700 ppb in the 1800s to over 1700 ppb by the 1990s (Etheridge et al., 1998). From 1999 to 2006, methane levels remained stable, but have begun to increase again since 2007 (Terao et al., 2011). The reason for this leveling off in the 2000s is highly debated. Possible causes include the stability or reduction in anthropogenic activities that emit methane, decreasing wetland emissions, and changes in atmospheric OH concentrations (Ciais et al., 2013).

All methane that enters the atmosphere comes from surface sources and can be divided into three groups, whether natural or anthropogenic. Biogenic sources produce methane from the anaerobic decomposition of organic matter and occurs in wetlands, livestock farms, rice paddies, and landfills. Thermogenic sources come from the geologic formation of fossil fuels in the Earth's crust which are released from tectonic or human activity. Pyrogenic sources involve the incomplete combustion of organic matter or fossil fuels. Each source of methane has a distinct isotopic signature as shown in Figure 20 (Rigby et al., 2012). Since methane has a lifetime of about 9 years (Ciais et al., 2013), it is well mixed in the troposphere and has a uniform isotopic composition above the surface. Concentrations are slightly higher in the Northern Hemisphere due to the increased emissions there.

The primary sink of methane is the reaction with OH which occurs in both the troposphere and stratosphere. About 95% of atmospheric methane is consumed in this manner. Additional minor reactions can occur in the stratosphere with Cl and O(<sup>1</sup>D). CH<sub>4</sub> + Cl is particularly important near the poles as Cl concentrations are high following the breakdown of the polar vortex. Each of these three reactions has its own KIE listed in Table 4. In the upper stratosphere, methane can also photolyze, though little methane reaches these altitudes. Near the surface, uptake by methanotropic bacteria is another minor sink (Ciais et al., 2013).

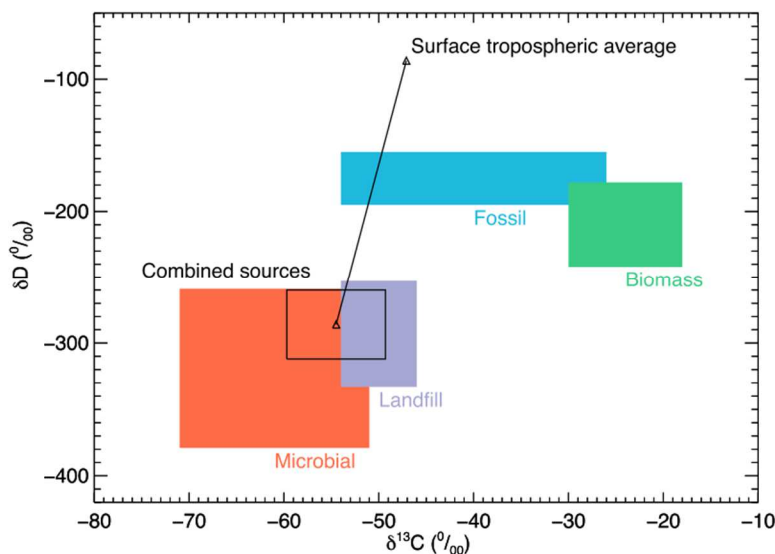


Figure 20: Isotopic composition of surface methane sources. From Rigby et al. (2012)

While methane is nearly constant throughout the troposphere, the stratospheric distribution of methane roughly follows the pattern of Brewer-Dobson circulation. Air entering through the tropical tropopause is rich in methane. Concentrations decrease with altitude and are the lower over the poles from the downwelling of methane-depleted air (Remsberg, 2015).

Table 4: Kinetic isotope effect ratios of methane with OH, O<sup>1</sup>D, and Cl

Reactant	$k_H/k_D$	$k_{12}/k_{13}$	Temperature	Ref.
OH	$1.294 \pm 0.018$	$1.0039 \pm 0.0004$	296 K	(Saueressig et al., 2001)
O <sup>1</sup> D	1.06	1.013	296 K	(Saueressig et al., 2001)
Cl	$1.47 \pm 0.03$	$1.06 \pm 0.01$	298 K	(Feilberg et al., 2005b)

The majority of measurements of methane and its isotopologues have been done in the troposphere. One large ground-based sampling program is the Global

Greenhouse Gas Reference Network, overseen by NOAA's Earth System Research Laboratory (Andrews et al., 2014). Sampling higher in the troposphere is frequently done by aircraft such as the CARIBIC program (Brenninkmeijer et al., 2007) or by balloon flights. In the upper stratosphere, measurements are far less common as only balloons can reach this height for sampling (Röckmann et al., 2011). An alternative to direct sampling at this altitude is satellite-based remote sensing. Some satellite instruments point toward nadir including GOSAT (Yokota et al., 2009), TES onboard the Aura satellite (Wecht et al., 2012) and IASI on MetOp (Xiong et al., 2013). Others observe the limb of the atmosphere including MIPAS (Payan et al., 2009) and HALOE (Park, 2004a). A few, such as SCIAMACHY on ENVISAT (Schneising et al., 2009) and TES can look in either direction. However, these satellite measurements do not include the heavy isotopes of methane, and many of them have limited vertical sampling or only measure the total column density.

This chapter presents data on methane and its two heavy isotopologues from ACE-FTS. Additionally, a model run is performed with WACCM for comparison to the data from ACE. The following is adapted from a paper published in Atmospheric Measurement Techniques (Buzan et al., 2016) and uses contributing work from C. Boone (ACE-FTS retrievals) and P. Bernath (supervisor). Text from other authors has not been used here.

## 5.2 Methods

Microwindows corresponding to the  $\nu_4$ ,  $2\nu_4$ , and  $\nu_3$  vibrational bands of  $\text{CH}_4$  were used for retrievals from ACE spectra (Boone et al., 2013). The fundamental  $\nu_4$  and  $\nu_3$  bands are used at higher altitudes while the  $2\nu_4$  overtone band is used at lower altitudes where the fundamentals are saturated. A summary of the microwindows used in the current study is given in Table 5 while the full microwindow list is given in Tables 13-15 in the Appendix.

The microwindow set used here for the main isotopologues differs from the normal version 3.5 microwindow set. Initial results of  $\delta\text{D}$  and  $\delta^{13}\text{C}$  showed latitude-dependent bands of heavy isotopic enrichment that were attributed to systematic



errors in the main isotopologue. To correct this, additional microwindows beyond the v3.5 set are used between 40 and 50 km and below 25 km. These corrections and their effects are discussed further in Section 5.4.1.

Table 5: Summary of microwindows used by ACE for retrieval of CH<sub>4</sub>

Isotopologue	Number of microwindows	Altitude Range (km)	Wavenumber Ranges (cm <sup>-1</sup> )
CH <sub>4</sub>	74	5-75	1139,1219-1374, 1672, 1876, 1950, 2610-3086
CH <sub>3</sub> D	45	5-35	923-1480, 2623-3096
<sup>13</sup> CH <sub>4</sub>	36	5-50	1202-1339, 1950, 2566-2839

For the main isotopologue of methane, random errors from the least-squares fitting process are in the range of 2% to 6% over the range of altitudes employed in this study. For <sup>13</sup>CH<sub>4</sub>, fitting errors range from 2% to 6% below 30 km, and the errors increase for altitudes above 30 km, reaching 10% near the upper altitude limit of the retrieval. For CH<sub>3</sub>D, fitting errors range from 4% to 12% below 15 km and increase for higher altitudes, approaching 30% near the upper altitude limit of the retrieval.

Spacing of retrieval altitudes for VMR profiles of the isotopologues of methane varies from ~2 km (low altitudes) to 6 km (high altitudes) and averages around 4 km. The profiles were interpolated onto a 1 km grid using a piecewise quadratic interpolation. Then, the profiles were placed into seasonal bins and 10 degree latitude bins. Figure 21 shows the spatial distribution of the profiles by season. Most of the profiles are at higher latitudes, but there are at least 40 profiles in each equatorial bin every season. The binning process averages the results from many occultations in order to reduce the impact of the random error on the results (the random error decreases according to the square root of the number of elements included in the average).

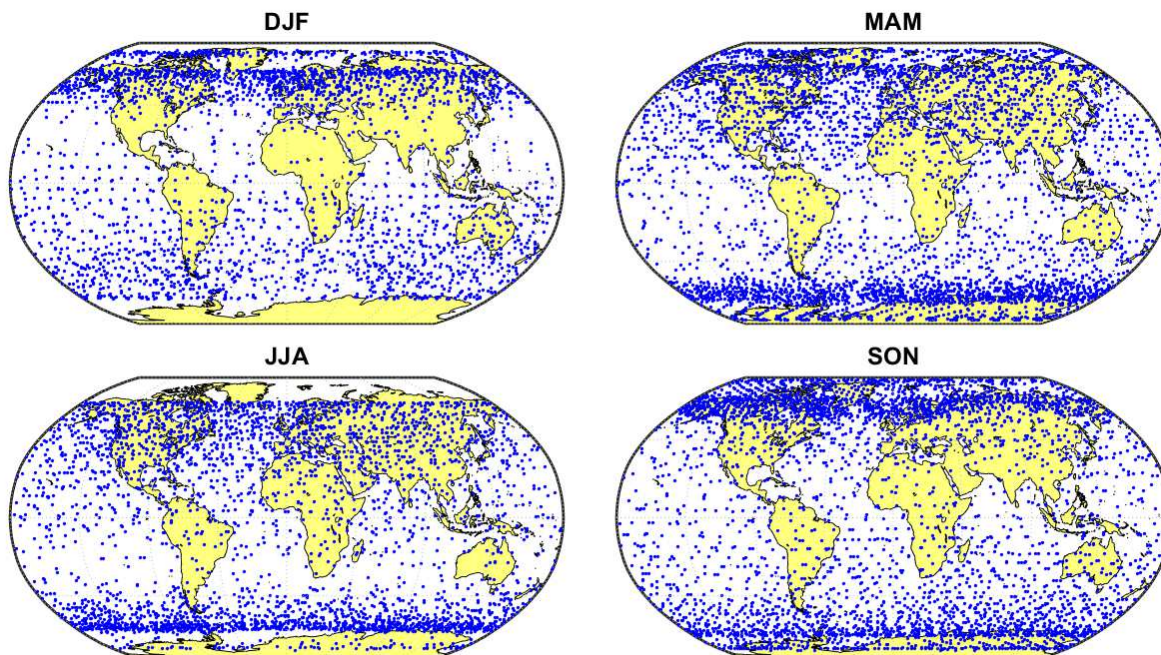


Figure 21. Location of all ACE CH<sub>4</sub> measurements by season.

The following modifications were made to WACCM to support CH<sub>3</sub>D and <sup>13</sup>CH<sub>4</sub>. First, the reactions of the first step of methane oxidation are duplicated and their rate constants adjusted by the kinetic isotope effects  $k_D/k_H$  and  $k_{12}/k_{13}$ . The KIE of methane with each oxidant is given in Table 4 and the full set of modified reactions is listed in Table 6. No further reactions or molecules are modified as only the isotopic composition of methane is studied here. Next, new photolytic cross sections were added for all three isotopologues (Lee et al., 2001; Nair et al., 2005). The blue shifts of the cross sections are approximately 1 nm for CH<sub>3</sub>D and 0.04 nm for <sup>13</sup>CH<sub>4</sub>. Finally, boundary conditions representing surface emissions were calculated for the two heavy isotopologues. Keeling plots presented by Röckmann et al. (2011) were used to derive relations between [CH<sub>4</sub>] versus  $\delta D$  and  $\delta^{13}C$ :

$$\delta D = \frac{1.50 \times 10^4}{[CH_4]/(ppm)} - 55.6\text{‰} \quad (34)$$

$$\delta^{13}C = \frac{1.29 \times 10^4}{[CH_4]/(ppm)} - 151.4\text{‰} \quad (35)$$

These relations were applied to the existing CH<sub>4</sub> boundary conditions used by WACCM (Lamarque et al., 2010) to derive boundary conditions for CH<sub>3</sub>D and <sup>13</sup>CH<sub>4</sub>.

Table 6: Reactions and kinetic constants of reactions for the CH<sub>4</sub> WACCM run.

Temperature-independent reactions use a single rate constant A in units of cm<sup>3</sup> molecule<sup>-1</sup> s<sup>-1</sup>. Temperature-dependent reactions have a rate constant given by the equation  $k(T) = A \times \exp(-E/RT)$ . The factor E/R has units of K<sup>-1</sup>.

Reaction	A	E/R	Ref.
CH <sub>4</sub> + OH → CH <sub>3</sub> + H <sub>2</sub> O	2.45×10 <sup>-12</sup>	1775	(Sander et al., 2006)
<sup>13</sup> CH <sub>4</sub> + OH → CH <sub>3</sub> + H <sub>2</sub> O	2.44×10 <sup>-12</sup>	1775	(Sander et al., 2006)
CH <sub>3</sub> D + OH → CH <sub>3</sub> + H <sub>2</sub> O	3.50×10 <sup>-12</sup>	1950	(Sander et al., 2006)
CH <sub>4</sub> + Cl → CH <sub>3</sub> + HCl	7.30×10 <sup>-12</sup>	1280	(Sander et al., 2006)
<sup>13</sup> CH <sub>4</sub> + Cl → CH <sub>3</sub> + HCl	6.89×10 <sup>-12</sup>	1280	(Sander et al., 2006)
CH <sub>3</sub> D + Cl → CH <sub>3</sub> + HCl	7.00×10 <sup>-12</sup>	1380	(Feilberg et al., 2005b)
CH <sub>4</sub> + O( <sup>1</sup> D) → CH <sub>3</sub> + OH	1.31×10 <sup>-10</sup>		(Sander et al., 2006)
CH <sub>4</sub> + O( <sup>1</sup> D) → CH <sub>2</sub> O + H + HO <sub>2</sub>	3.00×10 <sup>-11</sup>		(Sander et al., 2006)
CH <sub>4</sub> + O( <sup>1</sup> D) → CH <sub>2</sub> O + H <sub>2</sub>	7.50×10 <sup>-12</sup>		(Sander et al., 2006)
<sup>13</sup> CH <sub>4</sub> + O( <sup>1</sup> D) → CH <sub>3</sub> + OH	1.11×10 <sup>-10</sup>		(Saueressig et al., 2001)
<sup>13</sup> CH <sub>4</sub> + O( <sup>1</sup> D) → CH <sub>2</sub> O + H + HO <sub>2</sub>	2.96×10 <sup>-11</sup>		(Saueressig et al., 2001)
<sup>13</sup> CH <sub>4</sub> + O( <sup>1</sup> D) → CH <sub>2</sub> O + H <sub>2</sub>	7.40×10 <sup>-12</sup>		(Saueressig et al., 2001)
CH <sub>3</sub> D + O( <sup>1</sup> D) → CH <sub>3</sub> + OH	1.06×10 <sup>-10</sup>		(Saueressig et al., 2001)
CH <sub>3</sub> D + O( <sup>1</sup> D) → CH <sub>2</sub> O + H + HO <sub>2</sub>	2.83×10 <sup>-11</sup>		(Saueressig et al., 2001)
CH <sub>3</sub> D + O( <sup>1</sup> D) → CH <sub>2</sub> O + H <sub>2</sub>	7.08×10 <sup>-12</sup>		(Saueressig et al., 2001)
CH <sub>4</sub> + hν → products			(Lee et al., 2001)
<sup>13</sup> CH <sub>4</sub> + hν → products			(Lee et al., 2001)
CH <sub>3</sub> D + hν → products			(Nair et al., 2005)

WACCM was run as a standalone model with a resolution of 4x5 degrees (latitude/longitude) and 66 vertical levels. The model was run as a perpetual year 2000 for a total of 20 years: 17 years of spin-up time followed by 3 years that were analyzed. Data from WACCM was analyzed in two ways. First, to observe general trends, the entire data set from the final 3 years was averaged monthly and placed into 10 degree latitude bins. Second, to remove sampling bias from ACE when comparing to WACCM, a smaller data set was constructed by measuring "profiles" from the whole WACCM data set at the same times and locations as each ACE

profile. This data set was averaged seasonally and placed into 10 degree latitude bins to match the analysis of ACE data.

### 5.3 Results

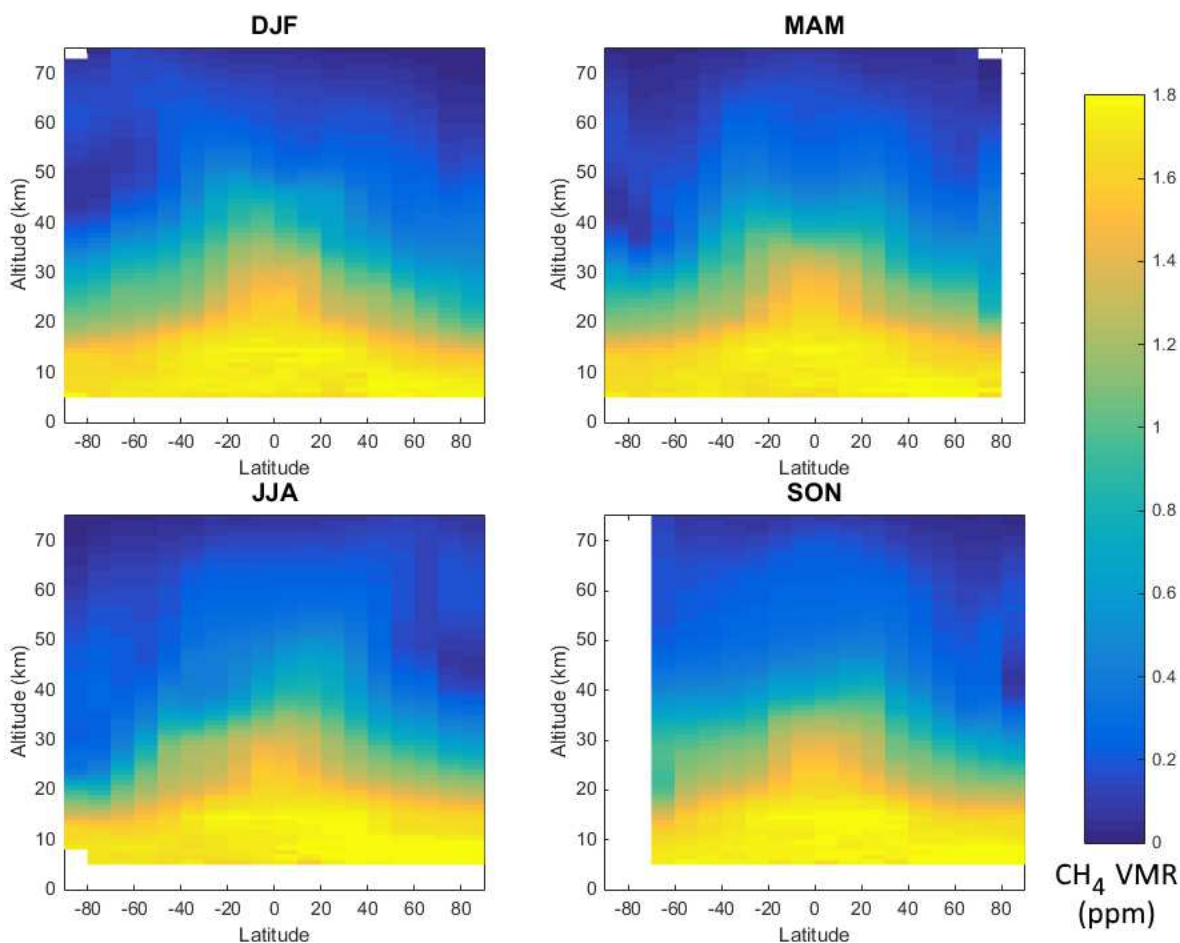


Figure 22. ACE total CH<sub>4</sub> VMR by season.

Figure 22 shows the total VMR of methane as a function of latitude and altitude as measured by ACE. In the well-mixed troposphere, the VMR of methane is nearly constant at around 1750 ppb. Above the tropopause methane VMRs decrease steadily at higher altitudes to about 300 ppb at 20-25 km above the tropopause. Methane near the Equator extends higher into the atmosphere primarily due to the

higher tropopause, as well as the transport of air containing elevated levels of methane from the troposphere to the lower stratosphere in the tropics (as part of the Brewer-Dobson circulation). Some seasonal variation is visible: pockets of methane-depleted air are present over the poles especially during the summer and fall months: December to May over the South Pole and June to November over the North Pole.

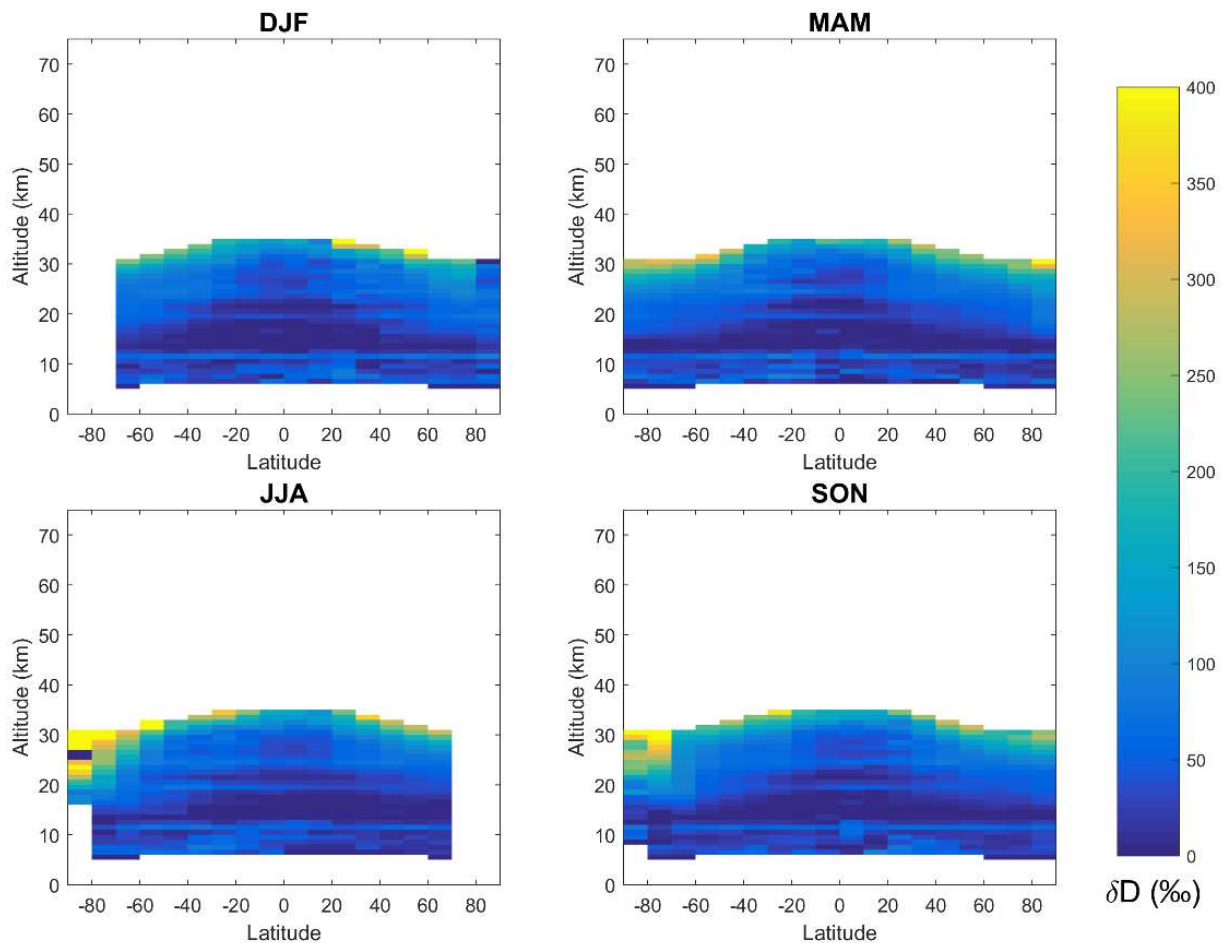


Figure 23. ACE  $\delta D$  by season.

ACE data for  $\delta D$  as a function of latitude and altitude are plotted in Figure 23.  $\text{CH}_3\text{D}$  data is available from 5 km to 30-35 km, depending on latitude. Above 12 km, values of  $\delta D$  steadily increase with altitude from tropospheric values around

0‰, then sharply increase at the highest few kilometers of the available data to between +250‰ and +400‰. This sharp increase occurs at the same altitudes where the fitting errors during retrieval are the highest. In addition, high levels of CH<sub>3</sub>D are noticeably present over the South Pole from June to November. Below 12 km, a “step function” occurs in the δD data and it becomes much noisier, averaging around +35‰. An additional horizontal line of high enrichment is present around 20 km. These are due to the previously mentioned systematic error in the main CH<sub>4</sub> isotope. Finally, there is another artifact present below 80°S in June-August: a single altitude with a very low δD. This is due to the low number and quality of measurements taken over the poles caused by the satellite’s non-polar orbit.

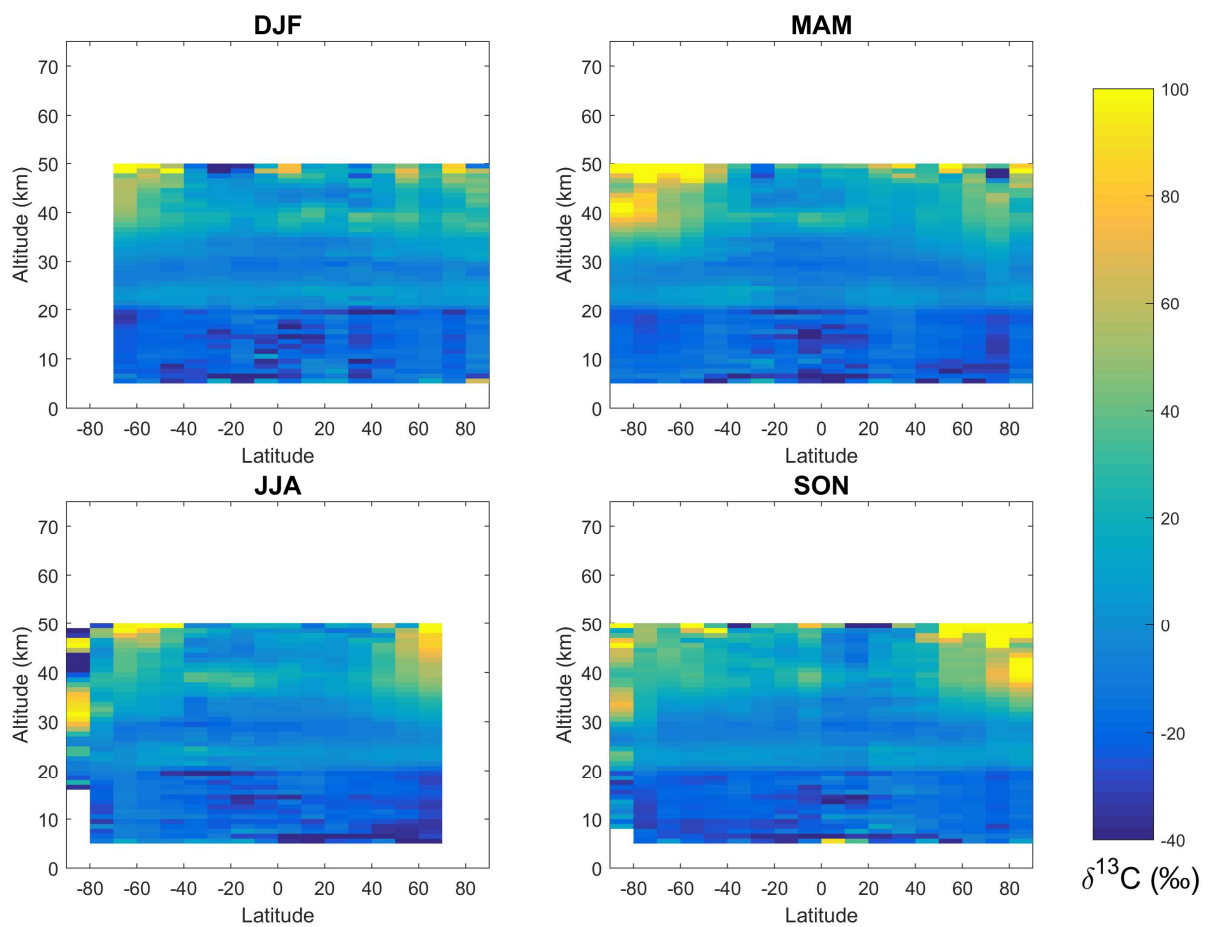


Figure 24. ACE δ<sup>13</sup>C by season.

ACE data for  $\delta^{13}\text{C}$  are plotted in Figure 24. These data are available from 6 km to 50 km except over the poles during some seasons. Overall the data are noisier than for  $\delta\text{D}$ , but values of  $\delta^{13}\text{C}$  still increase with altitude. Tropospheric values average near  $-20\text{‰}$ , while lower stratospheric values average near  $0\text{‰}$ . Seasonal changes are also more apparent than in  $\delta\text{D}$ . Enrichment of  $^{13}\text{C}$  is strongest during the summer and fall months. Values of  $\delta^{13}\text{C}$  as high as  $+100\text{‰}$  are present over both poles between 35 and 50 km. Higher  $\delta^{13}\text{C}$  values are present in two bands at 22 km and 40 km, additional artifacts from the main isotopologues.

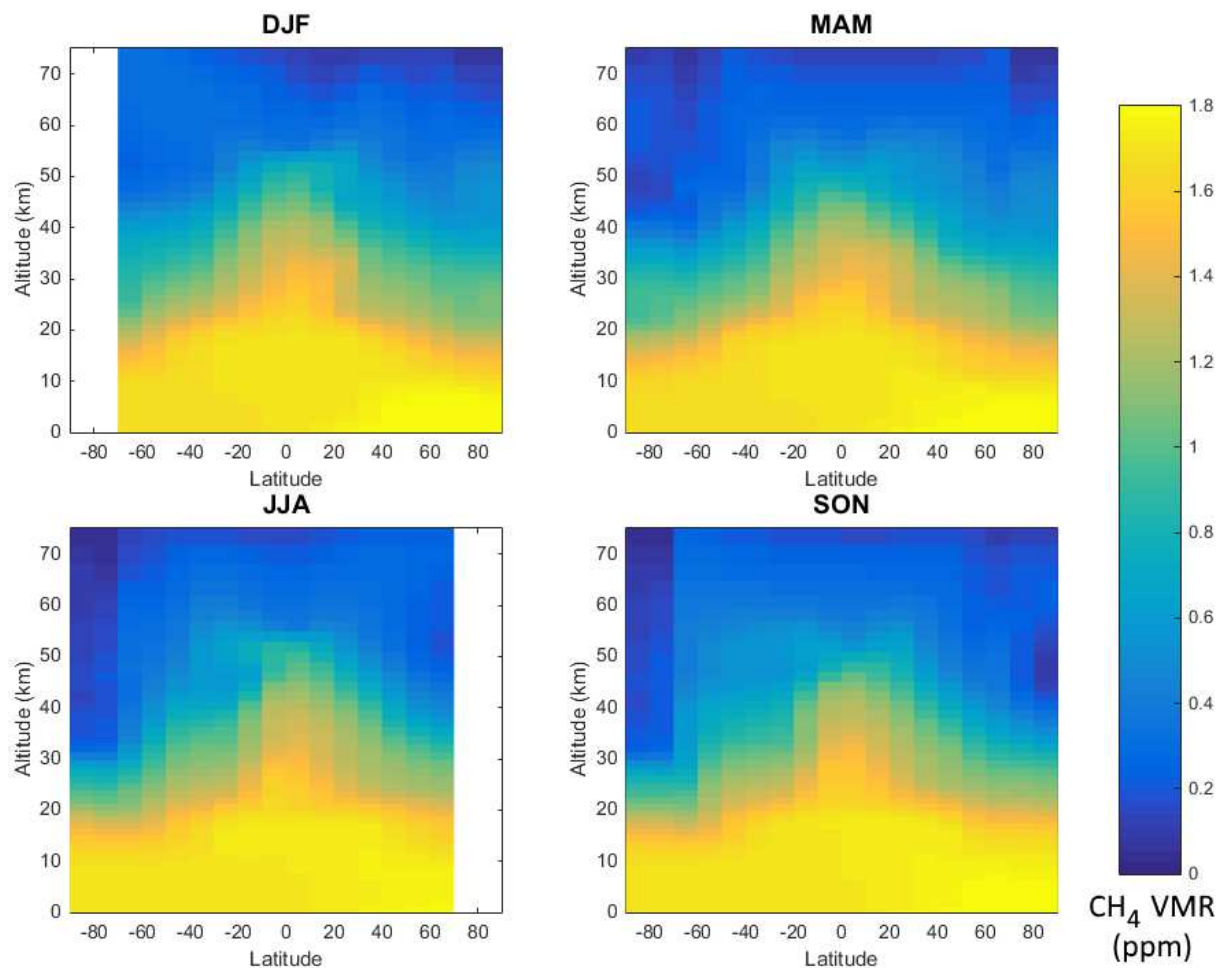


Figure 25. Total VMR by season from the ACE-sampled WACCM data set.

The ACE-sampled WACCM data set is presented in Figure 25 (total CH<sub>4</sub> VMR), Figure 26 ( $\delta D$ ), and Figure 27 ( $\delta^{13}C$ ). The model output of total methane agrees well with ACE's observations. Tropospheric methane fluctuates slightly by season but is steady around 1700 ppb. The plume of methane-rich air over the Equator in the stratosphere is also present, and mixing ratios of methane decrease with higher altitudes in the stratosphere and mesosphere. Seasonal variation is noticeable here; air masses low in methane form over each pole around 50 km during the summer, then sink and become further depleted during the fall.

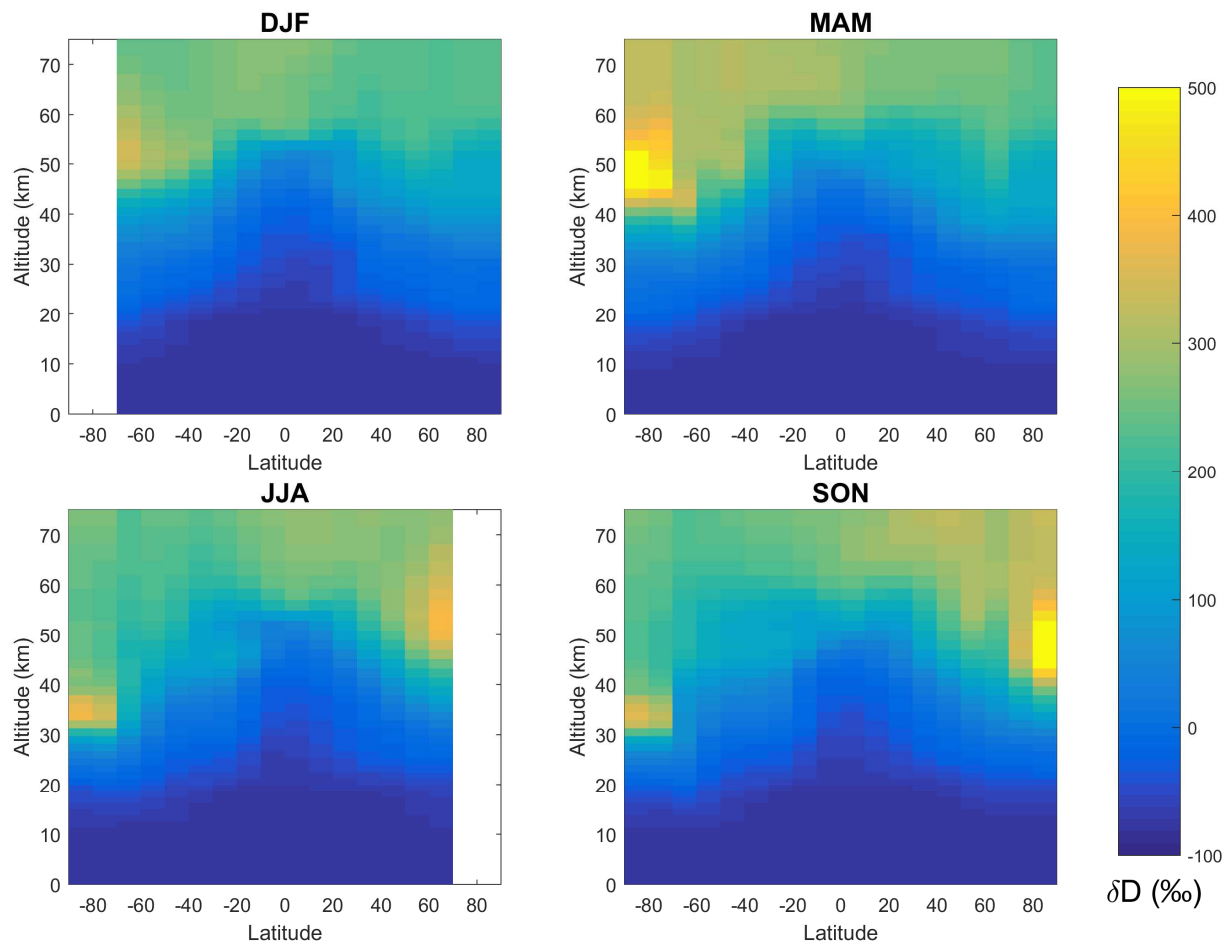


Figure 26.  $\delta D$  by season from the ACE-sampled WACCM data set.



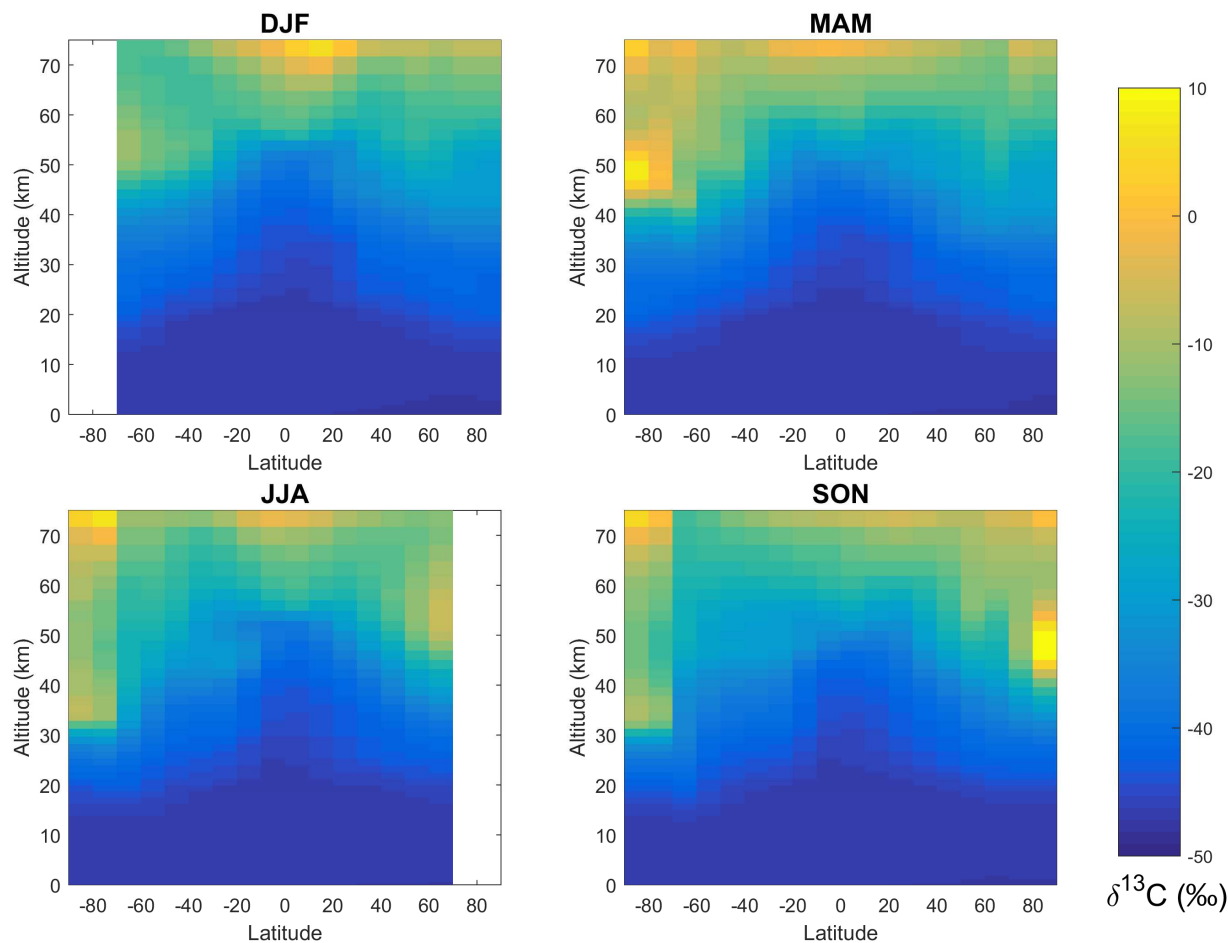


Figure 27.  $\delta^{13}\text{C}$  by season from the ACE-sampled WACCM data set.

These seasonal trends are especially visible in  $\delta\text{D}$  and  $\delta^{13}\text{C}$ . The polar air masses of depleted  $\text{CH}_4$  are enriched in both  $\text{CH}_3\text{D}$  and  $^{13}\text{CH}_4$  and become further enriched as they sink. Enrichment in the southern air mass reaches a lower altitude and lingers for a longer period, February to June, than the northern air mass which is enriched only from July to October. This difference in altitude is also shown in ACE; enrichment in the southern hemisphere reaches low enough to be detected by ACE, while enrichment in the northern hemisphere remains too high to be measurable by ACE.

## 5.4 Discussion

### 5.4.1 Corrections to ACE retrievals of $^{12}\text{CH}_4$ .

Several latitude-independent lines of heavy enrichment are present in the data for both heavy isotopologues: at 20 km and 12 km for  $\delta\text{D}$  and at 40 km and 20 km for  $\delta^{13}\text{C}$ . They were believed to be unphysical due to lack of seasonal variation and constant latitude across the Earth's surface and attributed to errors in the retrieval of  $^{12}\text{CH}_4$  due to their presence at 20 km in both isotopologues. Poor consistency between lines at different altitudes in  $^{12}\text{CH}_4$  are the cause of the bands. To correct for these artifacts, additional microwindows were added to the v3.5 set for  $^{12}\text{CH}_4$  between 40 and 50 km and below 25 km. In addition, spectroscopic parameters (positions, line widths, pressure shifts, and intensities) for  $\text{CH}_4$  lines in the  $2\nu_4$  band were adjusted to improve fitting residuals and to improve consistency between lines within this band and with lines in the  $\nu_4$  and  $\nu_3$  bands. This reduced the magnitude of the sharp increase in the band but did not remove them. At 20 km, the retrieval process transitions from the  $2\nu_4$  band below to the  $\nu_4$  band above used for the  $^{12}\text{CH}_4$  retrieval, suggesting a problem in spectroscopic compatibility between these two vibrational bands.

### 5.4.2 Keeling plots of ACE data

As with several gases in the atmosphere, there is a strong inverse correlation between the total mixing ratio of methane and  $\delta\text{D}$  and  $\delta^{13}\text{C}$ . This relation was first noted by Keeling (1958) in samples of  $\text{CO}_2$ , so a plot of  $[\text{CH}_4]$  or  $[\text{CH}_4]^{-1}$  versus  $\delta$  is often called a "Keeling plot". This phenomenon has more recently been demonstrated by e.g. Röckmann et al. (2011) for methane. Plotting  $[\text{CH}_4]^{-1}$  versus  $\delta$  of a time series of measurements results in an ellipse rather than a straight line due to seasonal variation in the sources and sinks of methane (Allan et al., 2001; Lassey et al., 2011).

Keeling plots for both isotopologues are given in Figure 28 by plotting the reciprocal of the methane mixing ratio against  $\delta\text{D}$  and  $\delta^{13}\text{C}$  for each altitude in

every ACE profile. In these figures, the expected relationship should appear as a sloped line. Such a slope is visible for  $\delta D$  at stratospheric altitudes. However, there is still a significant range of  $\delta D$  values for a given mixing ratio of methane, especially in the troposphere where methane has little spatial variability due to being well-mixed. For  $^{13}CH_4$ , a relationship between total methane and  $\delta^{13}C$  is much more difficult to distinguish. This is not surprising considering that the  $\delta^{13}C$  data have a larger range of values than the  $\delta D$  data. Several streaks are also visible in the  $\delta^{13}C$  data but are considered artifacts; since molecular concentrations from ACE are reported to three significant figures, a sharp change in precision occurs at multiples of ten, causing the data points to clump together into lines at just above 10 ppm. A similar artifact is slightly visible in  $\delta D$  at 1 ppm.

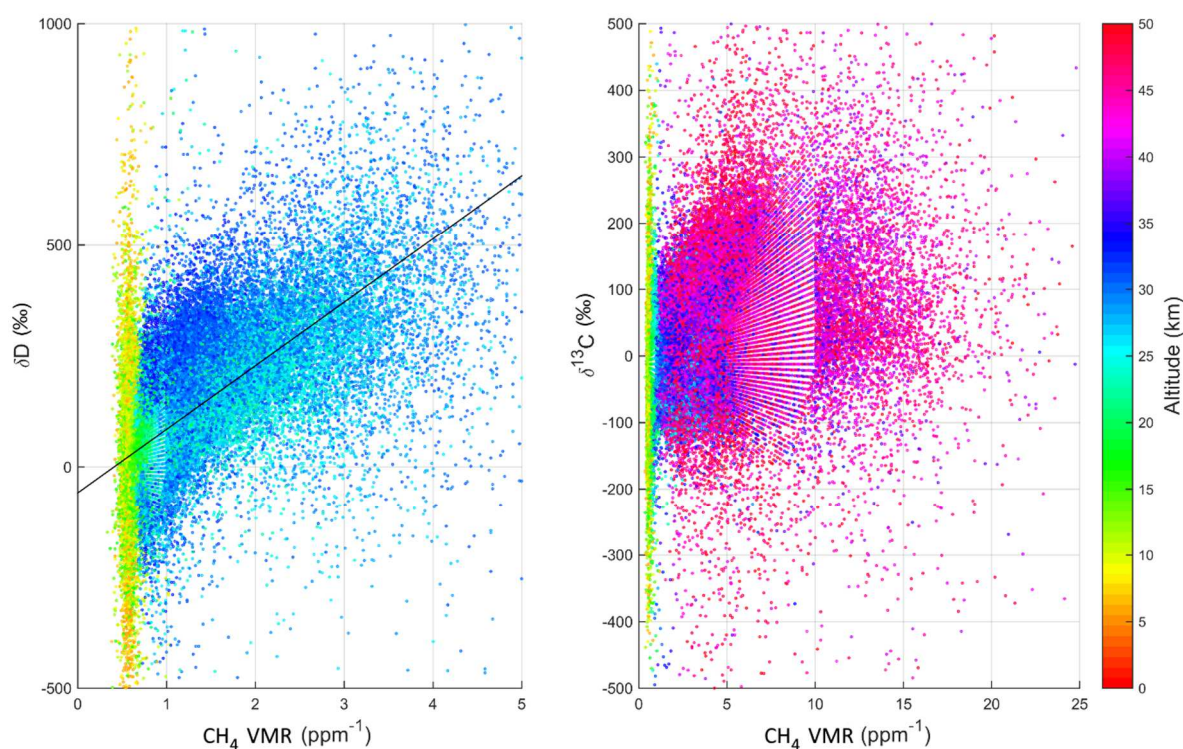


Figure 28. Keeling plots of ACE data for  $\delta D$  (left) and  $\delta^{13}C$  (right). Each measurement is color-coded by its measurement altitude. The streaks of data present in the right figure are artifacts; ACE measurements are retrieved to three significant figures, causing a sharp change in precision around 10  $ppm^{-1}$  (e.g., 9.99 ppm versus 10.1 ppm).

### 5.4.3 Comparison to WACCM output

In general, ACE and WACCM have good qualitative agreement with each other. The most noticeable shared feature between the two is the presence of enriched isotopes over the poles. In the ACE data for CH<sub>3</sub>D, the only visible seasonal change is an increase in  $\delta D$  over the South Pole during the winter (JJA). WACCM also shows this enrichment at the same time. Enrichment over the North Pole is not visible in the ACE data, but WACCM shows that CH<sub>3</sub>D enriched air does not descend to altitudes low enough to be measurable with ACE. In addition, the rapid increase in enrichment at the highest altitudes, 30-35 km, measured by ACE at all latitudes is not present at the same location in WACCM. Increased enrichment is observable above 40 km in WACCM, but the magnitude of this increase is much smaller. This suggests that the feature in ACE is not a real phenomenon, but rather it is possibly some systematic effect associated with the data near the upper altitude limit of the CH<sub>3</sub>D retrievals, a consequence of pushing the retrievals to altitudes where the spectra contain minimal signal from the isotopologue.

Though  $\delta^{13}C$  data from ACE are much noisier than for  $\delta D$ , seasonal enrichment over both poles is visible as the  $\delta^{13}C$  data extend to high altitudes. In both ACE and WACCM, enrichment over the South Pole is most visible in the fall (MAM) months with slightly lower enrichment during the winter (JJA) and spring (SON). The same trend is present over the North Pole in the fall (SON), but again the amount of enrichment fades more rapidly with time as it did with CH<sub>3</sub>D.

However, ACE and WACCM disagree greatly over the values of  $\delta D$  and  $\delta^{13}C$  (Figure 29 and Figure 30). ACE reports values of  $\delta^{13}C$  of over +100‰ in highly enriched areas, while WACCM reports  $\delta^{13}C$  values only up to +5‰ at the altitudes measured by ACE. Tropospheric values are closer, but there is still a disparity: ACE measures  $\delta^{13}C$  around -20‰ while WACCM reports it at around -45‰. The difference is more pronounced with  $\delta D$ . Tropospheric values of  $\delta D$  differ by 100‰ between ACE and WACCM. A quantitative comparison of  $\delta D$  in the stratosphere is more difficult due to the sharp increase seen in ACE.

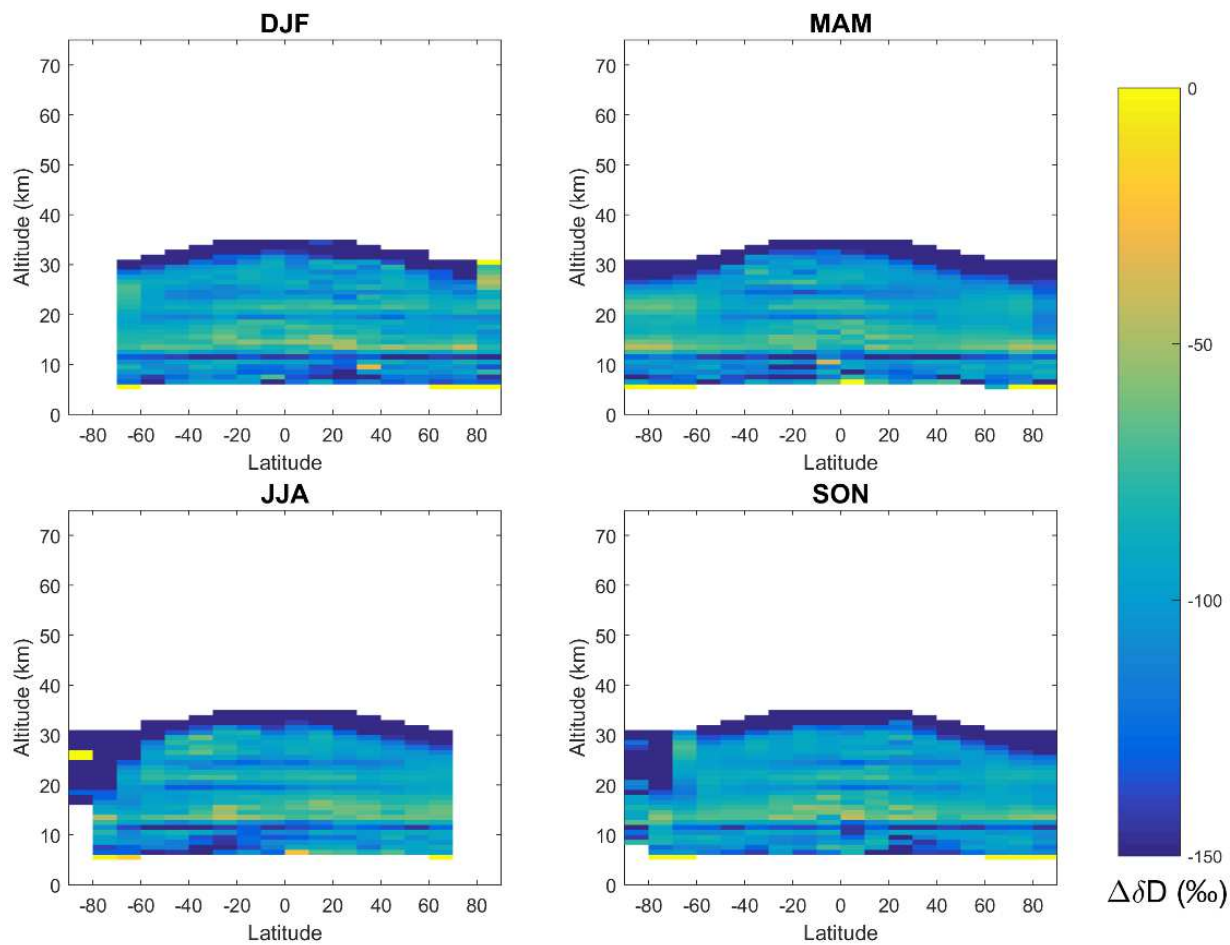


Figure 29. The difference in  $\delta D$  between ACE and WACCM. Negative values are given when ACE reports a larger value than WACCM.

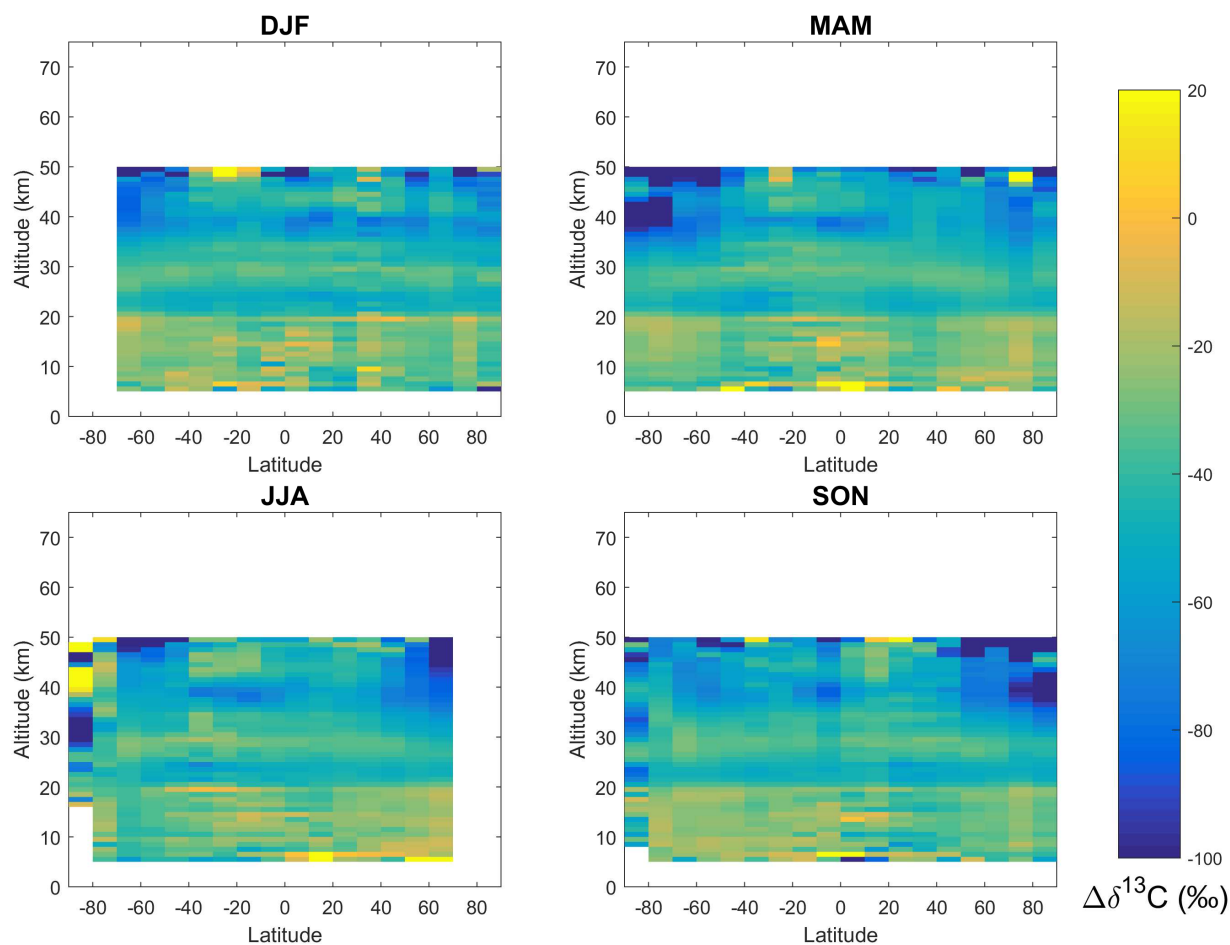


Figure 30. The difference in  $\delta^{13}\text{C}$  between ACE and WACCM. Negative values are given when ACE reports a larger value than WACCM.

Systematic errors in the ACE  $\text{CH}_4$  results are clearly dominated by errors in the spectroscopic constants. Although dramatically improved compared to the preliminary results that used the version 3.5 processing, there remain sharp latitude-independent features at particular altitudes in the fractionation plots in the current study using the research product for main isotopologue  $\text{CH}_4$ . While the new spectroscopic parameters derived for the main isotopologue of  $\text{CH}_4$  significantly improve the fitting residuals and reduce the magnitudes of the sharp features in the fractionation plots, further work is clearly required to refine the quality of these spectroscopic constants. It is not clear at this time what contributions to the systematic features are from the main isotopologue versus the subsidiary

isotopologues. With the magnitudes of the uncertainties involved, there seems little value in generating a formal, quantitative estimate of the systematic error; the errors are large enough (the  $\delta D$  curve was more than 9% different from expectations, and the  $\delta^{13}C$  curve was more than 2% different) to necessitate generating new spectroscopic constants for at least some portion of the  $CH_4$  lines in the microwindows employed for the ACE-FTS retrievals.

#### 5.4.4 Calibration of ACE data

In the troposphere, WACCM's predictions of  $\delta D$  and  $\delta^{13}C$  agree with previous measurements. For  $\delta^{13}C$ , WACCM predicts a tropospheric value of  $-47\text{‰}$ , while measurements range from  $-48\text{‰}$  to  $-46\text{‰}$  (Conny and Currie, 1996; Sugawara et al., 1997; Umezawa et al., 2012). Tropospheric  $\delta D$  measurements have a larger range, between  $-100\text{‰}$  and  $-75\text{‰}$  (Rice et al., 2003; Umezawa et al., 2012). WACCM lies on the high end of this, between  $-81\text{‰}$  and  $-78\text{‰}$ , with more a negative  $\delta D$  in the northern hemisphere. Based on this agreement, WACCM can be used to calibrate ACE by accounting for the unknown systemic error in the ACE retrievals of  $CH_3D$  and  $^{13}CH_4$ . These calibration factors, one for each isotopologue, are a shift applied to  $\delta D$  and  $\delta^{13}C$  from ACE and are equivalent to a multiplication factor applied to the  $CH_3D$  and  $^{13}CH_4$  VMR profiles retrieved by ACE. The calibration factors were derived by taking the difference of the median tropospheric  $\delta$  value for both isotopologues of ACE and WACCM. The height of the tropopause for each ACE profile was taken from derived meteorological products (DMPs) provided by Manney et al. (2007) and was between 8 km and 16 km for most profiles. The calculated calibration shifts are  $-92.4\text{‰}$  for  $\delta D$  and  $-21.8\text{‰}$  for  $\delta^{13}C$ .

The effect of this calibration at one location, the  $60^\circ S$  ACE latitude bin during the spring (SON), is shown in Figure 31. Also shown here are error bars on the post-calibration ACE data. These error bars represent one standard deviation of measurements from the entire data set at that altitude and latitude bin. The calibration is effective for  $CH_3D$  as ACE and WACCM now agree with each other up to 26 km where the sharp increase in  $\delta D$  is observed in ACE. On the other hand, this calibration does not function as well for  $^{13}CH_4$ . After the calibration, ACE and

WACCM agree up to a height of about 20 km, but the bump in the ACE results between 20 and 25 km (associated with the latitude-independent band in the  $\delta^{13}\text{C}$  plots near 22 km mentioned previously) yield significantly poorer agreement in that altitude range. The ACE results also show a stronger increase of  $\delta^{13}\text{C}$  with increasing altitude above 20 km compared to WACCM.

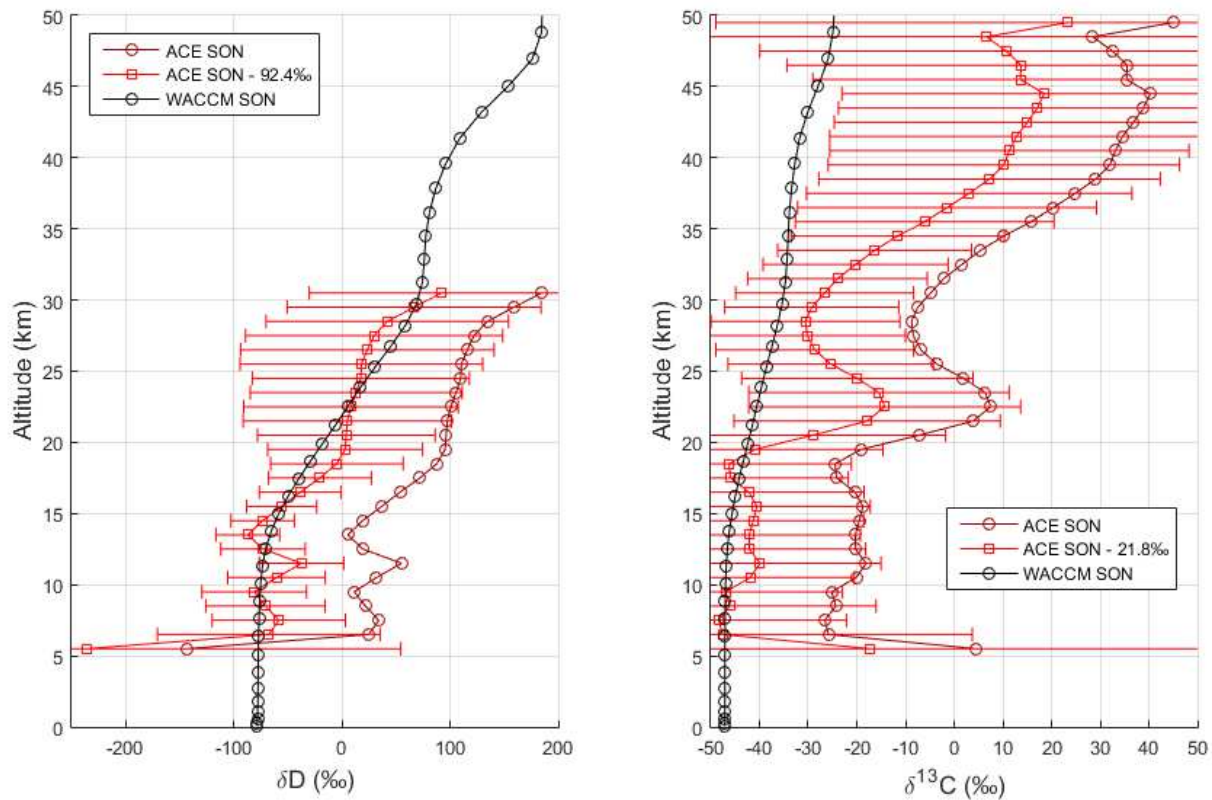


Figure 31. Results of ACE calibration compared to WACCM. Data shown here are from the 60°S September/October/November data bin. The error bars on the calibrated ACE data are equal to one standard deviation of the measurements at that altitude.



#### 5.4.5 Comparison to balloon profiles

ACE data were compared with balloon profiles analyzed by Röckmann et al. (2011). This data set consists of 13 balloon profiles, all of which have data for  $\delta^{13}\text{C}$  and all but two have data for  $\delta\text{D}$ . The balloon launches were performed at Hyderabad, India (17.5°N, 78.60°E), Kiruna, Sweden (67.9°N, 21.10°E), Aire-sur-l'Adour, France (43.70°N, 0.30°E), and Gap, France (44.44°N, 6.14°E). The balloon profiles from each location were compared to ACE profiles from the same season and the 10 degree latitude bin the balloon launches are located in. Both locations in France were considered together since only one launch was performed at Gap.

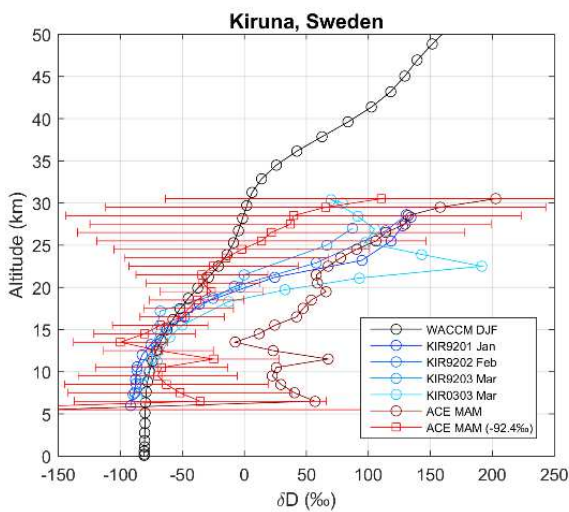
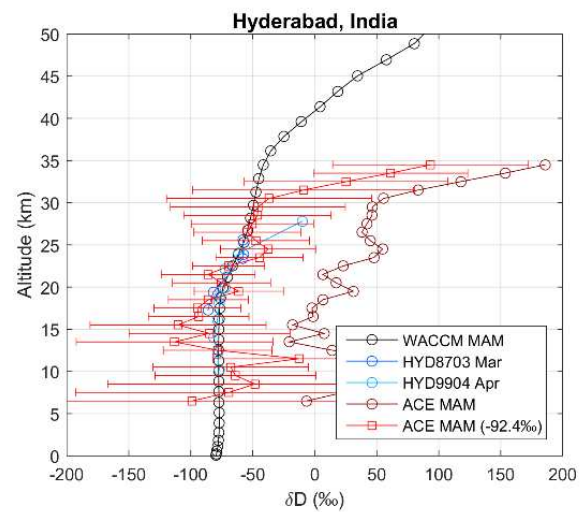
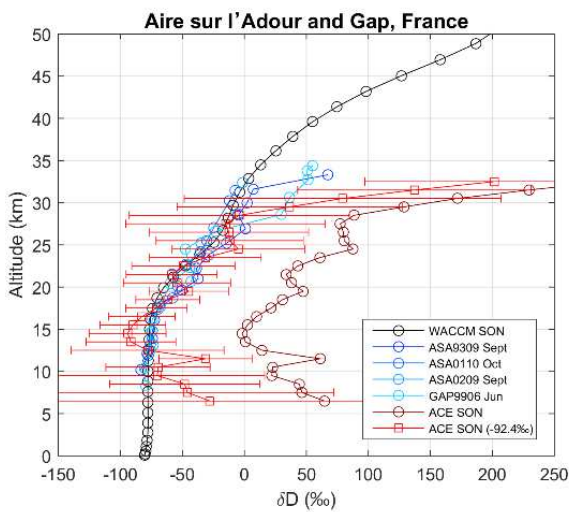


Figure 32 shows the comparison of  $\delta D$  among ACE (shown in red), WACCM (gray and black), and the balloon profiles (blue). The profiles over India and both locations in France show strong agreement among all three data sets to above 25 km. Over India, the balloon profiles end below 30 km, so there are no data to compare to the highest altitudes of ACE where  $\delta D$  rapidly increases. Over France, the balloon profiles reach as high as 33 km, slightly higher than ACE, but do not show the spike in  $\delta D$  present in ACE. This, along with the high amount of random error present in the retrieval at this altitude, supports the notion that the rapid increase in  $\delta D$  at the highest altitudes in the ACE results is a retrieval artifact. One profile, ASA9309, does show increased  $\delta D$  at the single highest point, but this is not conclusive. On the other hand, the profiles over Sweden do not show such agreement. Above 20 km, the balloon profiles show a large increase and noticeable month-to-month changes in  $\delta D$ , whereas ACE shows a more gradual rise. The sharp increase is likely due to strong influence from the polar vortex during the two years of measurements. The ACE data is a combination of 10 years of profiles, so years of strong vortex influence are balanced by years with less influence. Also, the run of WACCM does not include any interannual variation, so the effect of an average polar vortex is expected.

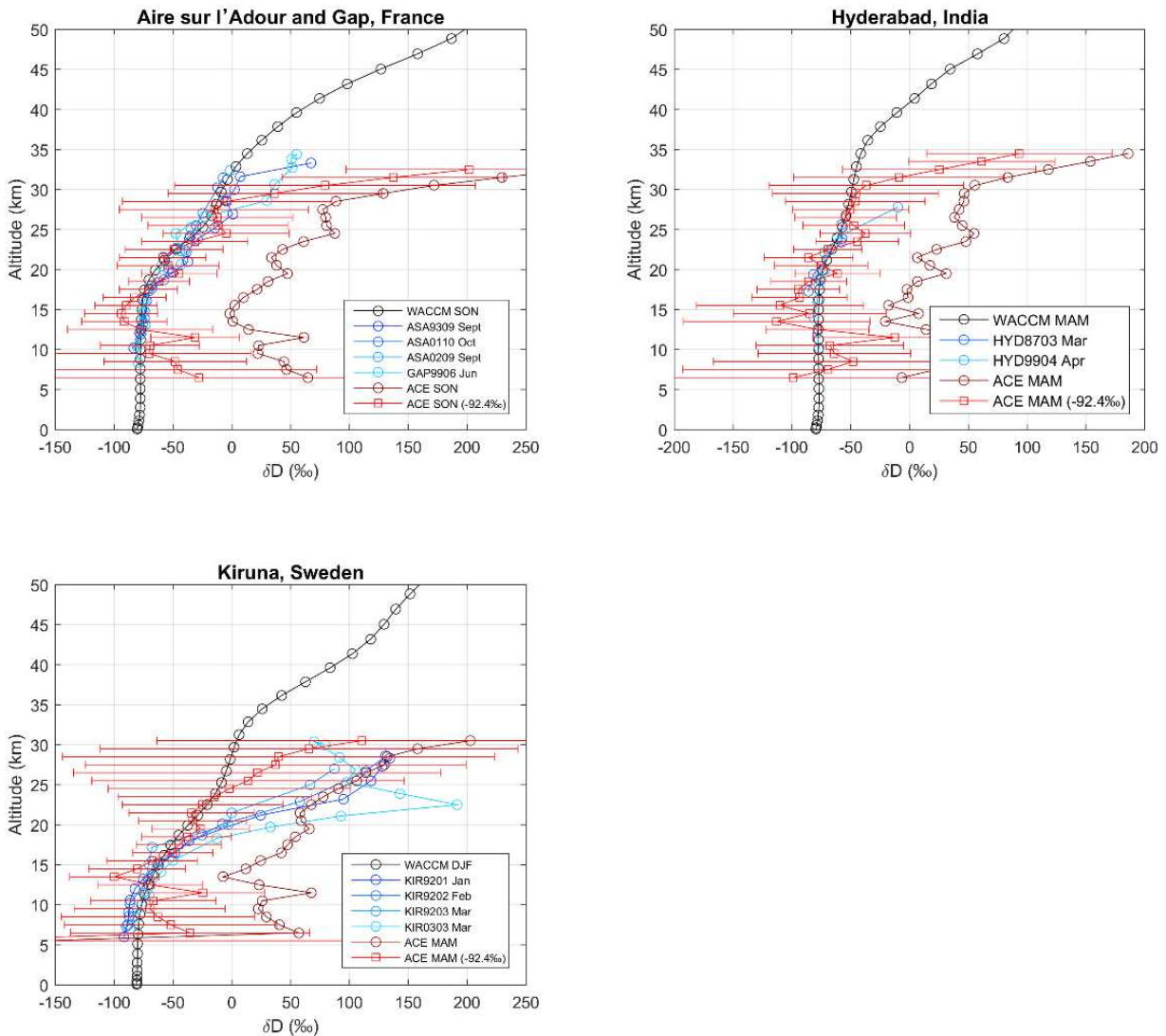


Figure 32. Comparison of  $\delta D$  profiles from ACE before and after calibration, WACCM, and balloon profiles from Röckmann et al. (2011).

Figure 33 shows the comparison of the three data sets for  $\delta^{13}C$ . Quantitatively, agreement is generally poorer between ACE and the balloon profiles than was observed for  $\delta D$ . Excluding the apparent artifact in the ACE  $\delta^{13}C$  results (the bump between 20 and 25 km), there is reasonable agreement for the balloon measurements over India. For the higher latitude measurements over France and Sweden, ACE indicates a smaller isotopic fractionation in the troposphere than was measured by the balloon campaign or predicted by WACCM. Interestingly, the

balloon measurements in Sweden show fairly good agreement with the bump between 20 and 25 km in the ACE  $\delta^{13}\text{C}$  results, but since this bump in the ACE results is thought to be an artifact, this agreement is probably a coincidence.

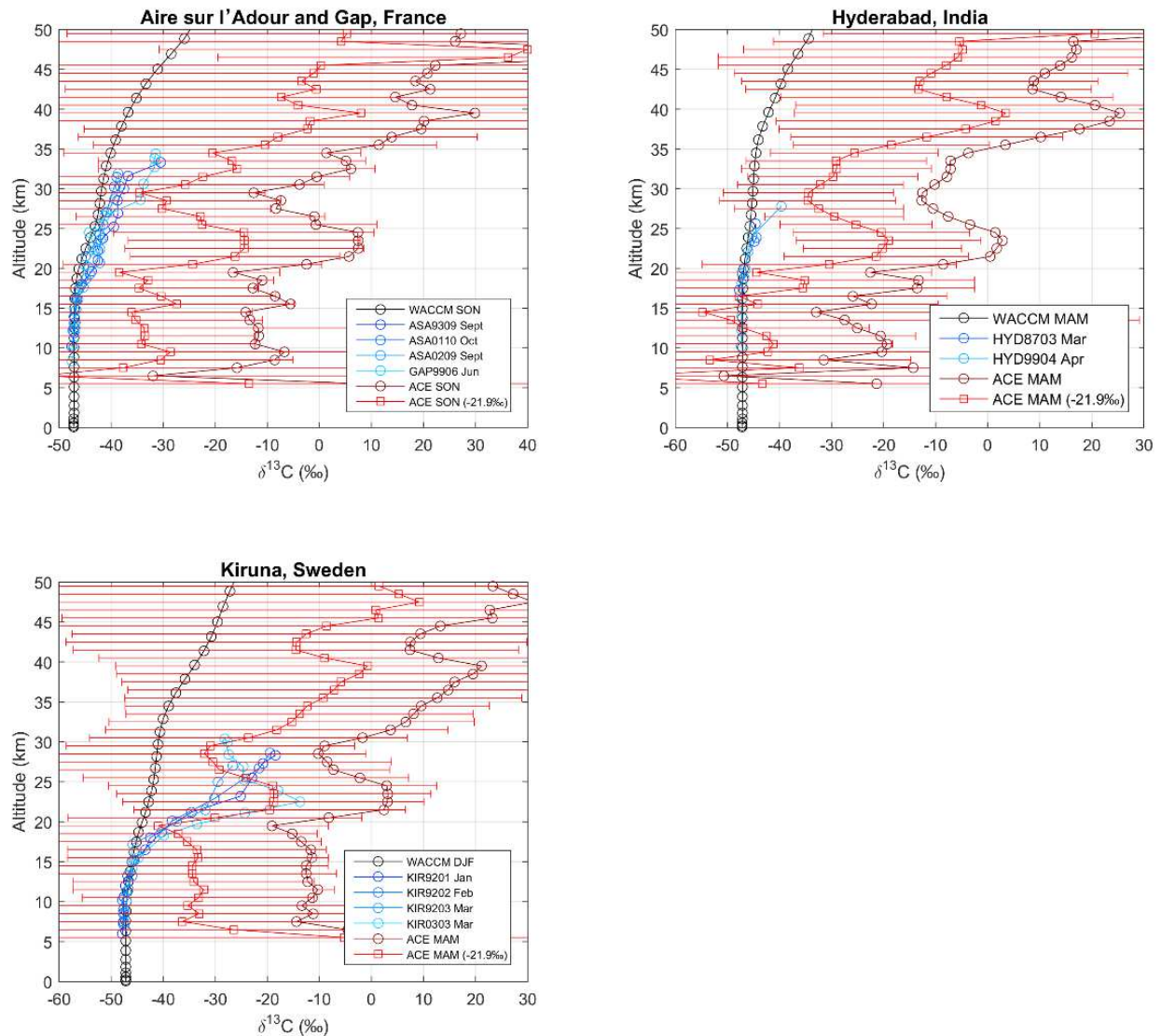


Figure 33. Comparison of  $\delta^{13}\text{C}$  profiles from ACE before and after calibration, WACCM, and balloon profiles from Röckmann et al. (2011).

#### 5.4.6 Distribution of methane sinks

A second set of WACCM runs were performed to further explore the effects of the different sinks of methane on its isotopic composition. The model was run an additional year past the initial 20 years. Then, several one day branch runs were performed on the first day of each month of the extra year. In these runs, the reactions for methane with OH, O (<sup>1</sup>D), Cl and sunlight (photolysis) were modified to additionally produce an inert dummy molecule. The abundance of this “molecule” at a specific location shows how much methane reacted with a specific molecule or via photolysis at that location. Since the model reports molecular concentrations as mixing ratios, the abundance of the dummy molecules is relative to the number density of air at that location. The mixing ratios of the dummy molecules are on the order of 10<sup>-9</sup> or smaller, so their presence does not have a large effect on the pressure or other dynamics in the atmosphere.

Figure 34 shows the results of these runs for the months of January, April, July, and October. The plots in the left column show which of the four sinks destroys the most methane at a given latitude and altitude. The right column shows the total rate of methane destruction. OH is the most important oxidant in the troposphere and most of the stratosphere outside of the polar regions. From 50 to 65 km, singlet oxygen becomes the largest oxidant. It is also the largest oxidant between 30 and 40 km at the equator, likely due to the presence of the ozone layer below which readily photolyzes to give oxygen atoms. Above 65 km, photolysis becomes the major source of methane destruction as the atmosphere becomes thinner, making chemical reactions more difficult and allowing the increased penetration of UV radiation.

The reaction of methane with chlorine atoms demonstrates strong seasonal variation. Oxidation via chlorine is only dominant over the poles in the stratosphere around the winter months. At the same time over the poles, methane destruction reaches its lowest rates. This is due to the presence of the polar vortex. The isolated air inside the vortex is not exposed to sunlight, so oxidizing radicals are quickly consumed and are not regenerated. Meanwhile, active chlorine-containing

compounds build up within the vortex, providing a small source of chlorine atoms even with minimal sunlight.

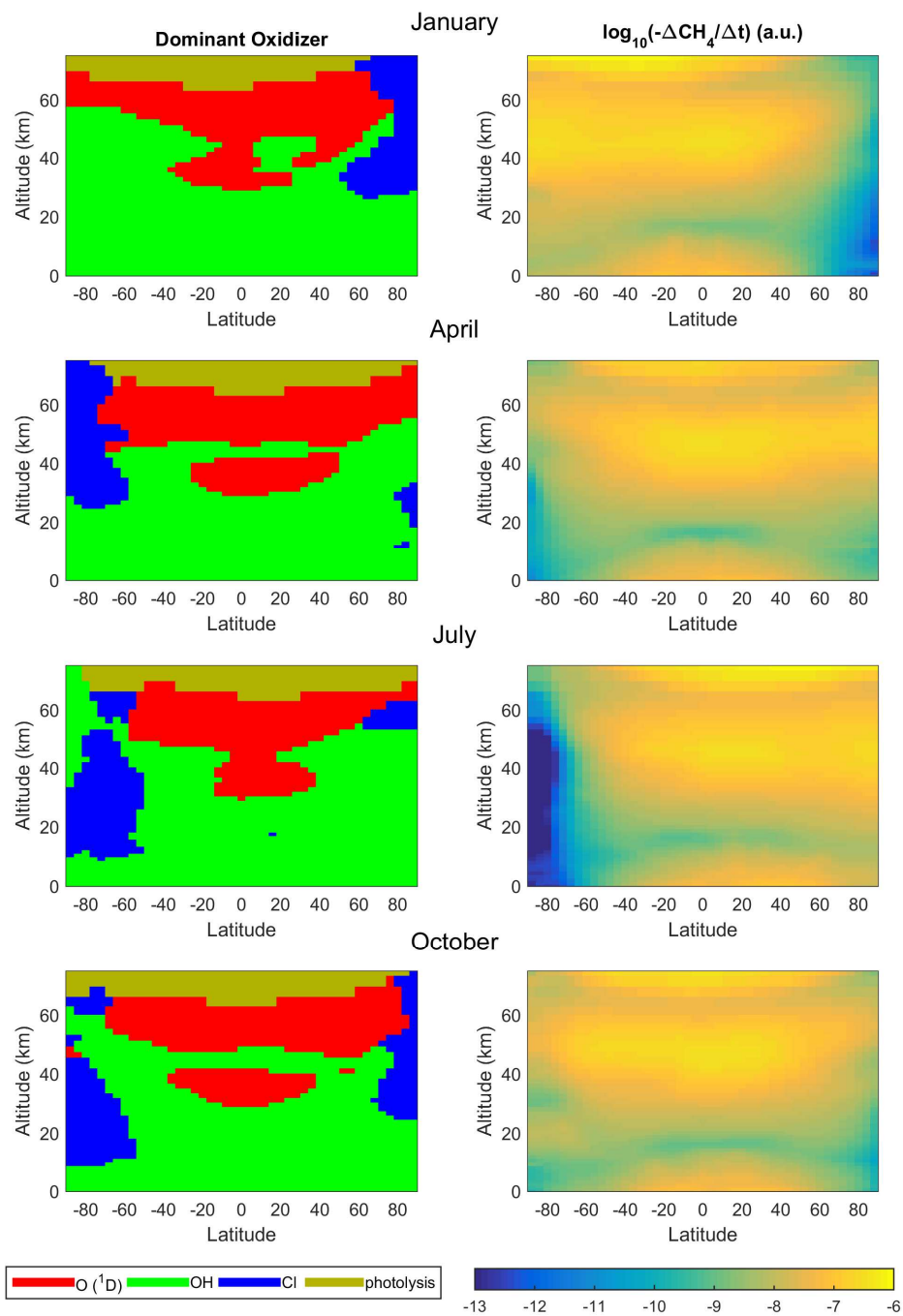


Figure 34. Dominant oxidizing species of CH<sub>4</sub> by location and season (left) and total methane oxidation (right).

## 5.5 Conclusions

The ACE data set presented in this chapter greatly expands the number of observations of methane and its isotopologues in the stratosphere. The data for CH<sub>3</sub>D have been shown to be consistent with both model predictions and existing balloon-based measurements after calibrating the ACE results using tropospheric  $\delta D$  calculated from the WACCM model. However, the data for <sup>13</sup>CH<sub>4</sub> still show large discrepancies. The addition of new microwindows and adjustment of spectroscopic parameters for CH<sub>4</sub> lines in the 2ν<sub>4</sub> band significantly reduced the large step function observed in  $\delta^{13}C$  when using the spectroscopic parameters for this band that are currently available in the HITRAN database. However, a systematic latitude-independent bump near 22 km in the  $\delta^{13}C$  profiles derived from ACE in the current study suggest that further refinement of these spectroscopic constants will be required to improve the retrieval results for the isotopologues CH<sub>4</sub> from ACE.

## **<sup>13</sup>CO MEASUREMENTS IN THE STRATOSPHERE AND MESOSPHERE**

### **6.1 Introduction**

Carbon monoxide (CO) is another important trace gas in the atmosphere. It is a weak greenhouse gas as it does not strongly absorb infrared light. However, its chemistry in the atmosphere, especially with the OH radical, has a large influence on the activity of other greenhouse gases, so it is considered an indirect greenhouse gas. It has a short lifetime, 2 months, making it a useful tracer for transport and causing large horizontal variation in its concentration.

CO has several sources in the troposphere: the incomplete combustion of fossil fuels and biomass on the surface, and the oxidation of methane and non-methane hydrocarbons (NHMCs) in the air. The isotopic signatures of each of these sources are given in Figure 35 (Park et al., 2015). Although the budget of CO is not well constrained, surface and oxidation sources are believed to be roughly equal in strength. Anthropogenic activities such as deforestation, burning of savanna and waste, and fossil fuel use make up 85% of surface sources; about half of atmospheric oxidation can be attributed to anthropogenic activity as well. (Ehhalt and Prather, 2001).

CO concentrations have risen greatly since the industrial era due to these anthropogenic sources. Ice core measurements from Greenland and Antarctica give an atmospheric concentration of ~90 ppb between 1600 and 1850 (Haan et al., 1996; Haan and Raynaud, 1998). Recently, CO concentrations are higher in the Northern Hemisphere due to the larger presence of anthropogenic emissions there combined with the short lifetime of CO compared to interhemispheric mixing. At the North Pole, CO ranges from 60 ppb in the summer to 200 ppb in the winter. Over the South Pole, CO is about 30 ppb in the summer and 65 ppb in the winter (Ehhalt and Prather, 2001). Recent trends of CO concentration have varied. An increasing abundance of CO was observed at Barrow, Alaska between 1979 and 1987 (Khalil and Rasmussen, 1984), but a decreasing trend was observed at the same location from 1988 to 1993 (Khalil and Rasmussen, 1994; Novelli et al., 1994).



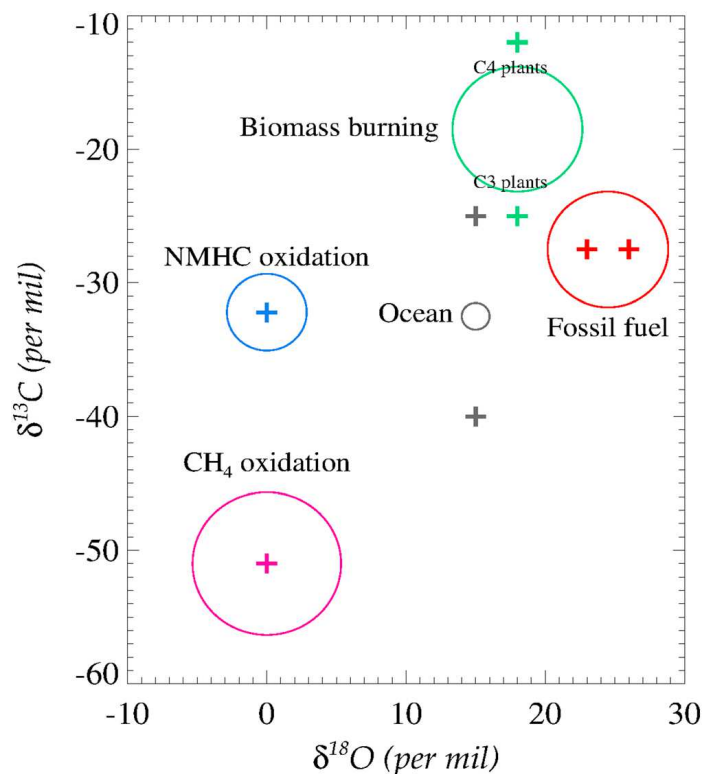
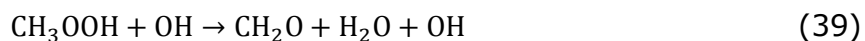
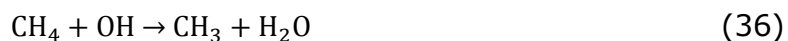


Figure 35:  $\delta^{13}\text{C}$  and  $\delta^{18}\text{O}$  isotopic signature of CO sources in the troposphere. From Park et al. (2015)

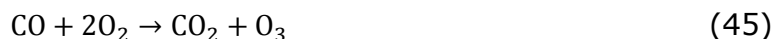
The oxidation of  $\text{CH}_4$  to CO is a multistep process that passes through several intermediates. The primary reaction pathway is as follows:



The only major sink of CO is the reaction with OH. This reaction has a strong influence on several other greenhouse gases. First, the reaction produces  $\text{CO}_2$ , the most important greenhouse gas. In addition, CO competes with  $\text{CH}_4$  to react with OH, increasing the lifetime of  $\text{CH}_4$  when CO is present. Finally, under high  $\text{NO}_x$  conditions, ozone is a byproduct of CO oxidation:



The net reaction is



Due to its indirect climate forcing effects, CO was given a Global Warming Potential (GWP) of 2 over 20 – 500 years in the first IPCC report (Shine et al., 1990), though this rating was later abandoned for indirect gases. Modeling performed by Daniel and Solomon (1998) suggested that forcing due to anthropogenic CO is stronger than that of anthropogenic N<sub>2</sub>O. Wild and Prather (2000) concluded that emissions of 100 kg of CO has the equivalent climate forcing of 5 kg of CH<sub>4</sub>.

In the mesosphere, both the concentration and lifetime of CO are higher. Here, carbon cycles between CO and CO<sub>2</sub> via the oxidation of CO and the photolysis of CO<sub>2</sub>. Above 50 km, CO concentrations increase exponentially with height up to 20-100 ppm at 100 km (López-Puertas et al., 2000). CO<sub>2</sub> decreases with height in the mesosphere since CO<sub>2</sub> photolysis is stronger than CO chemical loss, causing CO as a fraction of all carbon species to reach over 20% at 100 km. Modeling and observations by ACE-FTS indicate that mesospheric CO varies with the solar cycle while CO<sub>x</sub> (CO + CO<sub>2</sub>) increased between 2004 and 2011 (Emmert et al., 2012).

Several previous studies have measured CO and the <sup>13</sup>CO isotopologue in the troposphere and stratosphere. In situ sample collection and measurements are made somewhat difficult by the low abundance of CO and the complexity of isolating it from ambient air. The routine method uses a series of cryogenic traps, oxidation to CO<sub>2</sub>, and detection with continuous flow GC-MS (Brenninkmeijer et al., 1999; Stevens and Krout, 1972). Measurements of CO and <sup>13</sup>CO have been made allocations such as Svalbard and northern Canada (Röckmann et al., 2002), Japan (Kato et al., 2000), Barbados, (Mak, 2003), and the Trans-Siberian railroad (Bergamaschi et al., 1998). The CARIBIC project routinely collects CO isotopologues in the upper troposphere and lower stratosphere, but its early measurements had artificially high levels of CO (Gromov and Brenninkmeijer, 2015). However, large spatial coverage is important for CO given its short lifetime

and seasonal variability, something that in situ measurements cannot provide. Various satellite-based instruments collect data on CO including SCIAMACHY (de Laat et al., 2006), MOPITT (Deeter, 2003), MIPAS (Funke et al., 2009), and IASI (George et al., 2009), but none of these have observed isotopologues of CO.

This chapter presents ACE-FTS data of  $^{12}\text{CO}$  and  $^{13}\text{CO}$  as well as a matching model run performed with WACCM. The following is adapted from a paper published in the Journal of Molecular Spectroscopy (Beale et al., 2016) and uses contributing work from C. Beale (ACE-FTS data analysis), C. Boone (ACE-FTS retrievals), and P. Bernath (supervisor). Text from other authors has not been used here.

## 6.2 Methods

Retrievals from ACE-FTS of CO and  $^{13}\text{CO}$  use version 3.5 of the ACE-FTS software (Boone et al., 2013). Above  $\sim 95$  km, version 3.5 differs significantly from the previous version 3.0. In the old version, CO concentrations in the thermosphere were assumed to increase rapidly with altitude. This resulted in an overestimation in the contribution of the region above 110 km, above the highest measured altitude, to the calculated spectra used in the retrieval process. In version 3.5, CO VMR is assumed to be constant above 110 km. A total of 25,855 occultations are used in the ACE dataset in this study.

The microwindows used for  $^{12}\text{CO}$  retrievals cover the fundamental (1-0) and first overtone (2-0) vibrational bands, located around  $2143\text{ cm}^{-1}$  and  $4259\text{ cm}^{-1}$  respectively. Lines in the fundamental bands are used at higher altitudes while the overtone band lines are used low where stronger lines become saturated. For  $^{13}\text{CO}$ , only the fundamental band, located at approximately  $2090\text{ cm}^{-1}$ , is used. A complete list of the lines used for retrievals of both species is given in Tables 16 and 17 in the Appendix.

The two CO Isotopologues are retrieved independently with their own sets of microwindows. But as for other ACE retrievals, some interfering species that have spectral features within the microwindow set are retrieved simultaneously with the target species. For some interfering molecules, extra microwindows containing features primarily from the interferer are used to improve convergence of the least-

squares fitting. For the main isotopologue, the interferers in the version 3.5 microwindow set were  $\text{H}_2\text{O}$ ,  $\text{H}_2^{17}\text{O}$ ,  $\text{CO}_2$ ,  $^{18}\text{O}^{12}\text{C}^{16}\text{O}$ ,  $^{17}\text{O}^{12}\text{C}^{16}\text{O}$ ,  $\text{O}_3$ ,  $^{18}\text{O}^{16}\text{O}^{16}\text{O}$ ,  $\text{N}_2\text{O}$ ,  $^{15}\text{NNO}$ ,  $\text{N}^{15}\text{NO}$ ,  $^{13}\text{CO}$ ,  $\text{C}^{18}\text{O}$ ,  $\text{CH}_4$ , and  $\text{OCS}$ . For  $^{13}\text{CO}$ , the interferers were  $\text{H}_2\text{O}$ ,  $\text{H}_2^{18}\text{O}$ ,  $\text{H}_2^{17}\text{O}$ ,  $\text{CO}_2$ ,  $^{13}\text{CO}_2$ ,  $^{18}\text{O}^{12}\text{C}^{16}\text{O}$ ,  $^{17}\text{O}^{12}\text{C}^{16}\text{O}$ ,  $\text{O}_3$ ,  $^{18}\text{O}^{16}\text{O}^{16}\text{O}$ ,  $^{16}\text{O}^{18}\text{O}^{16}\text{O}$ ,  $^{17}\text{O}^{16}\text{O}^{16}\text{O}$ ,  $^{16}\text{O}^{17}\text{O}^{16}\text{O}$ ,  $\text{N}_2\text{O}$ ,  $^{12}\text{CO}$ ,  $\text{C}^{18}\text{O}$ ,  $\text{CH}_4$ , and  $\text{OCS}$ . Note that  $^{12}\text{CO}$  and  $^{13}\text{CO}$  do interfere with each other, but the profile of the non-target molecule is discarded.

ACE-FTS measurements of  $^{12}\text{CO}$  have previously been validated with other satellite, airborne, and ground-based measurements (Clerbaux et al., 2008). Retrievals errors are within 5% from the upper troposphere to 40 km and 10% above 40 km. The CO data produce differs from previous versions with small changes in the stratosphere compared to version 2.2 and the high-altitude corrections previously mentioned compared to version 3.0. Validation has shown that these corrections make ACE a viable platform for  $^{12}\text{CO}$  measurements from the troposphere up to 110 km. However,  $^{13}\text{CO}$  from ACE has not yet been validated.

The WACCM run used in this chapter is based on the previous  $\text{CH}_4$  run from the previous chapter with additional modifications used to track  $^{13}\text{C}$  along the oxidation of  $\text{CH}_4$  to  $\text{CO}_2$ . The list of modified reactions is given in Table 7. Although some of these reactions show temperature and/or pressure dependence (Brenninkmeijer et al., 1999), the KIEs were inserted into the model as constants. This is expected to cause a small but increasing amount of error at higher altitudes where pressure and temperature decrease. In addition, the photolysis of  $\text{CO}_2$  is the major source of CO at high altitudes and each isotopologue has a different absorption cross section for a given wavelength. At wavelengths above 150 nm, theoretical values for each isotopologue's cross section are used (Schmidt et al., 2013). Below 150 nm, where theoretical cross sections were not calculated, experimental values (Yoshino et al., 1996) for  $^{12}\text{C}^{16}\text{O}$  are used for both isotopologues. Isotopic differences for other photochemical reactions were not included.

Table 7: Reactions important to CO isotopic chemistry and corresponding KIE values. All reactions are reported at 298 K and 1 atm.

Reaction	$k_{12}/k_{13}$	Source
$\text{CH}_4 + \text{OH} \rightarrow \text{CH}_3\text{O}_2 + \text{H}_2\text{O}$	1.00288	(Sander et al., 2006)
$\text{CH}_3\text{Cl} + \text{Cl} \rightarrow \text{HO}_2 + \text{CO} + 2 \text{HCl}$	1.07	(Gola et al., 2005)
$\text{CH}_2\text{O} + \text{NO}_3 \rightarrow \text{CO} + \text{HO}_2 + \text{HNO}_3$	0.96	(Feilberg et al., 2004)
$\text{CH}_2\text{O} + \text{OH} \rightarrow \text{CO} + \text{H}_2\text{O} + \text{H}$	0.952	(Feilberg et al., 2004)
$\text{CH}_2\text{O} + \text{Br} \rightarrow \text{HBr} + \text{HO}_2 + \text{CO}$	1.13	(Feilberg et al., 2004)
$\text{CH}_2\text{O} + \text{Cl} \rightarrow \text{HCl} + \text{HO}_2 + \text{CO}$	1.058	(Feilberg et al., 2004)
$\text{CO} + \text{OH} + \text{M} \rightarrow \text{CO}_2 + \text{HO}_2 + \text{M}$	1.00597	(Röckmann et al., 1998)
$\text{CO}_2 + h\nu \rightarrow \text{CO} + \text{O}$	varies	(Schmidt et al., 2013; Yoshino et al., 1996)

Lower boundary conditions representing surface emissions were added to WACCM for CO and  $^{13}\text{C}$ O. Boundary conditions for  $\text{CH}_4$  and  $\text{CO}_2$  are already present in the model, so these two molecules were modified to include their heavy isotopologues. Data for surface CO concentrations were collected from the NOAA ESRL Carbon Cycle Cooperative Global Air Sampling Network (Andrews et al., 2014) and interpolated over all latitudes. The boundary conditions for  $^{13}\text{C}$ O were calculated using  $\delta^{13}\text{C}$  measurements from the work of Bergamaschi et al. (2000). Data from the Northern and Southern Hemisphere were averaged separately. For  $\text{CH}_4$  and  $\text{CO}_2$ , the following  $[\text{CH}_4] - \delta^{13}\text{C}$  and  $[\text{CO}_2] - \delta^{13}\text{C}$  relations were derived from experimental data by Röckmann et al. (2011), and Assonov et al. (2010),

$$\delta^{13}\text{C} (\text{CH}_4)/\text{‰} = \frac{1.29 \times 10^4}{[\text{CH}_4]/(\text{ppm})} - 151.4$$

$$\delta^{13}\text{C} (\text{CO}_2)/\text{‰} = \frac{6.47 \times 10^3}{[\text{CO}_2]/(\text{ppm})} - 25.3$$

These relations were combined with WACCM's out-of-the-box boundary condition data (Lamarque et al., 2010) to calculate boundary conditions for each isotopologue.

WACCM was run as a resolution of  $4^\circ$  latitude  $\times$   $5^\circ$  longitude with 66 vertical levels from the surface to  $5 \times 10^{-6}$  hPa ( $\sim 140$  km) for a period of 20 years as an eternal year 2000; the final three years were used for analysis.

In all figures in this chapter, data is binned by season (Dec/Jan/Feb, Mar/Apr/May, Jun/Jul/Aug, and Sept/Oct/Nov) and by 10° latitude. ACE data is a total mission average from 2004 to 2011, while WACCM data comes from the final 3 years of the run. Data from WACCM is analyzed in two forms: the full data set and an “ACE sampled” data set, where VMR profiles are sampled at the same times and locations as each ACE occultation.

## **6.3 Results and Discussion**

### *6.3.1 ACE-FTS data set*

Figure 36 shows the total CO VMR on a logarithmic scale from 25,855 occultations from the ACE dataset. CO VMRs lie around 100 ppb and decrease to between 20 ppb and 50 ppb in the stratosphere. This is consistent with previous satellite measurements (Clerbaux et al., 2008). CO VMRs are at their lowest in the lower stratosphere where oxidation via OH is strong and UV light is insufficient to photolyze CO<sub>2</sub> to CO. CO VMRs increase rapidly from the upper stratosphere into the mesosphere and lower thermosphere where CO<sub>2</sub> photolysis becomes more important. At 100 km, the CO VMR ranges from 25 ppm to 70 ppm. Some seasonal variation is apparent at the poles. Over the winter pole, CO-rich air from the mesosphere sinks into the stratosphere.

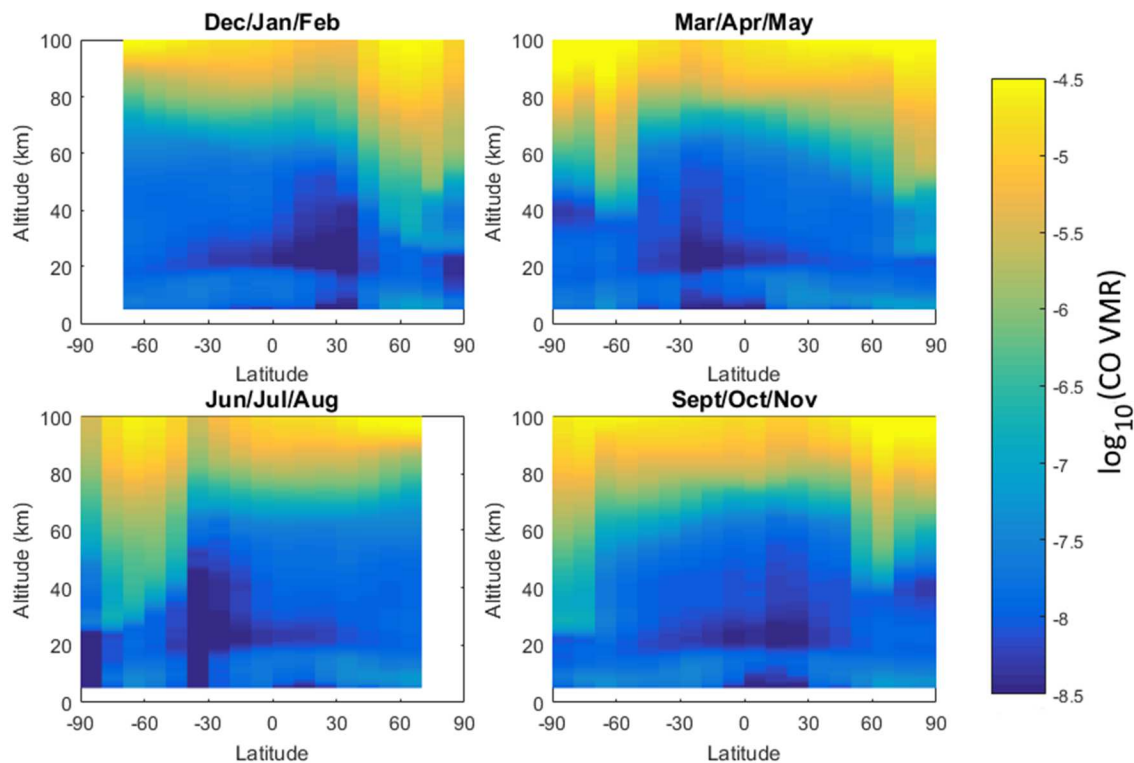


Figure 36: Total CO VMR by season from ACE

Figure 37 shows  $\delta^{13}\text{CO}$  values from the ACE data set. Data for  $^{13}\text{CO}$  is available from 5 km to 90 km at all latitudes. As with total CO, strong seasonal variation is apparent in the mesosphere. Here, photolysis of  $\text{CO}_2$  produces CO. This reaction has a strong normal kinetic isotope effect, causing an enrichment in  $^{12}\text{CO}$  (and  $^{13}\text{CO}_2$ ) and in turn lower values of  $\delta^{13}\text{CO}$ .  $\delta^{13}\text{CO}$  increases with altitude and is especially high above 80 km, suggesting the thermosphere is enriched in  $^{13}\text{CO}$ . This enriched air is seen descending over the winter pole much like in Figure 36 with total CO. From about 87 km upward  $\delta^{13}\text{CO}$  rapidly drops, but this is likely poor data at the edge of the measurement range of  $^{13}\text{CO}$ .

In the stratosphere and troposphere, seasonal variation is not as strong. Three areas of heavy enrichment are present: a band at 40 km at all latitudes except the winter pole, a pair of bands at 12 km over the mid and high latitudes, and a broad area centered at 20 km over the Equator. The origins of these highly-enriched areas are discussed in Section 6.3.3. Outside of these areas,  $\delta^{13}\text{CO}$  in the lower

stratosphere are around  $-50\text{‰}$ , consistent with the isotopic signature of CO produced from methane oxidation (Park et al., 2015)

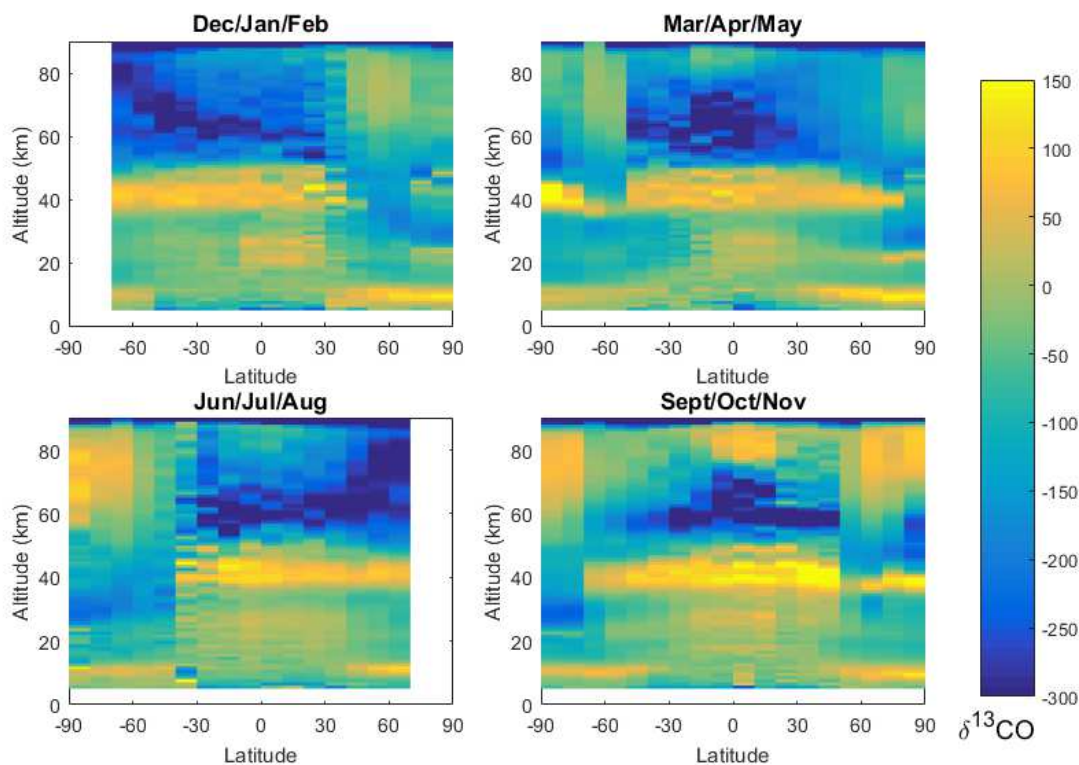


Figure 37: Seasonal variation of  $\delta^{13}\text{CO}$  as a function of latitude observed by ACE

### 6.3.2 WACCM data set

CO VMRs from the full WACCM data set are shown in Figure 38. Here, the differing tropospheric CO concentrations between the two hemispheres are more apparent. CO VMRs range from 80 ppb to 180 ppb in the Northern Hemisphere and 40 to 60 ppb in the Southern Hemisphere. Note that this difference is difficult to see in Figure 38 due to the logarithmic scale. In the lower stratosphere, CO drops to as low as 13 ppb before increasing with height. As with ACE, high concentrations of CO are present in the mesosphere and lower thermosphere and convect down over the winter pole, though the gradients are much smoother in WACCM than in ACE.



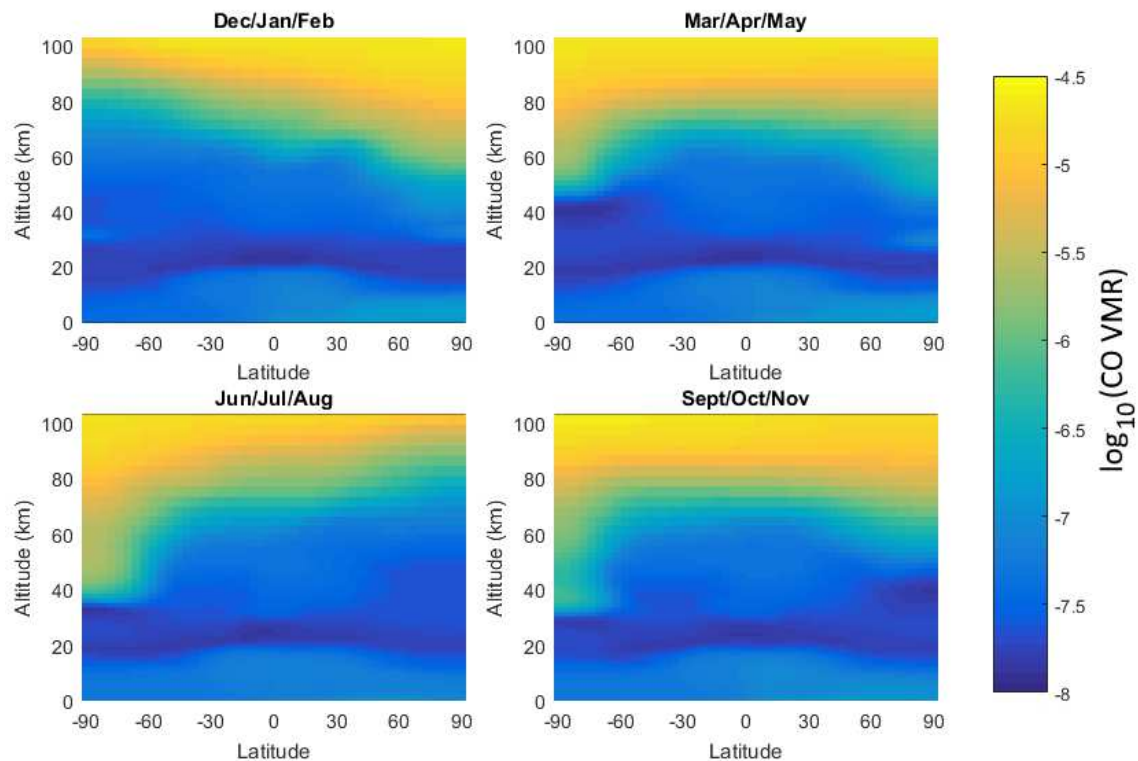


Figure 38: Total CO VMR by season from the full WACM data set

Values of  $\delta^{13}\text{CO}$  from the full WACCM data set are shown in Figure 39. Much like in the ACE dataset, the mesosphere has areas of low  $^{13}\text{CO}$  due to  $\text{CO}_2$  photolysis and wintertime downwelling of  $^{13}\text{CO}$ -rich air from the thermosphere. The troposphere and stratosphere differ greatly from the ACE dataset. The three areas of heavy enrichment are not present. Instead, the two layers have a distinct and narrow range of  $\delta^{13}\text{CO}$  values with a sharp transition at the tropopause. In the troposphere,  $\delta^{13}\text{CO}$  lies between  $-25\text{‰}$  in the Southern Hemisphere and  $-30\text{‰}$  in the Northern Hemisphere. This is closer to a median value of  $\delta^{13}\text{CO}$  from all tropospheric sources and likely represents combined contributions of each of them (Park et al., 2015). Stratospheric values are around  $-60\text{‰}$  except in the upper stratosphere over the winter pole.

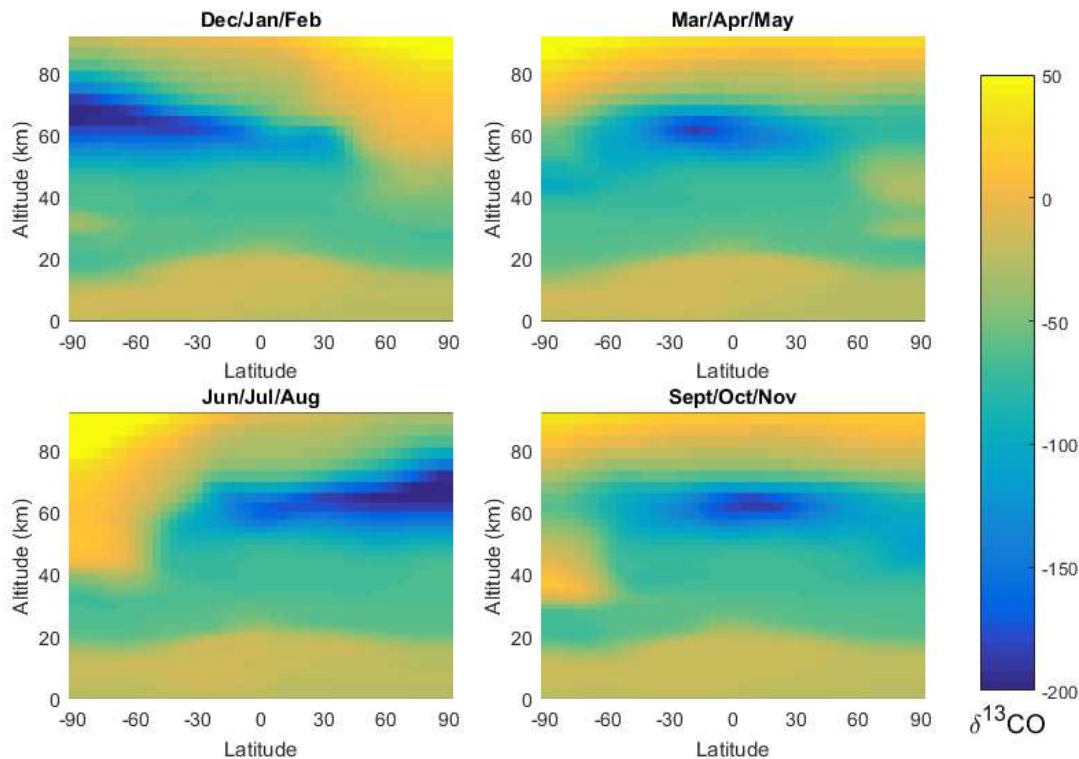


Figure 39:  $\delta^{13}\text{CO}$  by season from the full WACCM data set

### 6.3.3 Comparison of ACE and WACCM

While total CO VMRs from ACE (Figure 36) and WACCM (Figure 38) show the same general features, the exact shapes of these features differ. At some altitudes, ACE shows a sharp change in CO concentration from low to high latitudes, while the gradient is smoother in WACCM. Also, the area of CO-poor air in the stratosphere reaches higher around  $30^\circ$  in both hemispheres during the winter. Sampling WACCM in the same manner as ACE (Figure 40) reproduces these features as they are seen in ACE. This demonstrates that the shape of these features is due to the sampling bias of ACE, which makes the majority of its measurements around  $60^\circ$  (Figure 21). It also shows that WACCM can accurately replicate the basic chemistry and dynamics of CO as observed by ACE-FTS.

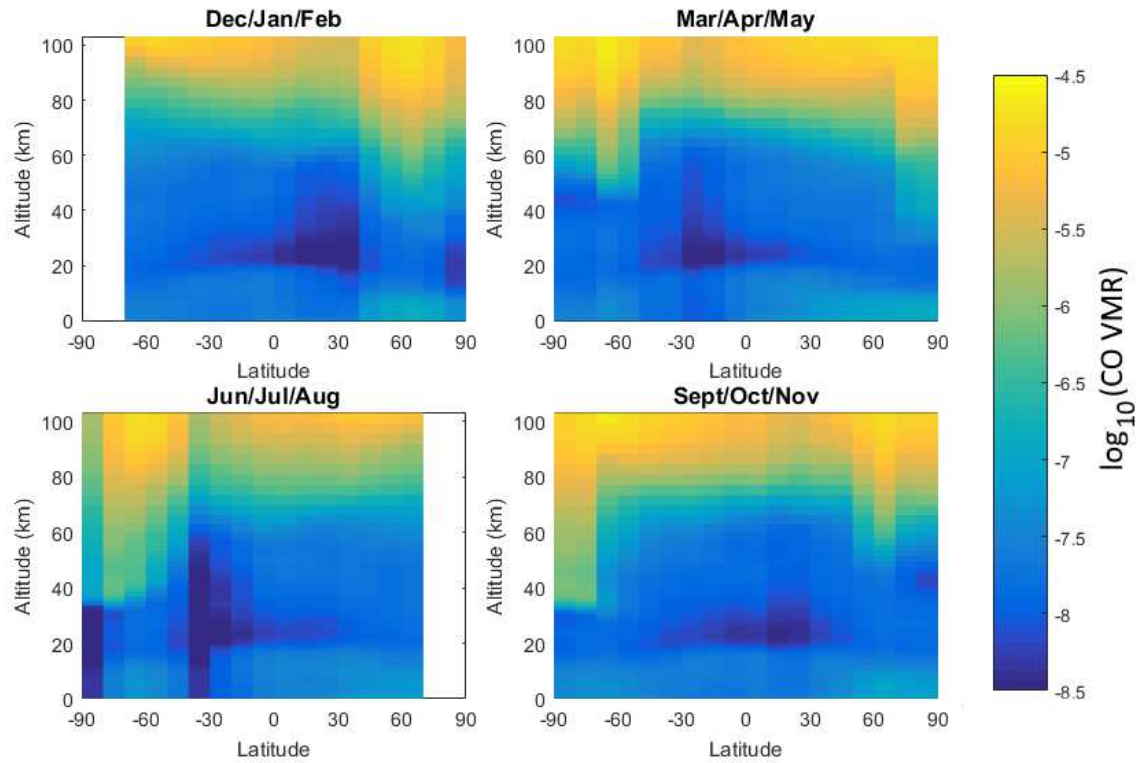


Figure 40: Total CO VMR by season from the ACE-sampled WACCM data set

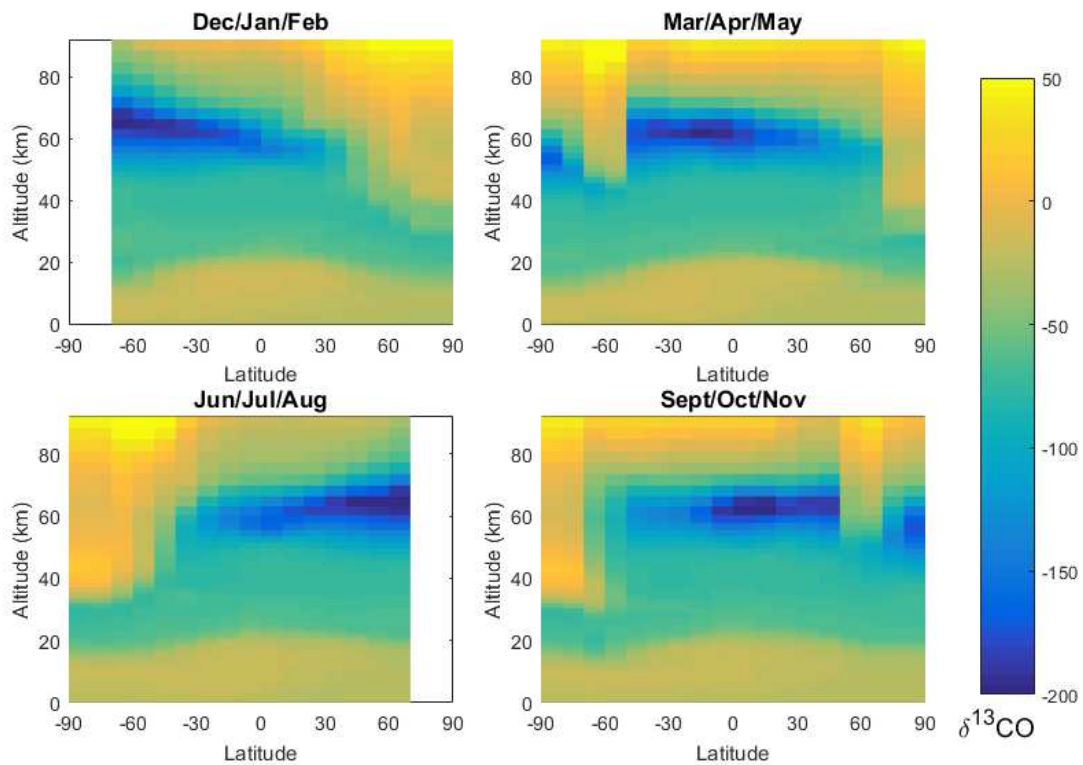


Figure 41:  $\delta^{13}\text{C}$  by season from the ACE-sampled WACCM data set

The same sampling scheme was applied to the  $\delta^{13}\text{CO}$  data (Figure 41). However, this does not result in a much closer match with the ACE data set. While this does reproduce the sharp latitudinal gradient in  $\delta^{13}\text{CO}$  in the high latitude mesosphere, the areas of high enrichment in the troposphere and stratosphere are still missing.

The band of high enrichment at 40 km appears to be a result of systematic errors in the CO VMR retrievals around that altitude. Formaldehyde peaks at around 40 km (Ricaud et al., 2007; Vigouroux et al., 2009) and the oxidation of formaldehyde to CO favors the production  $^{13}\text{CO}$  over  $^{12}\text{CO}$ , an uncommon inverse KIE (Feilberg et al., 2004). However, the fractionation in this band is very high relative to the fractionation of the  $\text{CH}_2\text{O} + \text{OH}$  reaction and is suspiciously flat over all altitudes, meaning the band is likely an artifact. The bands at 12 km are also suspected to be retrieval artifacts as they are similarly flat and appear in the upper troposphere where rapid mixing should produce a homogenous isotopic signature. This also may be due to poor data at the low end of the altitude range of  $^{13}\text{CO}$  measurements. While these artifact bands may be a problem, they highlight the sensitivity of the retrieval process to systematic errors, and their detection can leave to improvements in the profiles of  $^{12}\text{CO}$  and  $^{13}\text{CO}$ .

The area of high fractionation between 20 km and 30 km is another noticeable feature present in ACE but missing in WACCM. Unlike the other two bands, this area does not show any features characteristic of a retrieval error such as a narrow flat shape or a rapid spike in fractionation. Rather, this area may have a real fractionation effect that is not properly modeled by WACCM. One possibility is the oxidation of NMHC entering the stratosphere in the tropics; this run of WACCM only contains reactions involving methane. Indeed, CO produced from the oxidation of NMHCs is more highly enriched in  $^{13}\text{CO}$  compared to methane oxidation (Figure 35). Concentrations of CO are also very low in this region (Figure 36), meaning the oxidation of CO, which favors  $^{12}\text{CO}$  consumption over  $^{13}\text{CO}$ , is important.

Figure 42 shows the residual in  $\delta^{13}\text{CO}$  between the ACE and WACCM datasets; positive areas denote where ACE is higher. In the troposphere and stratosphere outside of the enrichment areas seen only in ACE, the residuals are between -50‰ and +50‰, showing good agreement between the two datasets in this region. In the mesosphere, WACCM predicts a lower amount of fractionation compared to ACE

(recall that both datasets are negative in the mesosphere except over the winter pole). This is likely due a lack of comprehensive treatment of  $\text{CO}_2$  photolysis. Cross sections for both isotopologues are only available to 150 nm, to fractionation from photolysis below 150 nm is not modeled. Also, temperature and pressure dependence is not modeled at the relevant wavelengths for this reaction. Still, this is believed to be the first attempt to model  $^{13}\text{CO}$  in the atmosphere that is at least semi-quantitative.

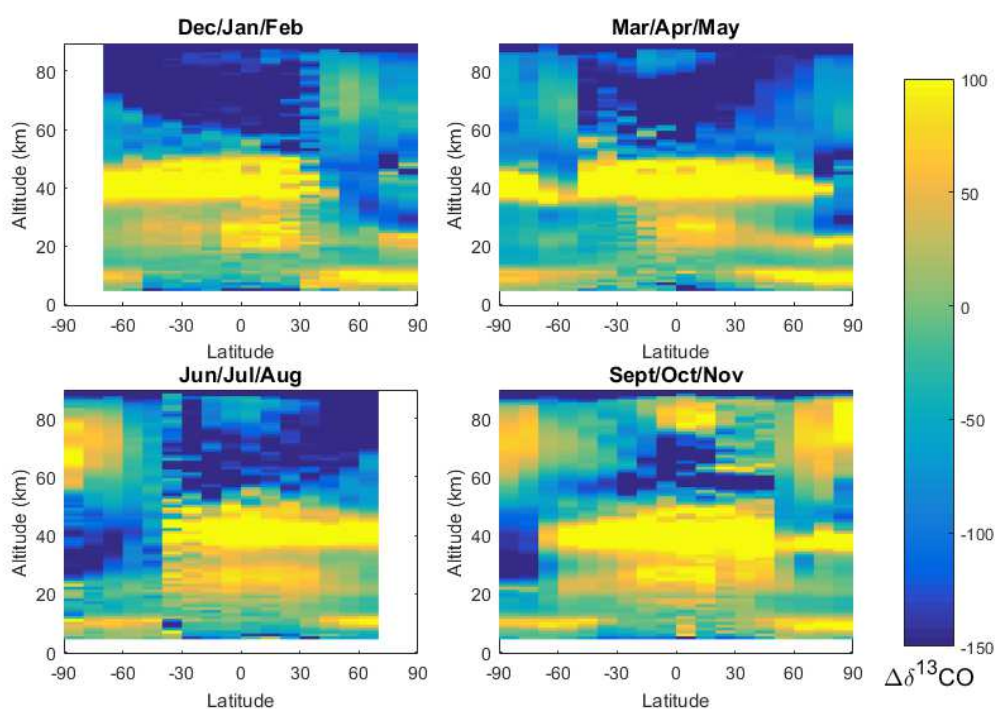


Figure 42: Residual in  $\delta^{13}\text{CO}$  between ACE and WACCM. In areas with positive values,  $\delta^{13}\text{CO}$  from ACE is higher than that from WACCM.

No other measured atmospheric profiles of  $^{13}\text{CO}$  are known to exist for comparison to ACE. However, several surface measurements of  $^{13}\text{CO}$  are available, though the high optical thickness and spectral congestion in the troposphere results in ACE measurements being less accurate near the surface. As the troposphere is well-mixed, ACE measurements in the upper troposphere can be compared with other surface measurements. In the subtropics, the averaged  $\delta^{13}\text{CO}$  value from ACE

in the troposphere is  $-32\text{‰}$ . Measurements from Mount Sonnblick, Austria ( $47^{\circ}\text{N}$ ) have  $\delta^{13}\text{CO}$  values ranging between  $-25\text{‰}$  and  $-30\text{‰}$  (Gros et al., 2001). Over Happo, Japan ( $37^{\circ}\text{N}$ ),  $\delta^{13}\text{CO}$  has been measured at between  $-24\text{‰}$  and  $-29\text{‰}$  (Kato et al., 2000). Finally, a transect across the Trans-Siberian Railroad gave values ranging between  $-26\text{‰}$  and  $-29.5\text{‰}$  (Tarasova et al., 2007).

## 6.4 Conclusions

This chapter presents the first set of global atmospheric data for  $^{13}\text{CO}$  measured from orbit in the infrared. This data can be used to further constrain sources and sinks in the CO budget. Both ACE and WACCM show that high enrichment in  $^{13}\text{CO}$  is present in the upper mesosphere and lower thermosphere and sinks over the poles in the wintertime. While this work is a good first look at global  $^{13}\text{CO}$  distributions, further improvements can be made to both datasets: the addition of more reactions to be modeled by WACCM and reduction of artifacts in the troposphere and stratosphere in ACE.

## CO<sub>2</sub> MASS-INDEPENDENT FRACTIONATION IN THE UPPER ATMOSPHERE

### 7.1 Introduction

CO<sub>2</sub> is the most well-known greenhouse gas and is the primary driver of climate change. Prior to the Industrial Revolution, tropospheric CO<sub>2</sub> concentrations were about 280 ppm; they have steadily risen since. Regular measurements from Mauna Loa Observatory, the source of the famous Keeling Curve (Figure 43) have shown CO<sub>2</sub> concentrations increasing from 315 ppm in 1958 to 405 ppm in 2017 (Keeling et al., 2001). In the troposphere, CO<sub>2</sub> is chemically inert, giving it a long lifetime. However, it exchanges between several surface reservoirs on Earth's surface on an overall timescale of years. These short-term reservoirs include biological activity (photosynthesis and respiration) and gas exchange with seawater. On longer timescales, CO<sub>2</sub> is stored in organic matter and carbonate minerals within the Earth's crust. Anthropogenic fossil fuel use removes carbon from these geologic reservoirs, unbalancing the carbon budget and leading to increased CO<sub>2</sub> concentrations (Ciais et al., 2013).

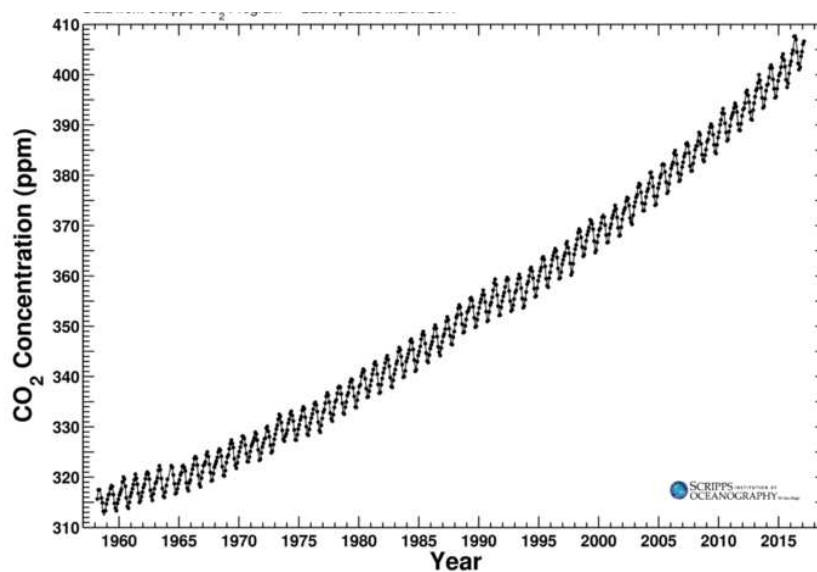


Figure 43: The Keeling Curve: CO<sub>2</sub> concentration from Mauna Loa Observatory, Hawaii

This increased CO<sub>2</sub> propagates into the higher layers of the atmosphere. CO<sub>2</sub> concentrations in the stratosphere are increasing, but lag behind tropospheric values by 5-6 years (Bischof et al., 1985; Foucher et al., 2011). CO<sub>2</sub> has an infrared emission band at 15 μm that radiatively cools the stratosphere. Stratospheric temperature measurements are often made using this band. Besides a small vertical gradient, CO<sub>2</sub> concentrations are constant throughout the stratosphere as it has no major sources or sinks here.

As mentioned in Section 6.1, CO cycles with CO<sub>2</sub> as the primary carbon species in the mesosphere and thermosphere. Radiative cooling from the 15 μm band is also important here, and the air is sufficiently thin to allow this radiation to escape into space. CO<sub>2</sub> is constant to about 60 km, then rapidly drops off in the mesosphere and lower thermosphere. Here, UV radiation is sufficiently strong to destroy CO<sub>2</sub>. In addition, air is thin enough for gases to separate by mass; the heavy CO<sub>2</sub> molecule diffuses upward more slowly in this region, further contributing to its decreased abundance in the thermosphere (López-Puertas et al., 2000). CO<sub>2</sub> shows seasonal variation in this region due to atmospheric dynamics and photolysis (Beagley et al., 2010). Thermospheric CO<sub>x</sub> (CO and CO<sub>2</sub>) is increasing at a rate of 2.35 ppm/yr, mostly driven by increases in CO<sub>2</sub> (Emmert et al., 2012).

This increasing abundance of CO<sub>2</sub> has an impact on the vertical structure of the upper atmosphere. As CO<sub>2</sub> builds up, the strength of its radiative cooling increases, thermal contraction of the atmosphere can occur (Roble and Dickinson, 1989). Laštovička et al (2008) demonstrated that temperature trends in the mesosphere and thermosphere are consistent with a contraction of these layers primarily driven by in-situ radiative cooling. This demonstrates that anthropogenic emissions of CO<sub>2</sub> can have an effect on the entire atmosphere, not just near the surface.

### *7.1.1 Mass independent fractionation of CO<sub>2</sub>*

Isotopologues of CO<sub>2</sub> can contain three oxygen isotopes: <sup>16</sup>O, <sup>17</sup>O, <sup>18</sup>O. The presence of a third isotope gives extra information beyond δ<sup>17</sup>O and δ<sup>18</sup>O when analyzing isotopic concentrations. Kinetic isotope effects arise from the difference in masses of isotopes, and the strength of the effect is proportional to the mass



difference (Section 2.3.1). As  $^{18}\text{O}$  is two mass units heavier than  $^{16}\text{O}$ , but  $^{17}\text{O}$  is only one mass unit heavier, KIEs for  $^{18}\text{O}$  should be about twice as large as for  $^{17}\text{O}$ . In turn, fractionation of  $^{18}\text{O}$  should be twice as strong. The commonly-used value for the ratio  $\Delta\delta^{17}\text{O}/\Delta\delta^{18}\text{O}$  is 0.52 and can be calculated from Equation 1 in Section 2.3.1. Deviations from this ratio are known as mass-independent fractionation (MIF).

In a strict sense, MIF cannot be determined from a single three-isotope measurement as the choice of the isotope ratio standard will affect the final delta values of the sample. Therefore, MIF must be verified by taking several measurements over a range of delta values, plotting (for example)  $\delta^{17}\text{O}$  vs  $\delta^{18}\text{O}$ , and measuring the triple isotope slope  $\Delta\delta^{17}\text{O}/\Delta\delta^{18}\text{O}$ . For a single measurement of  $\text{CO}_2$ , the  $^{17}\text{O}$  anomaly, denoted as  $\Delta^{17}\text{O}$ , is determined by:

$$\Delta^{17}\text{O} = \delta^{17}\text{O} - 0.52 \times \delta^{18}\text{O} \quad (46)$$

This chapter uses the triple isotope slope to analyze mass-independent fractionation.

Mass-independent fractionation of atmospheric gases was first measured in ozone. Thieme and Heidenreich (1983) discovered that ozone produced from electrical discharge of molecular oxygen was equally enriched in  $^{18}\text{O}$  and  $^{17}\text{O}$  rather than showing a 2:1 ratio. This fractionation was confirmed to occur in the stratosphere from two balloon flights by Mauersberger (1987), who measured the same equal enrichment in  $^{18}\text{O}\text{-O}_3$  and  $^{17}\text{O}\text{-O}_3$ . More recent measurements find the enrichment of ozone reaches as high as +130‰ in  $\delta^{18}\text{O}$  and +100‰ in  $\delta^{17}\text{O}$  vs.  $\text{O}_2$  in the stratosphere (Krankowsky et al., 2000, 2007; Mauersberger et al., 2001). The increase in fractionation at higher altitudes (Haverd et al., 2005), combined with laboratory studies of ozone photolysis (Liang et al., 2006; Miller et al., 2005) indicate that both the production and destruction of ozone contribute to its observed MIF.

$\text{CO}_2$  also displays interesting isotopic behavior in the stratosphere. One of the first balloon measurements by Gamo et al. (1989) showed that the lower stratosphere was 2‰ more enriched in  $^{18}\text{O}$  than the troposphere and  $\delta^{18}\text{O}$  increased with height up to 25 km. Yung et al. (1991) proposed that this increase was due to an isotopic exchange with ozone via  $\text{O}(^1\text{D})$  and a  $\text{CO}_3$  intermediate:



Thiemens et al. (1991) extended balloon measurements to  ${}^{17}OCO$ . They noted tropospheric values of  $\delta^{18}O = +40.4\text{‰}$  and  $\delta^{17}O = +20.9\text{‰}$  vs. VSMOW, consistent with mass-dependent fractionation. Stratospheric values for both isotopologues were on average 11‰ higher, demonstrating mass-independent fractionation. Further studies (Chakraborty and Bhattacharya, 2003; Shaheen et al., 2007; Yung et al., 1997) verified that the culprit of the isotopic behavior of stratospheric  $CO_2$  is exchange with ozone.

Recent measurements have shown that MIF of stratospheric  $CO_2$  is even stronger than that of ozone, especially in the polar vortex. Figure 44 shows a three isotope plot of several stratospheric measurements of  $CO_2$  (Wiegel et al., 2013). Note that these data are presented with the logarithmic notation  $\ln^{18}O = \ln(\delta^{18}O + 1)$  which removes a slight curvature that has no physical significance from the plot (Barkan and Luz, 2005). The slopes of  $\Delta \ln^{17}O / \Delta \ln^{18}O$  measured by Wiegel et al. (marked by triangles) range from 1.95 in the mid-latitudes to 2.22 in the polar vortex. Lämmerzahl (2002) determined a slope of 1.71 from measurements over France and Sweden. Alexander et al. (2001) made several measurements in and around the polar vortex with a slope of 2.1. One set of measurements made by Thiemens et al. (1995) ranges from 30 km to 60 km with a slope of 1.16, demonstrating that MIF of  $CO_2$  continues into the lower mesosphere.

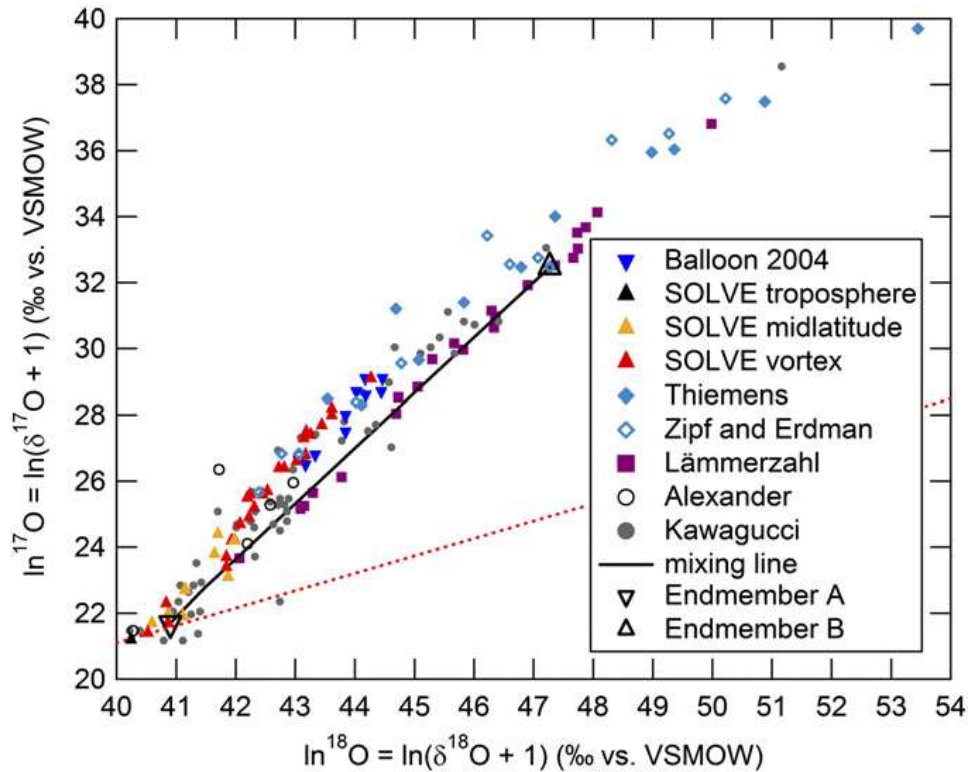


Figure 44: Three isotope plot of stratospheric CO<sub>2</sub> from several sources. The red line denotes mass-dependent fractionation,  $m = 0.52$ , while the black line has a slope of 1.7. From Wiegel et al. (2013)

So far measurements of CO<sub>2</sub> isotopologues have only been performed via balloon, rocket, or aircraft, limiting the spatial coverage. With the exception of measurements by Thiemens et al. (1995), measurements have also been limited to the stratosphere. This work presents measurements of  $\delta^{18}\text{O}$  and  $\delta^{17}\text{O}$  of CO<sub>2</sub> from ACE-FTS, expanding the range of CO<sub>2</sub> isotopologue measurements into the entire mesosphere and over almost the entire globe. ACE-FTS measures <sup>18</sup>OCO from the troposphere to 105 km and <sup>17</sup>OCO from 50 km to 100 km. This also allows for determination of mass-independent fractionation of CO<sub>2</sub> in the mesosphere. Data of OO<sup>18</sup>O, available up to 50 km, is also presented and briefly discussed in comparison with <sup>18</sup>OCO in the stratosphere.

A WACCM model run was also performed for comparison to ACE. However, its results had poor agreement with existing stratospheric CO<sub>2</sub> isotopologue measurements and therefore is not used here.

## 7.2 Methods

Retrievals from ACE-FTS of CO<sub>2</sub>, and its isotopologues use version 3.5 of the ACE-FTS software (Boone et al., 2013). A total of 28,236 occultations were analyzed in this work. Note that CO<sub>2</sub> is initially retrieved simultaneously with pressure and temperature. Between 12 km and 65 km (above 60°) or 75 km (below 60°), CO<sub>2</sub> is fixed using the equation

$$\text{CO}_2 \text{ VMR (ppm)} = 326.909 + 1.50155(t - t_0), t_0 = \text{January 1, 1977} \quad (50)$$

where  $t$  is in years. In the troposphere, CO<sub>2</sub> VMR is increased by 5.5 ppm. Above this altitude, CO<sub>2</sub> is fitted to an empirical formula:

$$\text{CO}_2 \text{ VMR}(z) = \frac{\text{VMR}_{\text{strat}} + a(z - z_0) + b(z - z_0)^2 + c(z - z_0)^3}{1 + d(z - z_0) + e(z - z_0)^2} \quad (51)$$

where  $z_0$  is the highest altitude that CO<sub>2</sub> is fixed.

In the final data product, CO<sub>2</sub> VMR is retrieved in the same manner as other gases. In theory, this should give back the initial fixed profile from P/T retrievals. However, the limitations of the retrieval method mean that there will be some differences between the fixed CO<sub>2</sub> values and the retrieved CO<sub>2</sub> profile. Replacing the retrieved CO<sub>2</sub> VMR with the fixed values in the middle atmosphere did not have a noticeable effect on the final calculated values of  $\delta^{18}\text{O}$  and  $\delta^{17}\text{O}$ , so the retrieved profiles are used. Either way, the lack of spatial and seasonal variation in the fixed CO<sub>2</sub> VMR introduces a small amount of systematic error in  $\delta^{18}\text{O}$  and  $\delta^{17}\text{O}$ . Version 4.0 of ACE-FTS retrievals will use a more realistic input CO<sub>2</sub> value for a given location and time.

The microwindows used for <sup>12</sup>CO<sub>2</sub> retrievals include lines from the  $\nu_1$ -  $\nu_3$ ,  $3\nu_2$ ,  $\nu_1 + \nu_2$ , and  $\nu_3$  vibrational bands. <sup>18</sup>OCO retrievals use lines from the  $\nu_1$ ,  $\nu_3$ , and  $4\nu_2$  bands, while <sup>17</sup>OCO use only the  $\nu_3$  band. A summary of the lines used is given in Table 8, and a full microwindow list is given in Tables 18-20 in the Appendix.

Table 8: Summary of CO<sub>2</sub> microwindows used

Species	Number of microwindows	Altitude range (km)	Microwindow ranges (cm <sup>-1</sup> )
CO <sub>2</sub>	109	5-125	927.0 - 947.7
			1899.2 - 1975.1
			2044.5 - 2072.2
			2289.2 - 2444.27
<sup>18</sup> OCO	59	5-105	1371.8 - 1385.9
			2276.7 - 2360.6
			2604.5 - 2636.6
<sup>17</sup> OCO	23	50-100	2329.6 - 2385.0

All of the <sup>12</sup>CO<sub>2</sub> microwindows were selected to be free of interfering species. However, the two heavy isotopologues do have interferers. For <sup>17</sup>OCO, the interfering species are CO<sub>2</sub>, <sup>13</sup>CO<sub>2</sub>, <sup>17</sup>OCO, <sup>18</sup>O<sup>13</sup>CO, <sup>17</sup>O<sup>13</sup>CO, <sup>18</sup>OC<sup>18</sup>O, <sup>17</sup>OC<sup>18</sup>O, CH<sub>4</sub>, <sup>13</sup>CH<sub>4</sub>, N<sub>2</sub>O, H<sub>2</sub>O, HDO, H<sup>17</sup>OH, and O<sub>3</sub>. For <sup>17</sup>OCO, the interfering species are CO<sub>2</sub> and <sup>18</sup>OCO. As with other molecules, interfering species are retrieved simultaneously with the target species, but the data are discarded.

### 7.3 Results and Discussion

#### 7.3.1 ACE δ<sup>18</sup>O and δ<sup>17</sup>O

Figure 45 shows the ACE full mission average and standard deviation for δ<sup>18</sup>O for by season. The troposphere and lower stratosphere has a nearly constant fractionation of around +40‰. The upper stratosphere is dominated by two bands of low enrichment at 30 km and 45 km. Inside these bands, δ<sup>18</sup>O reaches as low as -15‰ at 30 km and -40‰ at 45 km. The standard deviation is higher in the 40km band, indicating noisy data around this altitude. In between the two bands is a narrow band of high enrichment with a maximum of +100‰ around 38 km at the Equator. A small amount of seasonal variation is present in the stratosphere, where the two low-enrichment bands are more depleted in OC<sup>18</sup>O over the summer pole.

In the lower mesosphere, enrichment in OC<sup>18</sup>O increases with altitude and toward the Equator. Values range from +50‰ at 50 km to +100‰ at 70 km. This

area of high enrichment also shifts toward the winter pole. Enrichment drops slightly to a minimum at 80 km. At around 80 km in the spring, a pocket of low-enriched air forms at high latitudes and moves poleward. By the winter,  $\delta^{18}\text{O}$  values within this air mass reach  $-20\text{‰}$  over the South Pole and  $-30\text{‰}$  over the North Pole. Above 85 km,  $\delta^{18}\text{O}$  rapidly increases to over  $+200\text{‰}$  at some locations. However, the standard deviation also spikes at the altitudes to over  $200\text{‰}$ , suggesting that the data may be unreliable. The color scale for standard deviation on Figure 45 to highlight the variance at lower altitudes rather than these very high values.

The mission average and standard deviation for  $\delta^{17}\text{O}$  over the same timeframe is given in Figure 46. Spatial trends in mesospheric  $\delta^{17}\text{O}$  appear similar to that of  $\delta^{18}\text{O}$ . Values of  $\delta^{17}\text{O}$  range from  $+100\text{‰}$  at 55 km to  $+130\text{-}190\text{‰}$  at 65 km, then decrease to  $+90\text{-}140\text{‰}$  at 80 km. The mass of low-enrichment air approaches  $+75\text{‰}$  over the South Pole and  $+50\text{‰}$  over the North Pole. In the lower thermosphere  $\delta^{17}\text{O}$  again spikes to very high levels, up to  $+500\text{‰}$  at 100 km, but the large standard deviation (up to  $350\text{‰}$ ) implies low-quality data.

Figure 47 directly compares vertical profiles of both isotopologues in the  $60^\circ\text{N}$  -  $70^\circ\text{N}$  latitude bin. The strong depletion in both isotopologues during the spring and summer near the mesopause is visible. The area of enrichment in the middle mesosphere is also present in both isotopologues. However, the altitude of maximum fractionation is different between the two;  $\delta^{18}\text{O}$  peaks at 70 km while  $\delta^{17}\text{O}$  peaks at only 65 km.

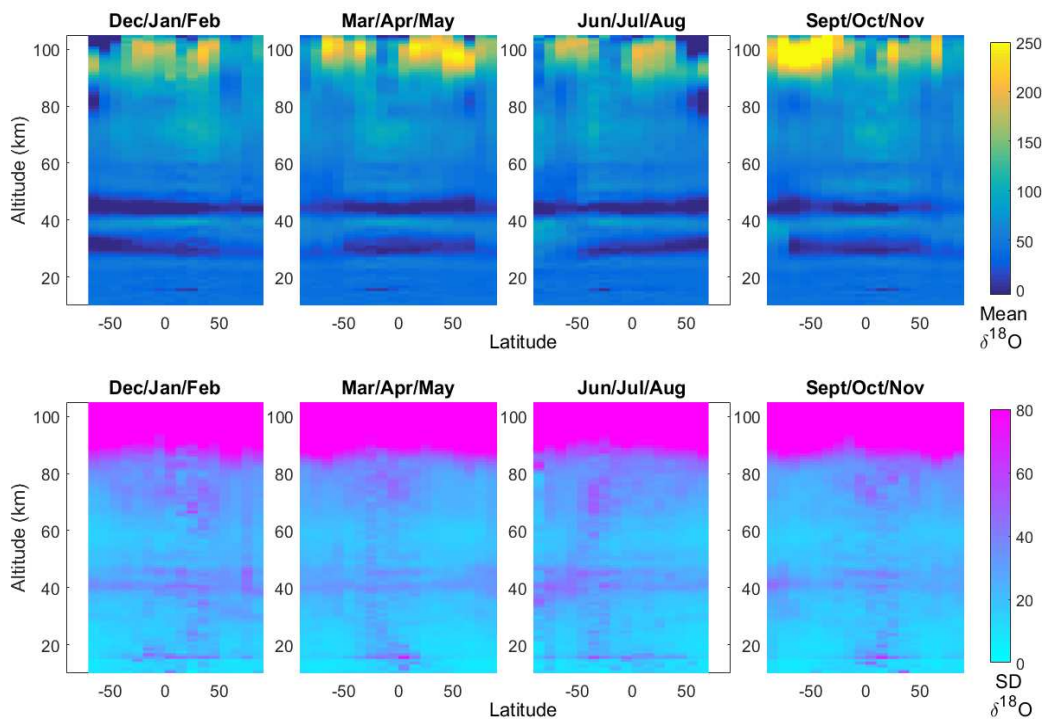


Figure 45: ACE CO<sub>2</sub> δ<sup>18</sup>O mission average (top) and standard deviation (bottom) by season.

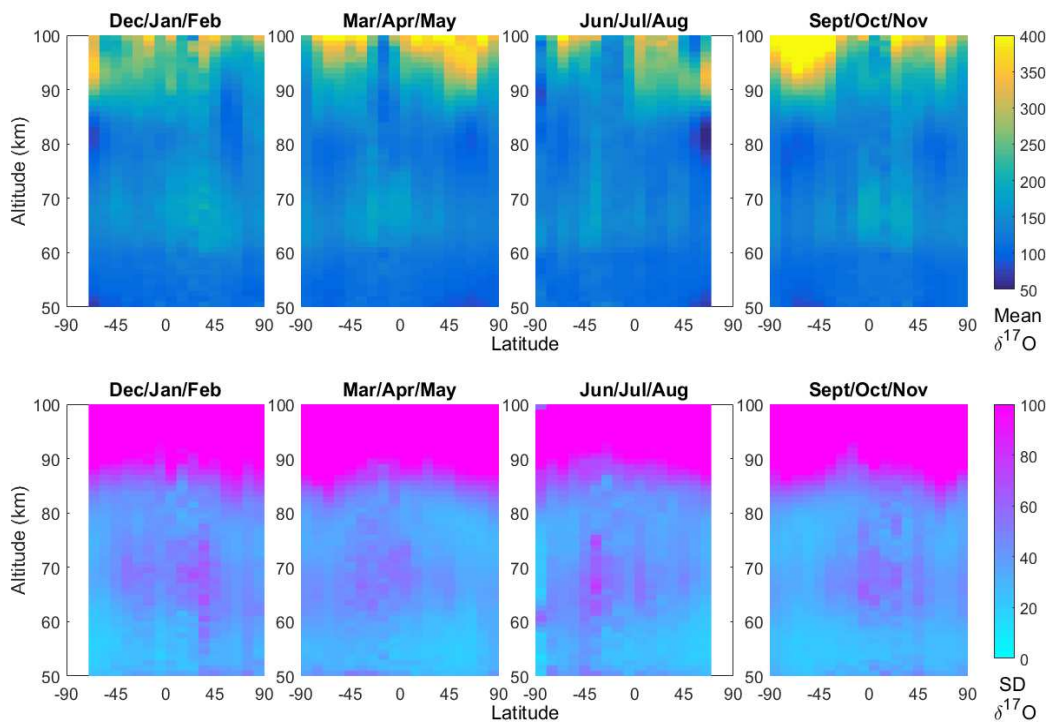


Figure 46: ACE CO<sub>2</sub> δ<sup>17</sup>O mission average (top) and standard deviation (bottom) by season.

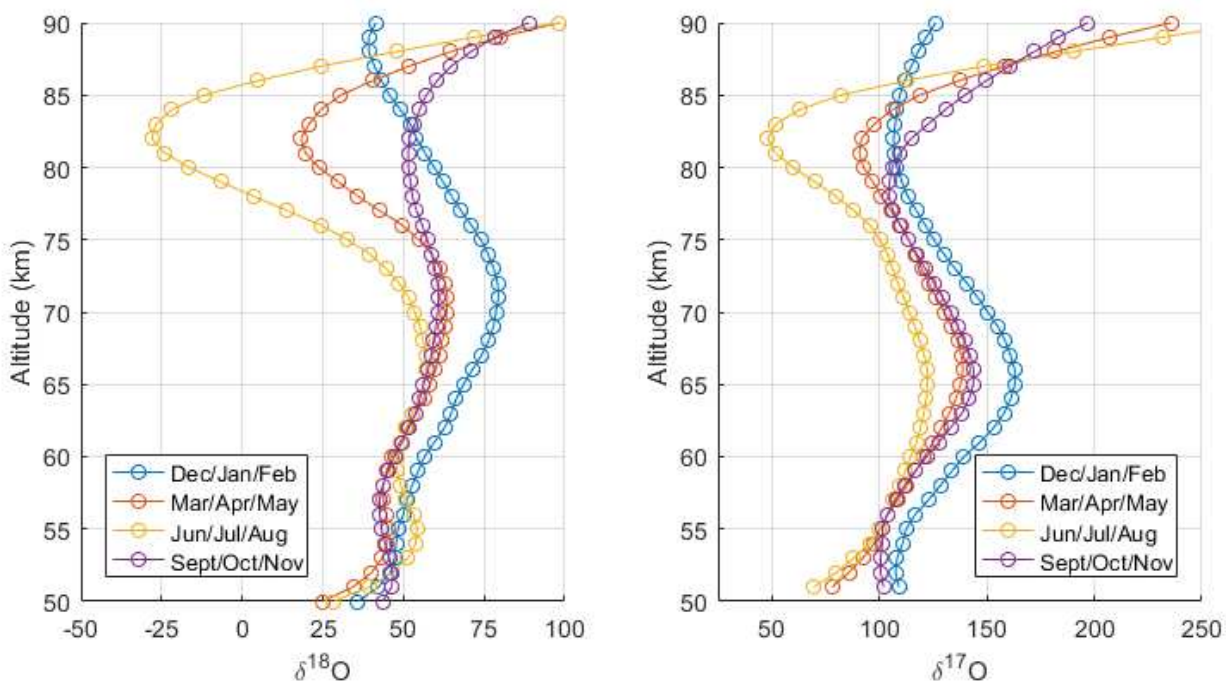


Figure 47: Altitude profiles of CO<sub>2</sub> isotopic abundance in the 60°N - 70°N latitude bin

### 7.3.2 Triple isotope plots

The triple isotope slope  $\Delta\delta^{17}\text{O}/\Delta\delta^{18}\text{O}$  was investigated by binning the full ACE data set by two methods: 30° latitude (Figure 48) and season (Figure 49). A summary of the  $\Delta\delta^{17}\text{O}/\Delta\delta^{18}\text{O}$  values with the error of the slope from a least-squares fit is given in Table 9. The triple isotope slope shows variation by both latitude and season. At low- and mid-latitudes, the slope has a small range 1.64 to 1.69; values are slightly higher in the Southern Hemisphere. Near the poles, the slope is much lower, reaching  $1.608 \pm 0.003$  over the South Pole and  $1.482 \pm 0.002$  over the North Pole.

Seasonally, the lowest values are seen in the summer in both hemispheres, reaching  $1.201 \pm 0.003$  in the north and  $1.361 \pm 0.004$  in the south. This correlates



with the pocket of low enrichment seen over the summer poles in Figure 45 and Figure 46. In most of the remaining seasons, the slope ranges from 1.63 to 1.70, closely matching the low- and mid-latitude slopes. The Northern Hemisphere spring is somewhat anomalous with a slope of  $1.562 \pm 0.004$ . This may indicate a trend of the slope decreasing smoothly over several months to a minimum in the summer. However, this is not seen in the Southern Hemisphere where the slope sharply drops in just the summer.

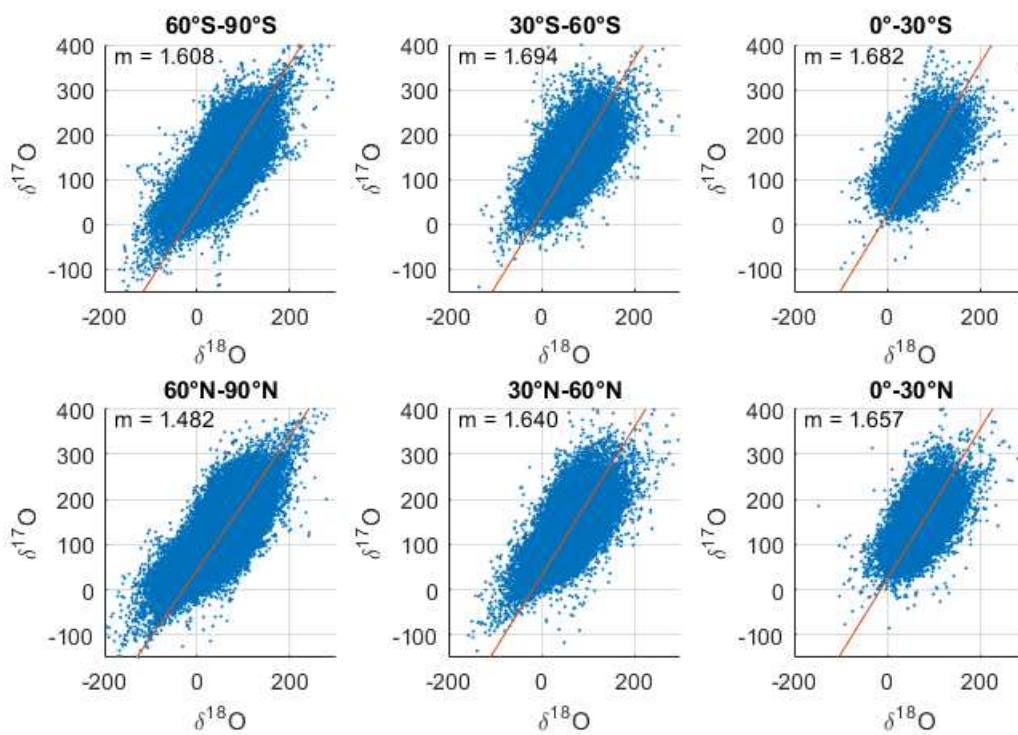


Figure 48: Triple isotope plots of mesospheric CO<sub>2</sub> by 30° latitude bins.

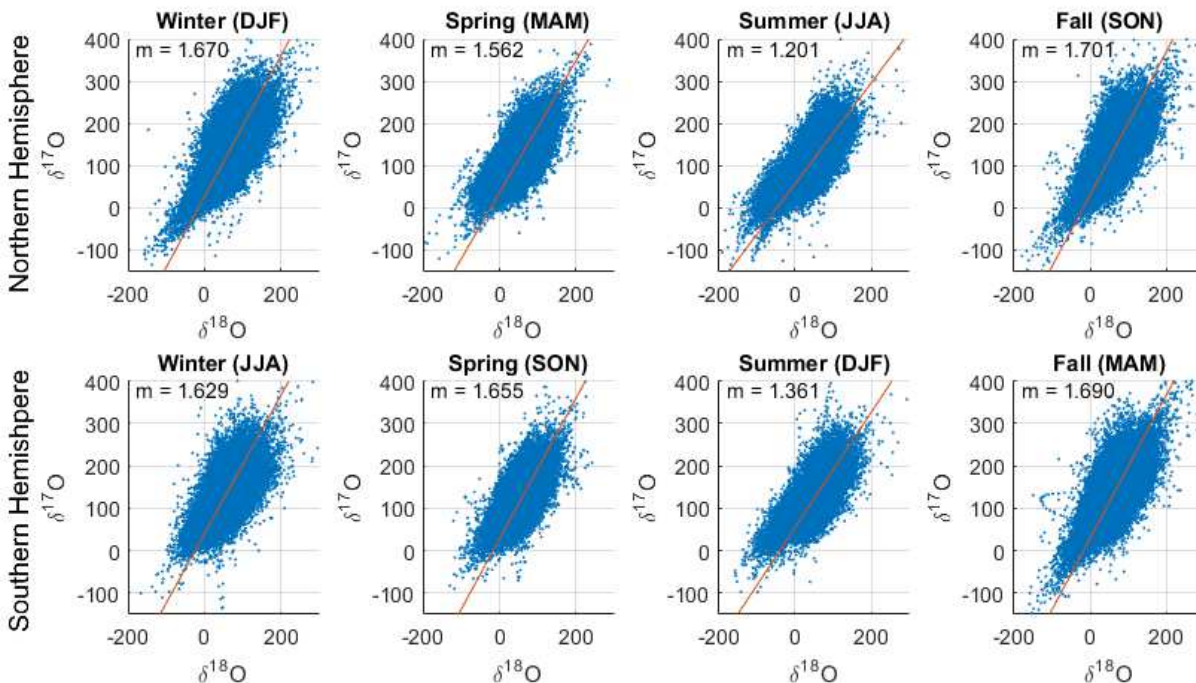


Figure 49: Triple isotope plots of mesospheric CO<sub>2</sub> by season and hemisphere.

Table 9: Summary of triple isotope slopes from the ACE CO<sub>2</sub> dataset. The number in parentheses denotes the error of the slopes from a least-squares fit in the last digit.

Bin	Slope	Bin	Slope
Full mission average	1.564(1)	By Season/Hemisphere	
		NH Winter	1.670(4)
By 30° Latitude		NH Spring	1.562(4)
NH Equatorial	1.657(7)	NH Summer	1.201(3)
NH Mid-latitude	1.640(4)	NH Fall	1.701(4)
NH Polar	1.482(2)	SH Winter	1.629(5)
SH Equatorial	1.682(7)	SH Spring	1.655(4)
SH Mid-latitude	1.694(4)	SH Summer	1.361(4)
SH Polar	1.608(3)	SH Fall	1.690(4)

Many of the triple isotope plots have a “tail” at low values of  $\delta^{18}\text{O}$  and  $\delta^{17}\text{O}$ . These data points correspond to the summer pocket of low enrichment seen between at 80 km. The points lie to the left of the best-fit slope of all data;

connecting them to the points at higher enrichment would result in a lower slope than what is seen overall, denoting a smaller triple isotope anomaly.

The overall mesospheric triple isotope slope of  $1.564 \pm 0.001$  measured by ACE is lower than previous stratospheric measurements which range from 1.7 to 2.2 but higher than the stratospheric/lower mesospheric slope of 1.16 measured by Thiemens et al. (1995). Above the stratosphere, ozone concentrations decrease up to 75 km, then increase with a maximum at 95 km. Even at the minimum at 75 km, concentrations are only about an order of magnitude lower than those in the stratosphere (Kasai et al., 2013). Therefore, isotopic exchange between ozone and  $\text{CO}_2$  can still happen in the mesosphere and drive the large mass-independent fractionation seen here. However, another process involving  $\text{CO}_2$  with a different mass dependence is likely occurring that lowers the observed slope in the mesosphere.

Cycling between CO and  $\text{CO}_2$  is one possible culprit.  $\text{CO}_2$  photolysis is a mass-dependent process (Schmidt et al., 2013); the  $\text{CO} + \text{OH}$  reaction is mass-independent, though it has a very weak kinetic isotope effect:  $k_{18}/k_{16} = 0.985$ ,  $k_{17}/k_{16} = 1.000$  (Feilberg et al., 2005a). The two reactions combined would enrich  $\text{CO}_2$  in  $^{17}\text{O}$  and  $^{18}\text{O}$  in a near-mass-dependent manner, reducing the observed triple isotope slope in the mesosphere.

However, this would not explain the low enrichment seen in the upper mesosphere. Isotopic exchange with  $\text{O}_2$  rather than  $\text{O}_3$  could occur since the low-wavelength UV light needed to photolyze  $\text{O}_2$  is more readily available at these high altitudes. Though  $\text{O}_2$  photolysis is strongly mass-independent,  $\text{O}_2$  is less enriched in heavy isotopes than ozone:  $\delta^{17}\text{O} = +12.08\text{‰}$  and  $\delta^{18}\text{O} = +23.88\text{‰}$  (Barkan and Luz, 2005). This exchange would produce  $\text{CO}_2$  with low enrichment overall but a stronger fractionation toward  $\delta^{17}\text{O}$ .

### *7.3.3 Profile comparison with other data sets*

ACE  $\delta^{18}\text{O}$  for  $\text{CO}_2$  was compared to several other stratospheric data sets, including aircraft measurements from the SOLVE campaign (Wiegel et al., 2013), rocket measurements (Thiemens et al., 1995), and balloon measurements

(Alexander et al., 2001; Kawaguchi et al., 2008; Lämmerzahl, 2002; Wiegel et al., 2013). These measurements are shown in Figure 50. From the upper troposphere to 25 km, ACE has very good agreement with previous measurements. Most data points lie between +40‰ and +50‰ over this range with a small increase at higher altitudes. Between 25 and 50 km, the three bands of high and low enrichment appear in ACE but do not in any other data set. This region has been problematic in CH<sub>4</sub> (Chapter 4) and CO (Chapter 5) isotopic measurements and the CO<sub>2</sub> data here is likely showing similar unphysical spikes in enrichment. Above 50 km, data is very sparse, consisting of just a few rocket measurements from Thiemens et al. ACE reports values slightly lower than the rocket measurements +45‰ for ACE versus +52‰ via rocket at 54 km), but these data are still well within the error range of ACE. Based on the agreement below 25 km and above 50 km, it is believed that ACE measurements in the mesosphere up to 85 km are accurate.

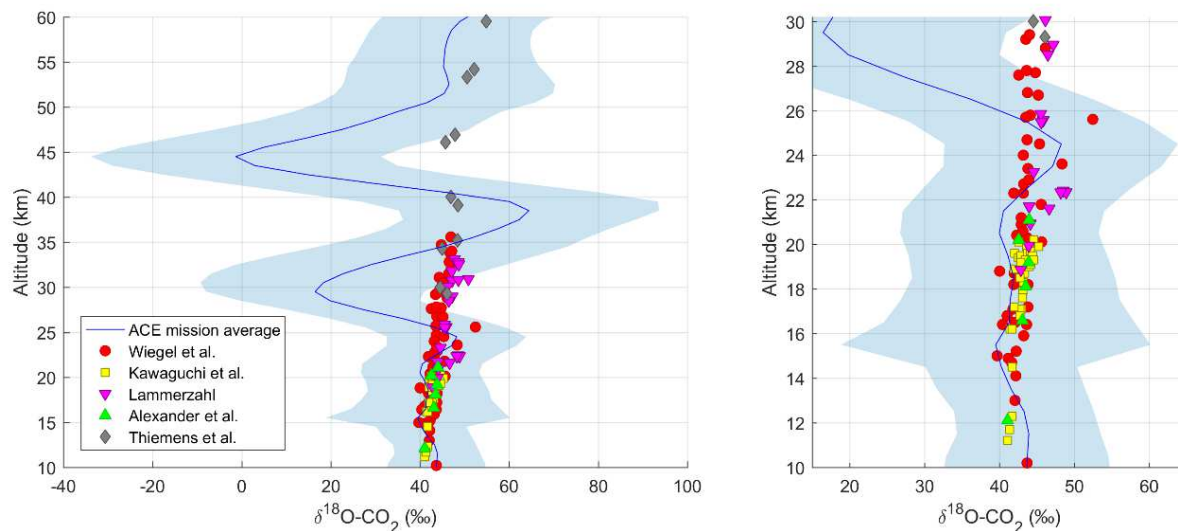


Figure 50: ACE  $\delta^{18}\text{O}$  compared to previous stratospheric measurements. The right figure focuses on measurements in the upper troposphere and lower stratosphere.

As  $\delta^{17}\text{O}$  from ACE begins at 50 km, these measurements can only be directly compared to the data from Thiemens et al. They report values of  $\delta^{17}\text{O}$  from +36 to +41 between 50 and 61 km. On the other hand, the ACE mission averages ranges from +100‰ to +120‰ in this region. Balloon measurements lower in the stratosphere from the previously mentioned studies lie between +20‰ and +40‰, and it is very unlikely that a spike in  $\delta^{17}\text{O}$  occurs between the stratosphere and mesosphere as none is present in  $\delta^{18}\text{O}$ . Therefore, ACE appears to overestimate mesospheric  $\delta^{17}\text{O}$  by about 60‰. If this bias is constant over the range of  $\delta^{17}\text{O}$  values, this would have no effect on the triple isotope slope in the mesosphere. However, if the bias is larger at higher enrichment (in other words, it is multiplicative), the “corrected” values of  $\delta^{17}\text{O}$  would reduce the triple isotope slope. ACE already reports slopes in this region lower than those in the stratosphere. However, isotope chemistry is not well understood in the mesosphere, so it is not known whether the triple isotope slope is expected to be lower than in the stratosphere.

#### **7.4 Conclusions**

This chapter presents the first global measurements of  $\delta^{18}\text{O}$  for  $\text{CO}_2$  in the stratosphere and mesosphere as well as  $\delta^{17}\text{O}$  in the mesosphere. Both isotopologues show increasing enrichment with altitude in the lower mesosphere and a minimum between 80 and 85 km. However, the altitude of maximum enrichment differs between the two isotopologues. Values of  $\delta^{18}\text{O}$  are problematic between 25 and 45 km but otherwise agree with previous observations, while  $\delta^{17}\text{O}$  is about 60‰ higher where comparisons can be made with previous data. The mesospheric triple isotope slope calculated from ACE averages 1.56 with lower slopes seen over the poles in the summer. This slope is lower than those measured in the stratosphere; cycling between CO and  $\text{CO}_2$  or differences in isotopic exchange may be the cause of this lower slope.

## ISOTOPOLOGUES OF N<sub>2</sub>O IN THE STRATOSPHERE

### 8.1 Introduction

Nitrous oxide (N<sub>2</sub>O) is a unique atmospheric gas in that it has two influences on climate change. It is a major greenhouse gas, the third strongest behind CO<sub>2</sub> and CH<sub>4</sub>, and has a GWP of 265 over 100 years (Myhre et al., 2013). In addition, it is an important ozone-depleting substance.

N<sub>2</sub>O is one of several nitrogen species produced from biological nitrogen fixation. In particular, N<sub>2</sub>O is one product of denitrification, the biological reduction of nitrate (NO<sub>3</sub><sup>-</sup>). Human activity since the Industrial Revolution has upset the balance of biological nitrogen fixation, leading to increased concentrations of N<sub>2</sub>O. Increased agricultural activity is the main source of nitrogen species. Use of nitrogen-containing synthetic fertilizers and manure increases the rate of denitrification in the soils, leading to increased N<sub>2</sub>O emissions. Runoff and leaching also transports nitrogen compounds into waterways, leading to increased denitrification in aquatic environments. Overall, nitrogen produced as a result of anthropogenic activity at least twice as high as natural production (Ciais et al., 2013), though the estimates of N<sub>2</sub>O emissions have an uncertainty factor of at least 2 (Prather et al., 2009) This has caused tropospheric N<sub>2</sub>O concentrations to increase 20% since before the Industrial Era (MacFarling Meure et al., 2006) to a 2011 value of 324 ppb (Hartmann et al., 2013).

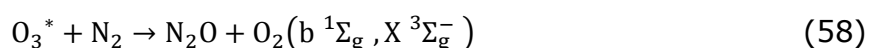
N<sub>2</sub>O is inert in the troposphere, leading to a lifetime of about 120 years (Prather et al., 2015). In the stratosphere, N<sub>2</sub>O is consumed by photolysis and reaction with singlet oxygen:



Photolysis comprises about 90% of the total atmospheric sink of N<sub>2</sub>O (Minschwaner et al., 1993); chemical loss via reactions 2 and 3 is 6% and 4%, respectively (Burkholder et al., 2015). N<sub>2</sub>O concentrations in the stratosphere strongly correlate with CH<sub>4</sub> as both have similar sinks in this region (Michelsen et al., 1998). As NO<sub>x</sub>

catalytically destroys ozone, N<sub>2</sub>O is an important ozone depleting substance. Calculations by Ravishankara et al. (2009) suggest that N<sub>2</sub>O is the dominant uncontrolled ozone-depleting substance in recent years due to the reduction of CFC emissions since the Montreal Protocol was enacted in 1989. N<sub>2</sub>O is not regulated under the Montreal Protocol, but is named in the Kyoto Protocol enacted in 2005.

Recently, N<sub>2</sub>O has also been shown to have an upper atmospheric source. Several reactions have been proposed as potential atmospheric sources of N<sub>2</sub>O (Prasad and Zipf, 2008; Semeniuk et al., 2008; Zipf and Prasad, 1982):



The presence of this atmospheric source was verified by observations from ACE-FTS that showed an excess of N<sub>2</sub>O above the North Pole at 50-60 km during winter 2004 and 2006 (Semeniuk et al., 2008). An associated model run demonstrated that energetic particle precipitation produces N<sub>2</sub>O in the mesosphere which is then carried downward during a sudden stratospheric warming event. More recent retrievals from ACE show increasing N<sub>2</sub>O with altitude to the instrumental limit of 95 km (Sheese et al., 2016). Enhanced stratospheric N<sub>2</sub>O has also been observed in 2003 over the North Pole with MIPAS (Funke et al., 2008).

N<sub>2</sub>O has multiple isotopic combinations such as NN<sup>18</sup>O, NN<sup>17</sup>O, <sup>15</sup>NNO, and N<sup>15</sup>NO from which a large amount of information can be derived. As with CO<sub>2</sub>, N<sub>2</sub>O can contain one of three oxygen isotopes, meaning mass independent fractionation can be studied. Heavy nitrogen can also be present on the center (<sup>15</sup>N<sup>α</sup>) or terminal (<sup>15</sup>N<sup>β</sup>) site of the molecule; the difference between these two is called the site preference (SP).

Snider et al. (2015) compiled N<sub>2</sub>O isotopic data from over 50 papers and concluded that there is a large overlap in isotopic signatures among various sources. The large variability in δ<sup>15</sup>N and δ<sup>18</sup>O from a given source can be attributed to the complexity of nitrogen fixing, nitrification, and denitrification which have multiple steps and pathways. Enrichment in <sup>15</sup>N and <sup>18</sup>O are correlated, and the amount of enrichment tends to increase from soils and groundwater to freshwater

to marine sources. Many surface aquatic measurements lie near the average tropospheric values of  $\delta^{15}\text{N} = 6.72\text{‰}$  and  $\delta^{18}\text{O} = 44.62\text{‰}$  vs. VSMOW (Kaiser, 2003) due to exchange with the atmosphere. On the other hand, groundwater sources do not exchange with the atmosphere and so have lower delta values. Long-term studies have shown that enrichment in heavy  $\text{N}_2\text{O}$  is decreasing over time due to the increased contribution of agricultural sources that are isotopically lighter (Bernard et al., 2006; Toyoda et al., 2013)

SP is less commonly studied as conventional mass spectrometry cannot distinguish the two heavy nitrogen isotopomers. Yoshida and Toyoda (2000) noted that tropospheric  $\text{N}_2\text{O}$  is enriched in  $^{15}\text{N}^\alpha$  over  $^{15}\text{N}^\beta$  by about  $+19\text{‰}$ . This preference increases with a depletion in  $^{15}\text{N}$ . Various nitrogen fixing pathways have different site preferences; nitrification shows a preference for  $^{15}\text{N}^\alpha$ , while denitrification does not show a preference (Sutka et al., 2006). However, nitrogen fixing does not fully account for the SP seen in tropospheric air; stratospheric air with a different isotopic composition must be mixing downward. As with other  $\text{N}_2\text{O}$  source isotopic information, SP is poorly isolated between specific sources (Snider et al., 2015), but reproducibility of SP data is poor among laboratories using different techniques (Mohn et al., 2014).

Triple oxygen isotope ratios of  $\text{N}_2\text{O}$  have not been extensively studied. The first surface measurements of  $\text{NN}^{17}\text{O}$  noted a  $\Delta^{17}\text{O}$  value of  $+1\text{‰}$  over a  $\delta^{18}\text{O}$  range of  $+40\text{‰}$  to  $+44\text{‰}$  (Cliff and Thiemens, 1997). Further samples collected via aircraft demonstrate that this  $^{17}\text{O}$  anomaly persists into the lower stratosphere (Cliff et al., 1999; Röckmann et al., 2001b).

Measurements of stratospheric  $\text{N}_2\text{O}$  isotopologues have been made at several locations around the world by balloon (Kaiser et al., 2006; Röckmann et al., 2001a; Toyoda, 2004; Toyoda et al., 2001) and aircraft (Park, 2004b). Enrichment in heavy isotopologues increases with altitude as  $\text{N}_2\text{O}$  concentrations drop with the sharpest gradients appearing within the polar vortex.  $\delta^{15}\text{N}^\alpha$  increases more rapidly than  $\delta^{15}\text{N}^\beta$ ; fractionation due to photolysis of  $\text{N}^{15}\text{NO}$  is stronger than that of  $^{15}\text{NNO}$  since the former has a lower zero-point energy (Yung and Miller, 1997).

Although  $\text{N}_2\text{O}$  isotopologues at several locations have been measured, measurements reach only to  $\sim 35$  km and global coverage of stratospheric  $\text{N}_2\text{O}$



isotopologues is lacking. Multiple space-based instruments including MIPAS (Plieninger et al., 2015), AIRS (Xiong et al., 2014), and CLEAS on UARS (Roche et al., 1996) have measured  $\text{N}_2\text{O}$  but do not have isotopologues data. This chapter presents measurements of  $\text{NN}^{18}\text{O}$ ,  $^{15}\text{NNO}$ , and  $\text{N}^{15}\text{NO}$  up to 45 km obtained by ACE-FTS. An associated model run with WACCM featuring these  $\text{N}_2\text{O}$  isotopologues was also performed.

## 8.2 Methods

The ACE data set used in this chapter consists of 28,842 occultations containing profiles of  $\text{N}_2\text{O}$  and the three heavy isotopologues  $\text{NN}^{18}\text{O}$ ,  $^{15}\text{NNO}$ , and  $\text{N}^{15}\text{NO}$ . The microwindows used for these species include lines from the  $2\nu_2$ ,  $\nu_3$ , and  $\nu_1$  vibrational modes along with a few additional lines that improve the fitting of some interfering species (Boone et al., 2013). A summary of the microwindows used is given in Table 10 and the list of interfering species is given in Table 11. The full microwindow list is given in Tables 21-24 in the Appendix.

Table 10: Microwindow summary for  $\text{N}_2\text{O}$  and its daughter isotopologues

Isotopologue	Altitude Range (km)	Number of microwindows	Vibrational modes and wavenumber ranges ( $\text{cm}^{-1}$ )
$\text{N}_2\text{O}$	5-95	66	$2\nu_2$ : 1134.2 – 1204.7 $\nu_3$ : 1264.7 – 1277.1 $\nu_1$ : 2201.8 – 2242.0 $2\nu_3$ : 2566.2 – 2623.9
$^{15}\text{NNO}$	7-45	35	$\nu_3$ : 1231.4 – 1250.7 $\nu_1$ : 2160.6 – 2220.9
$\text{N}^{15}\text{NO}$	5-45	41	$\nu_1$ : 2140.2 – 2196.8
$\text{NN}^{18}\text{O}$	5-45	40	$\nu_3$ : 1223.7 – 1235.5 $\nu_1$ : 2177.9 – 2333.6

Table 11: Interfering species for N<sub>2</sub>O and its daughter isotopologues

Isotopologue	Interfering species
N <sub>2</sub> O	<sup>15</sup> NNO, NN <sup>18</sup> O, H <sub>2</sub> O, HDO, H <sup>18</sup> OH, CO <sub>2</sub> , OC <sup>18</sup> O, O <sup>13</sup> C <sup>18</sup> O, CO, CH <sub>4</sub> , <sup>13</sup> CH <sub>4</sub> , CH <sub>3</sub> D, N <sup>15</sup> NO, O <sub>3</sub> , HNO <sub>3</sub> , CHF <sub>2</sub> Cl
<sup>15</sup> NNO	N <sub>2</sub> O, N <sup>15</sup> NO, NN <sup>18</sup> O, NN <sup>17</sup> O, H <sub>2</sub> O, HDO, CO <sub>2</sub> , <sup>13</sup> CO <sub>2</sub> , OC <sup>18</sup> O, O <sub>3</sub> , CO, CH <sub>4</sub> , <sup>13</sup> CH <sub>4</sub> , CH <sub>3</sub> D, H <sub>2</sub> O <sub>2</sub> , COF <sub>2</sub>
N <sup>15</sup> NO	N <sub>2</sub> O, <sup>15</sup> NNO, NN <sup>18</sup> O, NN <sup>17</sup> O, H <sub>2</sub> O, CO <sub>2</sub> , <sup>13</sup> CO <sub>2</sub> , OC <sup>18</sup> O, OC <sup>17</sup> O, O <sub>3</sub> , CO, <sup>13</sup> CO, C <sup>18</sup> O, C <sup>17</sup> O, CH <sub>4</sub> , <sup>13</sup> CH <sub>4</sub> , CH <sub>3</sub> D
NN <sup>18</sup> O	N <sub>2</sub> O, <sup>15</sup> NNO, N <sup>15</sup> NO, NN <sup>17</sup> O, H <sub>2</sub> O, HDO, <sup>13</sup> CO <sub>2</sub> , OC <sup>18</sup> O, OC <sup>17</sup> O, O <sub>3</sub> , CO, CH <sub>4</sub> , <sup>13</sup> CH <sub>4</sub> , CH <sub>3</sub> D, H <sub>2</sub> O <sub>2</sub> , COF <sub>2</sub>

The ACE N<sub>2</sub>O isotopic data set contains a large amount of unphysical data when compared to other molecules. Several steps were taken to remove this bad data and improve the final results. First, data flagged as outliers by analysis from Sheese et al. (2015) are removed. This reduced the number of occultations from 32,024 to 28,842. Next, profiles containing a negative VMR value are removed. While negative concentrations are allowed in ACE retrievals (where the value is very small and has a large absolute error), they are not valid when calculating delta values. This further reduced the number of occultations used to 17,183. Finally, filtering using the median absolute deviation (MAD) was performed. MAD is defined as

$$MAD = median_i(|x_i - median_j(x_j)|) \quad (59)$$

and is less sensitive than the standard deviation to extreme outliers. The data set was binned by season, 10° latitude, and each altitude level and a MAD was calculated for each bin. Values with an absolute deviation higher than the MAD multiplied by 5 were discarded. This did not remove any full profiles.

WACCM was modified to include support for the three heavy isotopologues, NN<sup>18</sup>O, <sup>15</sup>NNO, and N<sup>15</sup>NO, observed by ACE. Photolysis cross sections for the four isotopologues were taken from Schmidt et al. (2011) and include temperature and dependence. KIEs for the reaction with O(<sup>1</sup>D) were taken from (Kaiser and Brenninkmeijer, 2002). Although the base reaction shows a temperature dependence (Burkholder et al., 2015), fractionation is not significantly influenced by

temperature. An upper atmospheric source of  $\text{N}_2\text{O}$  via reactions 4-7 above was also implemented. Since isotopic fractionation of this reaction has not been investigated, a reasonable guess was made by forcing the reaction to produce an isotopic composition matching upper stratospheric measurements (Toyoda et al., 2001) The lower boundary condition for all locations was modified by  $\delta$  values of tropospheric air measured by Röckmann and Levin (2005). Since the atmospheric lifetime of  $\text{N}_2\text{O}$  is so long compared to tropospheric mixing, this essentially sets the isotopic abundance in the troposphere. Finally, initial conditions were modified from WACCM's built-in data using stratospheric isotopic measurements by Toyoda et al. (2001). The values used are summarized in Table 12 and include a photolysis  $\epsilon$  at 233 K and 200  $\mu\text{m}$  is provided for comparison with chemical loss to  $\text{O}(^1\text{D})$ .

Table 12: Summary of  $\text{N}_2\text{O}$  isotopologue modifications made to WACCM

Isotopologue	Chemical loss $\epsilon$ ( $\text{N}_2\text{O} + \text{O}(^1\text{D})$ )	Photolysis cross section $\epsilon$ (233 K, 200 $\mu\text{m}$ )	Tropospheric $\delta$
$^{15}\text{NNO}$	+8.87	+30.63	-15.8
$\text{N}^{15}\text{NO}$	+2.22	+69.86	+29.2
$\text{NN}^{18}\text{O}$	+12.38	+40.97	+44.62

Two additional isotopologues,  $\text{NN}^{17}\text{O}$  and  $^{15}\text{N}^{15}\text{NO}$ , were included for comparison with future versions of ACE retrievals. Photolysis data was available for these two isotopologues. Elsewhere,  $\text{NN}^{17}\text{O}$  was assumed to act mass-dependently, and fractionation of  $^{15}\text{N}^{15}\text{NO}$  was assumed to be an average of the two singly-substituted  $^{15}\text{N}$  isotopologues. The results of these isotopologues are not discussed further.

The model was given a spin-up time of 100 years at an eternal year 2000; three additional years were used for analysis. To account for the location bias in the ACE

data set, WACCM data presented here is sampled as a series of “profiles” at the same location and time of year as the ACE profiles.

### 8.3 Results and Discussion

#### 8.3.1 ACE-FTS data set

Figure 51 shows the mission median delta values for each heavy isotopologue sorted by season as a function of altitude and latitude. All three isotopologues show similar spatial and temporal patterns. Delta values up to 20 km are fairly noisy with averages of  $\delta^{15}\text{N}^{\alpha} = +28\text{‰}$ ,  $\delta^{15}\text{N}^{\beta} = -3\text{‰}$ , and  $\delta^{18}\text{O} = -2\text{‰}$ . A sharp increase is present in both  $^{15}\text{N}$  isotopologues at 20 km. Above 20 km, enrichment in all three isotopologues increases with altitude with the exception of a band of slight depletion at 35 km in  $\delta^{18}\text{O}$ .

The largest enrichment is present over the poles during the summer and fall months. Air over the poles is older due to Brewer-Dobson circulation and so is more highly enriched in the heavy isotopologues. Enrichment is especially high in the summer as photolysis is strongest during this time; this enrichment then persists through the fall. At 42 km below  $30^{\circ}$  latitude, enrichment lies around  $\delta^{15}\text{N}^{\alpha} = +220\text{‰}$  and  $\delta^{15}\text{N}^{\beta} = +110\text{‰}$ . At the same altitude at  $60^{\circ}$  latitude, enrichment ranges from roughly  $\delta^{15}\text{N}^{\alpha} = +250\text{‰}$  and  $\delta^{15}\text{N}^{\beta} = +200\text{‰}$  in the winter to  $\delta^{15}\text{N}^{\alpha} = +450\text{‰}$  and  $\delta^{15}\text{N}^{\beta} = +350\text{‰}$ . At these altitudes, the standard deviation of these measurements are very high, in excess of  $200\text{‰}$  (Figure 52), meaning the exact delta values above 40 km are unreliable. This is especially true for  $\delta^{18}\text{O}$ , where ACE reports values above  $+1000\text{‰}$  in the polar upper stratosphere. Nonetheless, the general patterns are real as they match both the patterns seen in other molecules such as methane (Chapter 4) and expectations from seasonality and dynamics.

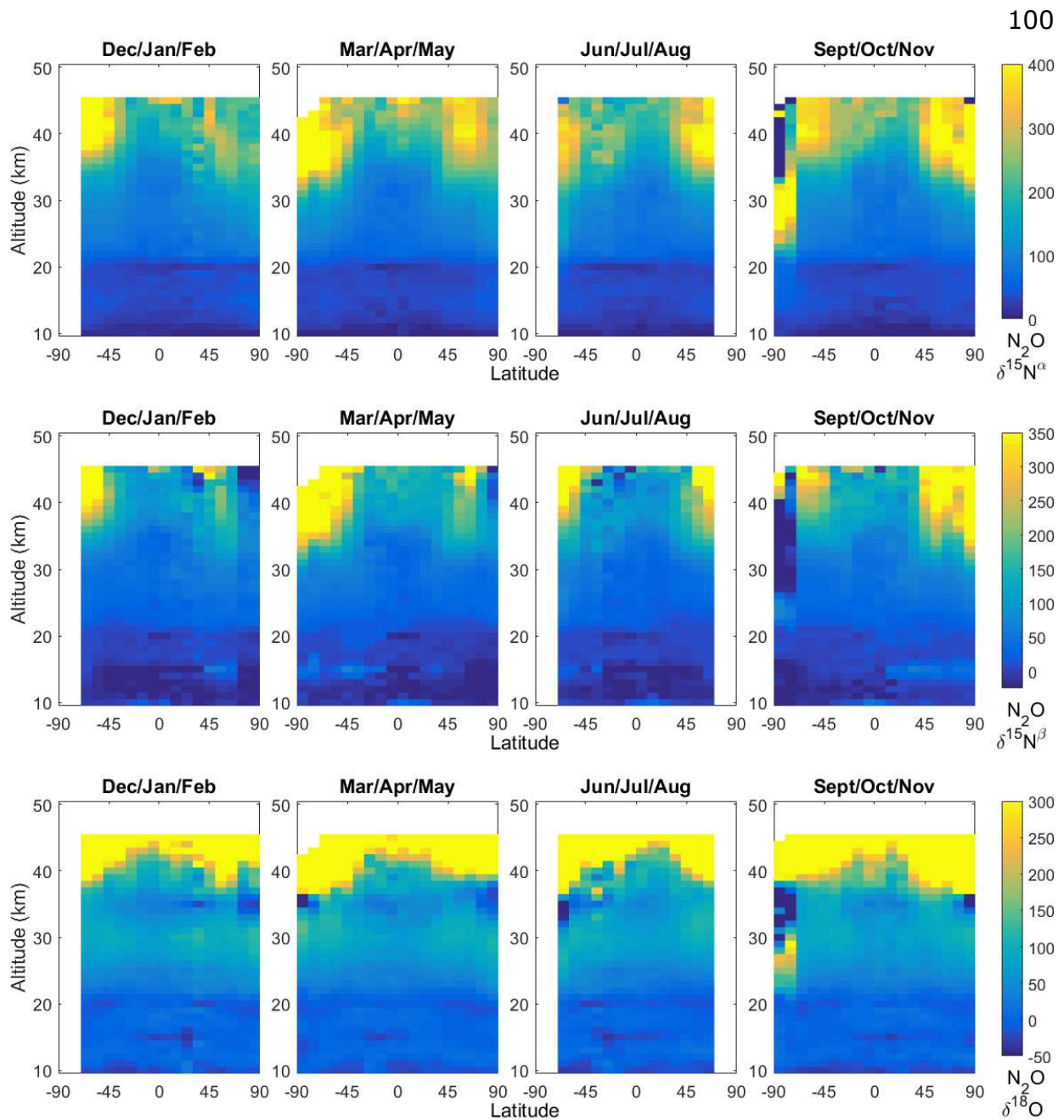


Figure 51: ACE-FTS  $\delta^{15}\text{N}^{\alpha}$  (top),  $\delta^{15}\text{N}^{\beta}$  (middle), and  $\delta^{18}\text{O}$  (bottom) mission median by season.

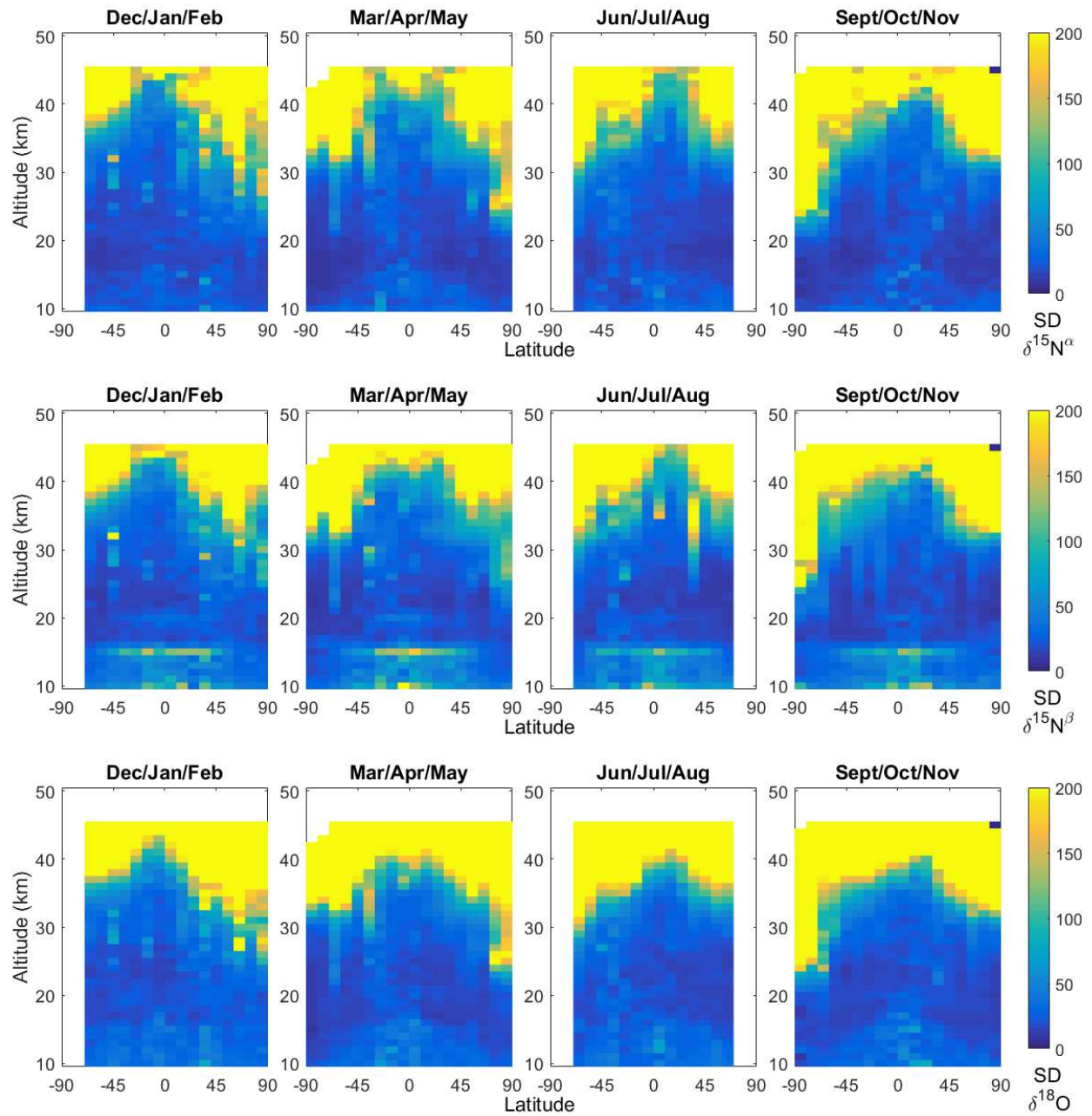


Figure 52: ACE-FTS  $\delta^{15}\text{N}^{\alpha}$  (top),  $\delta^{15}\text{N}^{\beta}$  (middle), and  $\delta^{18}\text{O}$  (bottom) mission standard deviation by season.

As with other previously observed isotopologues, several artifacts are present in the ACE data set. The sharp increase at 20 km in both  $\delta^{15}\text{N}$  and the depletion in  $\delta^{18}\text{O}$  at 35 are both at a constant altitude across the whole globe, a telltale sign that they are unphysical. In addition, profiles below 70°S from June to November show clearly inaccurate data. In the June-August bin, all of these profiles had negative concentrations and so were filtered out. In the September-November bin, some of these profiles were not filtered out, but the sharp changes between depletion and enrichment and very large standard deviations indicate that they are not real.

### 8.3.2 WACCM data set

The quarterly mean enrichment values for the three  $\text{N}_2\text{O}$  isotopologues from the WACCM run are given in Figure 53. All three isotopologues show very similar patterns in enrichment; this is unsurprising as they are subjected to the same dynamics and chemistry and only differ in kinetic isotope effects. The troposphere is well-mixed in all isotopologues with delta values of  $\delta^{15}\text{N}^{\alpha} = +33\text{‰}$ ,  $\delta^{15}\text{N}^{\beta} = -12\text{‰}$ , and  $\delta^{18}\text{O} = +44\text{‰}$ . Above 20 km, enrichment increases with altitude. As with the ACE measurements, delta values are lower over the Equator in the stratosphere, and the stronger enrichment is seen closer to the poles in the summer and fall. At 50 km over the North Pole, delta values reach  $\delta^{15}\text{N}^{\alpha} = +380\text{‰}$ ,  $\delta^{15}\text{N}^{\beta} = +129\text{‰}$ , and  $\delta^{18}\text{O} = +267\text{‰}$ .

Figure 54 shows monthly  $\delta^{15}\text{N}^{\beta}$  from WACCM and gives additional insight into the nature of the polar enrichment. This high enrichment begins forming in January (South Pole) and July (North Pole) in the upper stratosphere and mesosphere. The enriched air then travels downward, as low as 40 km by May/November, and mixes with the less enriched stratospheric air. By the wintertime, this air mass has fully dissipated.

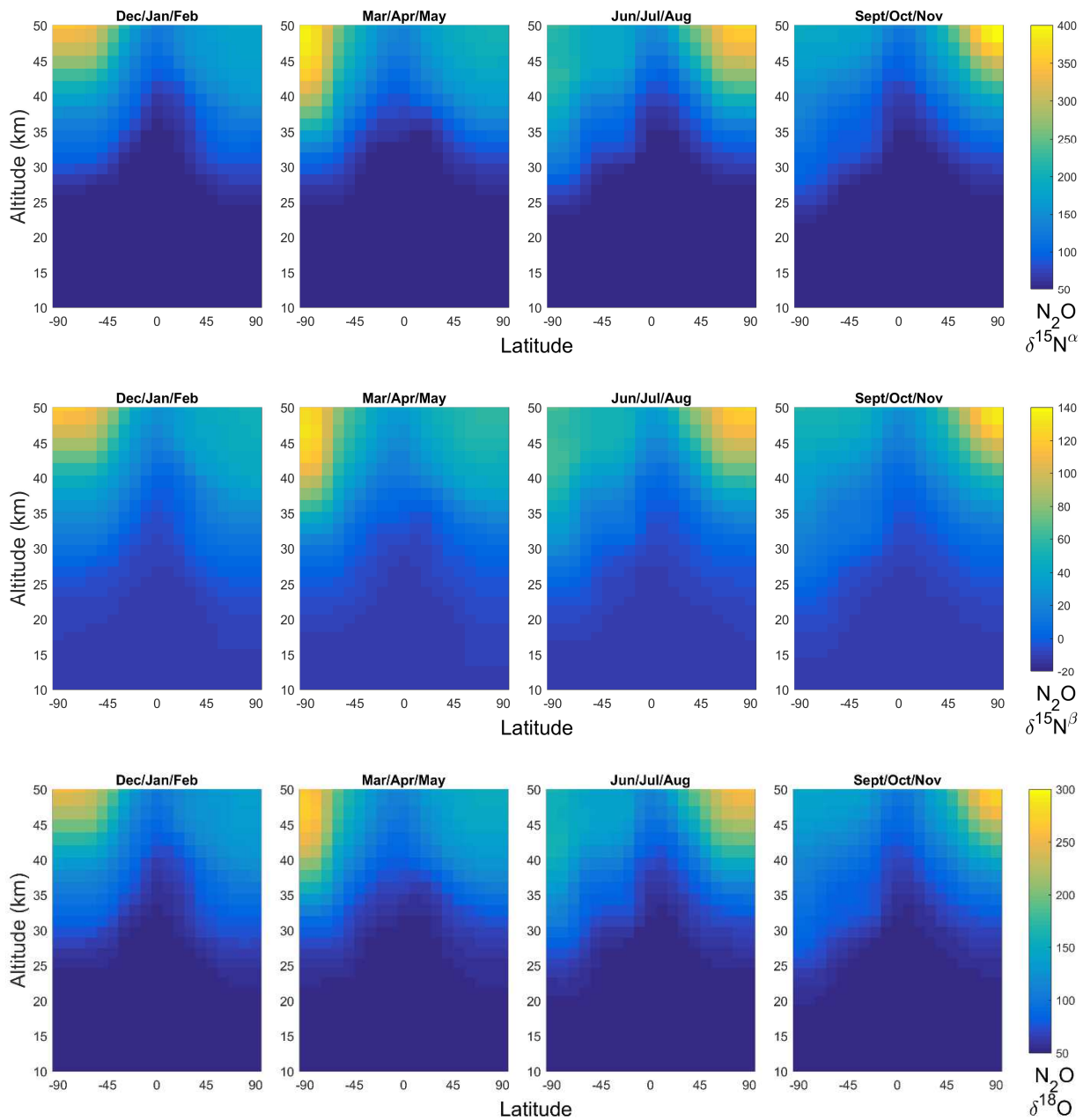


Figure 53: WACCM  $\delta^{15}\text{N}^{\alpha}$  (top),  $\delta^{15}\text{N}^{\beta}$  (middle), and  $\delta^{18}\text{O}$  (bottom) mean by season.



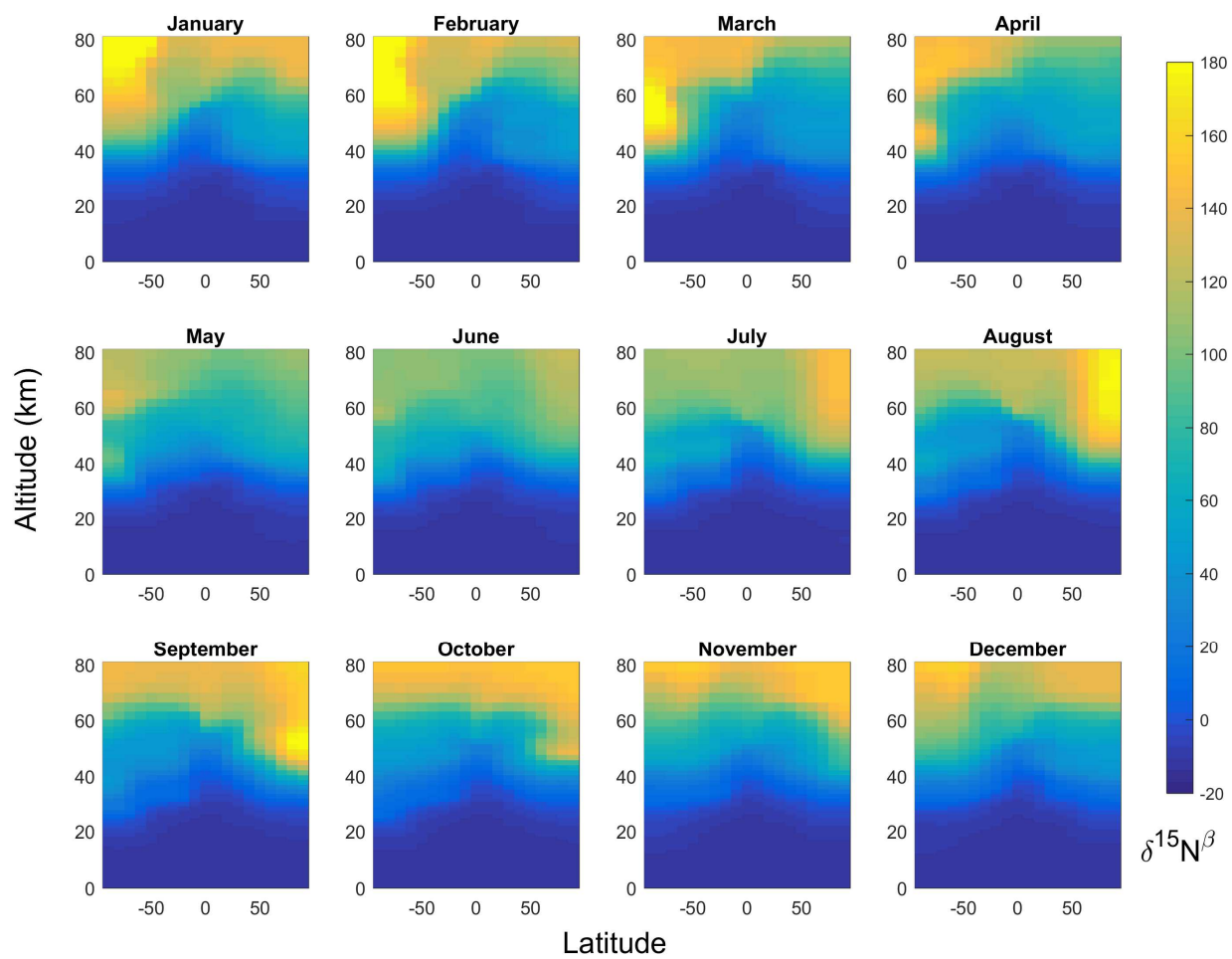


Figure 54:  $\delta^{15}\text{N}^\beta$  monthly average from WACCM

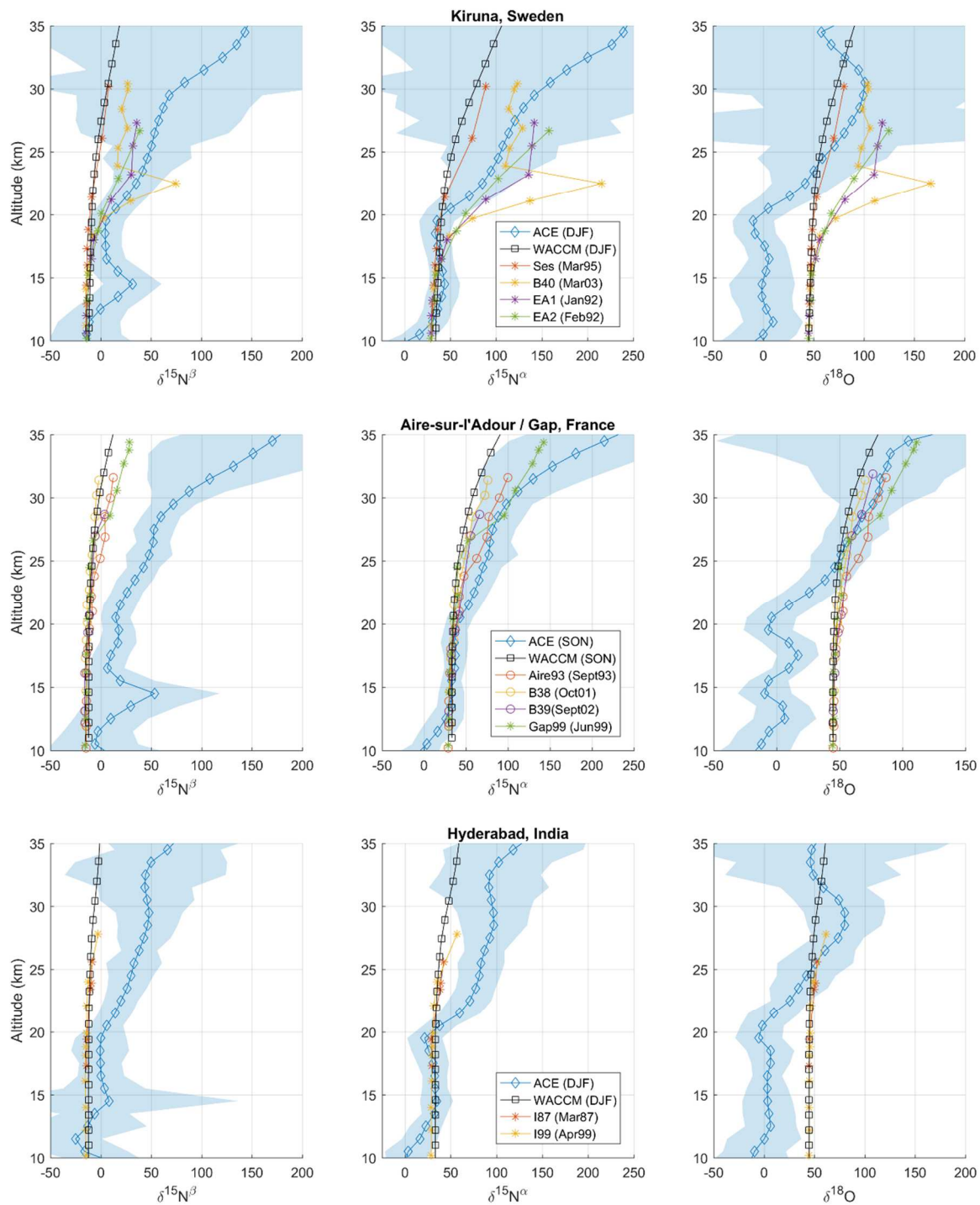


Figure 55: Comparison of ACE and WACCM to balloon profiles over Sweden (top), France (middle), and the Equator (bottom)

### 8.3.3 Comparison to balloon profiles

Figure 55 compares the ACE and WACCM data sets with balloon measurements collected by Kaiser et al. (2006). These measurements were made over Kiruna, Sweden (67.9°N, 21.10°E), Aire sur l'Adour, France (43.70°N, 0.30°E), Gap, France (44.44°N, 6.14°E), and Hyderabad, India (17.5°N, 78.6°E). In general, all profiles show increasing enrichment in all three isotopologues with a stronger increase closer to the poles.

Over Sweden, ACE shows good agreement with balloon measurements in  $\delta^{15}\text{N}^{\beta}$  (left) and  $\delta^{15}\text{N}^{\alpha}$  (center), though  $\delta^{15}\text{N}^{\beta}$  has a positive bias at higher altitudes. The results from WACCM closely match with the Ses balloon profile; both profiles show the lowest enrichment of all the compared data. The large variation in measurements can likely be attributed to the influence of the polar vortex from month to month and year to year. Similar patterns are seen over France, though the balloon profiles show less variation. Again both  $^{15}\text{N}$  isotopologues show good agreement with a small positive bias in  $\delta^{15}\text{N}^{\beta}$  from ACE. Over India,  $\delta^{15}\text{N}^{\beta}$  and  $\delta^{15}\text{N}^{\alpha}$  begin to deviate above 20 km. At all locations, ACE underestimates  $\delta^{18}\text{O}$  below 20 km but has good agreement above 25 km.

### 8.3.4 Similarities between $\text{N}_2\text{O}$ and $\text{CH}_4$

VMRs of  $\text{N}_2\text{O}$  and  $\text{CH}_4$  in the atmosphere are known to be strongly correlated (Minschwaner and Manney, 2014). In particular, measurements of the two gases from ATMOS demonstrated that the tropics and polar have tight, distinct correlations, while mid-latitude air is less compact but still correlated. In addition, little variability is seen between seasons and hemispheres (Michelsen et al., 1998). The overall correlation as well as the distinct equatorial pattern is clearly present in the ACE data set (Figure 56).

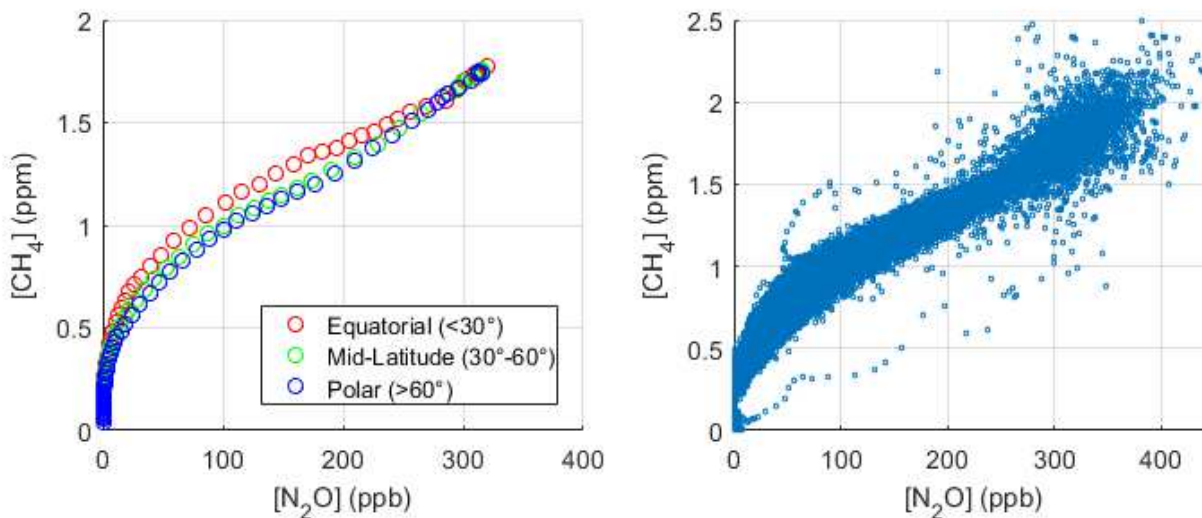


Figure 56:  $\text{N}_2\text{O}$  vs  $\text{CH}_4$  mixing ratios in the ACE dataset. The median value by  $30^\circ$  latitude is shown on the left, and the mission-long dataset with low-quality profiles removed is shown on the right.

The strong correlation between  $\text{CH}_4$  and  $\text{N}_2\text{O}$  is due to their similar behavior in the atmosphere. In the troposphere, both gases are only emitted from the surface and are well-mixed due to their long lifetimes. In the stratosphere, the primary source of both is upwelling from the tropical troposphere. Their destruction is also controlled by sunlight; photolysis is the primary sink of  $\text{N}_2\text{O}$ , and  $\text{CH}_4$  is primarily consumed by OH which is produced by  $\text{O}(^1\text{D})$  from  $\text{O}_3$  photolysis.

Isotopic data can give additional information on the correlation between  $\text{CH}_4$  and  $\text{N}_2\text{O}$  since they are highly sensitive to small changes in concentration and the relative strengths of sinks. Although the ACE data set is too noisy to perform a quantitative analysis, some qualitative patterns can be discerned from ACE and WACCM.

Both  $\text{N}_2\text{O}$  and  $\text{CH}_4$  have similar isotopic distributions in the stratosphere. The lowest enrichments are seen near the tropopause, and the highest enrichments are seen over the poles in the winter and spring. However, the behavior of the enriched polar air differs between the two molecules. According to WACCM (Figure 26 and Figure 27), polar enrichment in  $\text{CH}_3\text{D}$  and  $^{13}\text{CH}_4$  begins in the summer in the lower mesosphere and persists through the winter as it mixes downward. In contrast,  $\text{N}_2\text{O}$

enrichment (Figure 53) disappears over the pole by wintertime. In addition, the enriched  $\text{CH}_4$  reaches lower altitudes than  $\text{N}_2\text{O}$  does. This is clearly visible in the ACE data set where the polar spike in  $\text{CH}_3\text{D}$  is detectable below 30 km, whereas heavy  $\text{N}_2\text{O}$  enrichment is only seen down to 35 km. This difference in altitude may be due to the dependence on different regions of UV light to photolyze ozone ( $\lambda < 320$  nm) and  $\text{N}_2\text{O}$  ( $\lambda < 220$  nm).

## 8.4 Conclusions

The ACE data set presented in this chapter extends isotopic measurements of  $\text{N}_2\text{O}$  over the majority of the globe and up to 46 km. The  $\text{N}_2\text{O}$  isotopic abundance in the stratosphere acts similar to methane, where enrichment increases with altitude and peaks over the poles during the summer and fall months. Modeling with WACCM confirms that photolysis is primarily responsible for this pattern of enrichment. Though very noisy in the upper stratosphere, the ACE data set shows good agreement with balloon measurements up to 35 km depending on the isotopologue.

## SUMMARY

Measurements by ACE-FTS have extended the vertical range of some of the isotopologues of CH<sub>4</sub>, CO, CO<sub>2</sub>, and N<sub>2</sub>O to new altitudes in the stratosphere and mesosphere. Nearly global coverage has also been achieved, a large improvement over current balloon measurements that are restricted to a few locations. Though the ACE datasets have noticeable artifacts, when combined with modeling results from WACCM, they reveal several spatial and seasonal patterns in these species.

CH<sub>4</sub> and N<sub>2</sub>O behave similarly in the stratosphere due to their shared atmospheric sinks. Both molecules show enrichment at higher altitudes and near the poles with especially high enrichment in the wintertime, a possible interaction with the polar vortex.

<sup>13</sup>CO is enriched throughout the stratosphere and in the polar mesosphere in the winter as a result of downwelling of CO-rich air from the thermosphere. WACCM does not properly model the enrichment in the stratosphere; this is likely due to WACCM modeling a limited set of organic compounds that can oxidize to form CO.

Mesospheric CO<sub>2</sub> continues to show mass-independent fractionation in the mesosphere, though it is weaker than that seen in the stratosphere. In this altitude range, CO<sub>2</sub> may undergo isotopic exchange with species besides ozone, the source of the strong enrichment and mass-independent fractionation at lower altitudes. Also, the altitude of maximum enrichment in the mesosphere is different for δ<sup>18</sup>O and δ<sup>17</sup>O for an unknown reason.

Many improvements can still be made to the ACE datasets. Most pressing is the elimination of latitude-independent "spikes" in enrichment seen in the stratosphere. Improvements have already been made to CH<sub>4</sub> from the addition and adjustment of microwindows to decrease residuals between different absorption bands. These enhancements should be performed on other species as well. Furthermore, validation of the ACE datasets requires outside measurements which are currently limited in location and altitude. Ideally, other satellite missions that measure isotopologues would be ideal as they can obtain wide coverage of the Earth. Lacking that, additional measurements via balloon or sounding rockets at new locations and altitudes would be useful.

## REFERENCES

- Alexander, B., Vollmer, M. K., Jackson, T., Weiss, R. F. and Thiemens, M. H.: Stratospheric CO<sub>2</sub> isotopic anomalies and SF<sub>6</sub> and CFC Tracer Concentrations in the Arctic Polar Vortex, *Geophys. Res. Lett.*, 28(21), 4103–4106, doi:10.1029/2001GL013692, 2001.
- Allan, W., Manning, M. R., Lassey, K. R., Lowe, D. C. and Gomez, A. J.: Modeling the variation of  $\delta^{13}\text{C}$  in atmospheric methane: Phase ellipses and the kinetic isotope effect, *Global Biogeochem. Cycles*, 15(2), 467–481, doi:10.1029/2000GB001282, 2001.
- Andrews, A. E., Kofler, J. D., Trudeau, M. E., Williams, J. C., Neff, D. H., Masarie, K. A, Chao, D. Y., Kitzis, D. R., Novelli, P. C., Zhao, C. L., Dlugokencky, E. J., Lang, P. M., Crotwell, M. J., Fischer, M. L., Parker, M. J., Lee, J. T., Baumann, D. D., Desai, A. R., Stanier, C. O., De Wekker, S. F. J., Wolfe, D. E., Munger, J. W. and Tans, P. P.: CO<sub>2</sub>, CO, and CH<sub>4</sub> measurements from tall towers in the NOAA Earth System Research Laboratory's Global Greenhouse Gas Reference Network: instrumentation, uncertainty analysis, and recommendations for future high-accuracy greenhouse gas, *Atmos. Meas. Tech.*, 7(2), 647–687, doi:10.5194/amt-7-647-2014, 2014.
- Anslyn, E. V. and Dougherty, D. A.: *Modern Physical Organic Chemistry*, University Science Books, 2006.
- Assonov, S. S., Brenninkmeijer, C. a. M., Schuck, T. J. and Taylor, P.: Analysis of <sup>13</sup>C and <sup>18</sup>O isotope data of CO<sub>2</sub> in CARIBIC aircraft samples as tracers of upper troposphere/lower stratosphere mixing and the global carbon cycle, *Atmos. Chem. Phys.*, 10(17), 8575–8599, doi:10.5194/acp-10-8575-2010, 2010.
- Barkan, E. and Luz, B.: High precision measurements of <sup>17</sup>O/<sup>16</sup>O and <sup>18</sup>O/<sup>16</sup>O ratios in H<sub>2</sub>O, *Rapid Commun. Mass Spectrom.*, 19(24), 3737–3742, doi:10.1002/rcm.2250, 2005.
- Beagley, S. R., Boone, C. D., Fomichev, V. I., Jin, J. J., Semeniuk, K., McConnell, J. C. and Bernath, P. F.: First multi-year occultation observations of CO<sub>2</sub> in the MLT by ACE satellite: observations and analysis using the extended CMAM, *Atmos. Chem. Phys.*, 10(3), 1133–1153, doi:10.5194/acp-10-1133-2010, 2010.

- Bergamaschi, P., Brenninkmeijer, C. A. M., Hahn, M., Röckmann, T., Scharffe, D. H., Crutzen, P. J., Elansky, N. F., Belikov, I. B., Trivett, N. B. A. and Worthy, D. E. J.: Isotope analysis based source identification for atmospheric CH<sub>4</sub> and CO sampled across Russia using the Trans-Siberian railroad, *J. Geophys. Res. Atmos.*, 103(D7), 8227–8235, doi:10.1029/97JD03738, 1998.
- Bergamaschi, P., Hein, R., Brenninkmeijer, C. A. M. and Crutzen, P. J.: Inverse modeling of the global CO cycle: 2. Inversion of <sup>13</sup>C/<sup>12</sup>C and <sup>18</sup>O/<sup>16</sup>O isotope ratios, *J. Geophys. Res. Atmos.*, 105(D2), 1929–1945, doi:10.1029/1999JD900819, 2000.
- Bernard, S., Röckmann, T., Kaiser, J., Barnola, J.-M., Fischer, H., Blunier, T. and Chappellaz, J.: Constraints on N<sub>2</sub>O budget changes since pre-industrial time from new firn air and ice core isotope measurements, *Atmos. Chem. Phys.*, 6(2), 493–503, doi:10.5194/acp-6-493-2006, 2006.
- Bernath, P. F.: *Spectra of Atoms and Molecules*, 3rd ed., Oxford University Press, New York., 2016.
- Bernath, P. F.: The Atmospheric Chemistry Experiment (ACE), *J. Quant. Spectrosc. Radiat. Transf.*, 186(SP-636), 3–16, doi:10.1016/j.jqsrt.2016.04.006, 2017.
- Bischof, W., Borchers, R., Fabian, P. and Krüger, B. C.: Increased concentration and vertical distribution of carbon dioxide in the stratosphere, *Nature*, 316(6030), 708–710, doi:10.1038/316708a0, 1985.
- Bönisch, H., Engel, A., Birner, T., Hoor, P., Tarasick, D. W. and Ray, E. A.: On the structural changes in the Brewer-Dobson circulation after 2000, *Atmos. Chem. Phys.*, 11(8), 3937–3948, doi:10.5194/acp-11-3937-2011, 2011.
- Boone, C. D., Walker, K. A. and Bernath, P. F.: Version 3 Retrievals of the Atmospheric Chemistry Experiment Fourier Transform Spectrometer (ACE-FTS), in *The Atmospheric Chemistry Experiment: ACE at 10*, edited by P. F. Bernath, pp. 103–127, A. Deepak Publishing, Hampton, VA. [online] Available from: <http://www.ace.uwaterloo.ca/publications/2013/Version3.5retrievals2013.pdf>, 2013.
- Bovensmann, H., Burrows, J. P., Buchwitz, M., Frerick, J., Noël, S., Rozanov, V. V., Chance, K. V. and Goede, a. P. H.: SCIAMACHY: Mission Objectives and Measurement Modes, *J. Atmos. Sci.*, 56(2), 127–150, doi:10.1175/1520-



0469(1999)056<0127:SMOAMM>2.0.CO;2, 1999.

- Brenninkmeijer, C. A. M., Röckmann, T., Bräunlich, M., Jöckel, P., Bergamaschi, P., Brenninkmeijer, C. A. ., Röckmann, T., Bräunlich, M., Jöckel, P. and Bergamaschi, P.: Review of progress in isotope studies of atmospheric carbon monoxide, *Chemosph. - Glob. Chang. Sci.*, 1(1–3), 33–52, doi:10.1016/S1465-9972(99)00018-5, 1999.
- Brenninkmeijer, C. A. M., Crutzen, P., Boumard, F., Dauer, T., Dix, B., Ebinghaus, R., Filippi, D., Fischer, H., Franke, H., Frieß, U., Heintzenberg, J., Helleis, F., Hermann, M., Kock, H. H., Koeppel, C., Lelieveld, J., Leuenberger, M., Martinsson, B. G., Miemczyk, S., Moret, H. P., Nguyen, H. N., Nyfeler, P., Oram, D., O’Sullivan, D., Penkett, S., Platt, U., Pupek, M., Ramonet, M., Randa, B., Reichelt, M., Rhee, T. S., Rohwer, J., Rosenfeld, K., Scharffe, D., Schlager, H., Schumann, U., Slemr, F., Sprung, D., Stock, P., Thaler, R., Valentino, F., van Velthoven, P., Waibel, A., Wandel, A., Waschitschek, K., Wiedensohler, A., Xueref-Remy, I., Zahn, A., Zech, U. and Ziereis, H.: Civil aircraft for the regular investigation of the atmosphere based on an instrumented container: the new CARIBIC system, *Atmos. Chem. Phys.*, 7(2), 5277–5339, doi:10.5194/acpd-7-5277-2007, 2007.
- Buijs, H. J., Soucy, M.-A. and Lachance, R. L.: ACE-FTS Hardware and Level 1 Processing, in *The Atmospheric Chemistry Experiment: ACE at 10*, edited by P. F. Bernath, pp. 53–80, A. Deepak Publishing, Hampton, VA., 2013.
- Burkholder, J. B., Sander, S. P., Abbatt, J., Barker, J. R., Huie, R. E., Kolb, C. E., Kurylo, M. J., Orkin, V. L., Wilmouth, D. M. and Wine, P. H.: *Chemical Kinetics and Photochemical Data for Use in Atmospheric Studies Evaluation Number 18*, Pasadena, CA. [online] Available from: <http://jpldataeval.jpl.nasa.gov>, 2015.
- Chakraborty, S. and Bhattacharya, S. K.: Experimental investigation of oxygen isotope exchange between CO<sub>2</sub> and O(<sup>1</sup>D) and its relevance to the stratosphere, *J. Geophys. Res.*, 108(D23), 4724, doi:10.1029/2002JD002915, 2003.
- Ciais, P., Sabine, C., Bala, G., Bopp, L., Brovkin, V., Canadell, J., Chhabra, A., DeFries, R., Galloway, J., Heimann, M., Jones, C., Quéré, C. Le, Myneni, R. B., Piao, S. and Thornton, P.: Carbon and Other Biogeochemical Cycles, in *Climate Change 2013: The Physical Science Basis*, edited by T. F. Stocker, D. Qin, G.-K.

- Plattner, M. Tignor, S. K. Allen, J. Boschung, A. Nauels, Y. Xia, V. Bex, and P. M. Midgley, pp. 465–570, Cambridge University Press, Cambridge, United Kingdom., 2013.
- Clerbaux, C., George, M., Turquety, S., Walker, K. A., Barret, B., Bernath, P., Boone, C., Borsdorff, T., Cammas, J. P., Catoire, V., Coffey, M., Coheur, P.-F., Deeter, M., De Mazière, M., Drummond, J., Duchatelet, P., Dupuy, E., de Zafra, R., Eddounia, F., Edwards, D. P., Emmons, L., Funke, B., Gille, J., Griffith, D. W. T., Hannigan, J., Hase, F., Höpfner, M., Jones, N., Kagawa, A., Kasai, Y., Kramer, I., Le Flochmoën, E., Livesey, N. J., López-Puertas, M., Luo, M., Mahieu, E., Murtagh, D., Nédélec, P., Pazmino, A., Pumphrey, H., Ricaud, P., Rinsland, C. P., Robert, C., Schneider, M., Senten, C., Stiller, G., Strandberg, A., Strong, K., Sussmann, R., Thouret, V., Urban, J. and Wiacek, A.: CO measurements from the ACE-FTS satellite instrument: data analysis and validation using ground-based, airborne and spaceborne observations, *Atmos. Chem. Phys.*, 8(9), 2569–2594, doi:10.5194/acp-8-2569-2008, 2008.
- Cliff, S. S. and Thiemens, M. H.: The  $^{18}\text{O}/^{16}\text{O}$  and  $^{17}\text{O}/^{16}\text{O}$  Ratios in Atmospheric Nitrous Oxide: A Mass-Independent Anomaly, *Science*, 278(5344), 1774–1776, doi:10.1126/science.278.5344.1774, 1997.
- Cliff, S. S., Brenninkmeijer, C. A. M. and Thiemens, M. H.: First measurement of the  $^{18}\text{O}/^{16}\text{O}$  and  $^{17}\text{O}/^{16}\text{O}$  ratios in stratospheric nitrous oxide: A mass-independent anomaly, *J. Geophys. Res. Atmos.*, 104(D13), 16171–16175, doi:10.1029/1999JD900152, 1999.
- CMG Lee: Comparison US standard atmosphere 1962, [online] Available from: [https://commons.wikimedia.org/wiki/File:Comparison\\_US\\_standard\\_atmosphere\\_1962.svg](https://commons.wikimedia.org/wiki/File:Comparison_US_standard_atmosphere_1962.svg) (Accessed 1 May 2017), 2015.
- Conny, J. M. and Currie, L. A.: The isotopic characterization of methane, non-methane hydrocarbons and formaldehyde in the troposphere, *Atmos. Environ.*, 30(4), 621–638, doi:10.1016/1352-2310(95)00305-3, 1996.
- Daniel, J. S. and Solomon, S.: On the climate forcing of carbon monoxide, *J. Geophys. Res.*, 103(D11), 13249–13260, 1998.
- Deeter, M. N.: Operational carbon monoxide retrieval algorithm and selected results for the MOPITT instrument, *J. Geophys. Res.*, 108(D14), 4399,

doi:10.1029/2002JD003186, 2003.

- Ehhalt, D. and Prather, M.: Atmospheric Chemistry and Greenhouse Gases, *Clim. Chang.* 2001 Sci. Basis, 239–287, doi:10.2753/JES1097-203X330403, 2001.
- Emmert, J. T., Stevens, M. H., Bernath, P. F., Drob, D. P. and Boone, C. D.: Observations of increasing carbon dioxide concentration in Earth's thermosphere, *Nat. Geosci.*, 5(12), 868–871, doi:10.1038/ngeo1626, 2012.
- Emmons, L. K., Walters, S., Hess, P. G., Lamarque, J.-F., Pfister, G. G., Fillmore, D., Granier, C., Guenther, A., Kinnison, D., Laepple, T., Orlando, J., Tie, X., Tyndall, G., Wiedinmyer, C., Baughcum, S. L. and Kloster, S.: Description and evaluation of the Model for Ozone and Related chemical Tracers, version 4 (MOZART-4), *Geosci. Model Dev.*, 3(1), 43–67, doi:10.5194/gmd-3-43-2010, 2010.
- Etheridge, D. M., Steele, L. P., Francey, R. J. and Langenfelds, R. L.: Atmospheric methane between 1000 A.D. and present: Evidence of anthropogenic emissions and climatic variability, *J. Geophys. Res.*, 103(D13), 15979, doi:10.1029/98JD00923, 1998.
- Feilberg, K. L., Johnson, M. S. and Nielsen, C. J.: Relative Reaction Rates of HCHO, HCDO, DCDO, H<sup>13</sup>CHO, and HCH<sup>18</sup>O with OH, Cl, Br, and NO<sub>3</sub> Radicals, *J. Phys. Chem. A*, 108(36), 7393–7398, doi:10.1021/jp048329k, 2004.
- Feilberg, K. L., Johnson, M. S. and Nielsen, C. J.: Relative rates of reaction of <sup>13</sup>C<sup>16</sup>O, <sup>12</sup>C<sup>18</sup>O, <sup>12</sup>C<sup>17</sup>O and <sup>13</sup>C<sup>18</sup>O with OH and OD radicals, *Phys. Chem. Chem. Phys.*, 7(11), 2318, doi:10.1039/b503350k, 2005a.
- Feilberg, K. L., Griffith, D. W. T., Johnson, M. S. and Nielsen, C. J.: The <sup>13</sup>C and D kinetic isotope effects in the reaction of CH<sub>4</sub> with Cl, *Int. J. Chem. Kinet.*, 37(2), 110–118, doi:10.1002/kin.20058, 2005b.
- Fischer, H., Birk, M., Blom, C., Carli, B., Carlotti, M., von Clarmann, T., Delbouille, L., Dudhia, A., Ehhalt, D., Endemann, M., Flaud, J. M., Gessner, R., Kleinert, A., Koopman, R., Langen, J., López-Puertas, M., Mosner, P., Nett, H., Oelhaf, H., Perron, G., Remedios, J., Ridolfi, M., Stiller, G. and Zander, R.: MIPAS: an instrument for atmospheric and climate research, *Atmos. Chem. Phys.*, 8(8), 2151–2188, doi:10.5194/acp-8-2151-2008, 2008.
- Forbes, J. M.: Dynamics of the Thermosphere, *J. Meteorol. Soc. Japan*, 85B(2),

193–213, doi:10.2151/jmsj.85B.193, 2007.

- Foucher, P. Y., Chédin, A., Armante, R., Boone, C., Crevoisier, C. and Bernath, P.: Carbon dioxide atmospheric vertical profiles retrieved from space observation using ACE-FTS solar occultation instrument, *Atmos. Chem. Phys.*, 11(6), 2455–2470, doi:10.5194/acp-11-2455-2011, 2011.
- Funke, B., García-Comas, M., López-Puertas, M., Glatthor, N., Stiller, G. P., von Clarmann, T., Semeniuk, K. and McConnell, J. C.: Enhancement of N<sub>2</sub>O during the October–November 2003 solar proton events, *Atmos. Chem. Phys.*, 8(14), 3805–3815, doi:10.5194/acp-8-3805-2008, 2008.
- Funke, B., López-Puertas, M., García-Comas, M., Stiller, G. P., von Clarmann, T., Höpfner, M., Glatthor, N., Grabowski, U., Kellmann, S. and Linden, A.: Carbon monoxide distributions from the upper troposphere to the mesosphere inferred from 4.7  $\mu$ m non-local thermal equilibrium emissions measured by MIPAS on Envisat, *Atmos. Chem. Phys.*, 9(7), 2387–2411, doi:10.5194/acp-9-2387-2009, 2009.
- Gamo, T., Tsutsumi, M., Sakai, H., Nakazawa, T., Tanaka, M., Honda, H., Kubo, H. and Itoh, T.: Carbon and oxygen isotopic ratios of carbon dioxide of a stratospheric profile over Japan, *Tellus B*, 41B(2), 127–133, doi:10.1111/j.1600-0889.1989.tb00130.x, 1989.
- Gans, P.: FTIR Interferometer, [online] Available from: [https://commons.wikimedia.org/wiki/File:FTIR\\_Interferometer.png](https://commons.wikimedia.org/wiki/File:FTIR_Interferometer.png) (Accessed 1 May 2017), 2011.
- George, M., Clerbaux, C., Hurtmans, D., Turquety, S., Coheur, P.-F., Pommier, M., Hadji-Lazarou, J., Edwards, D. P., Worden, H., Luo, M., Rinsland, C. and McMillan, W.: Carbon monoxide distributions from the IASI/METOP mission: evaluation with other space-borne remote sensors, *Atmos. Chem. Phys.*, 9(21), 8317–8330, doi:10.5194/acp-9-8317-2009, 2009.
- Gierczak, T., Talukdar, R. K., Herndon, S. C., Vaghjiani, G. L. and Ravishankara, A. R.: Rate Coefficients for the Reactions of Hydroxyl Radicals with Methane and Deuterated Methanes, *J. Phys. Chem. A*, 101(17), 3125–3134, doi:10.1021/jp963892r, 1997.
- Gola, A. A., D’Anna, B., Feilberg, K. L., Sellevåg, S. R., Bache-Andreassen, L. and

- Nielsen, C. J.: Kinetic isotope effects in the gas phase reactions of OH and Cl with CH<sub>3</sub>Cl, CD<sub>3</sub>Cl, and <sup>13</sup>CH<sub>3</sub>Cl, *Atmos. Chem. Phys.*, 5(9), 2395–2402, doi:10.5194/acp-5-2395-2005, 2005.
- Gromov, S. and Brenninkmeijer, C. A. M.: An estimation of the <sup>18</sup>O/<sup>16</sup>O ratio of UT/LMS ozone based on artefact CO in air sampled during CARIBIC flights, *Atmos. Chem. Phys.*, 15(4), 1901–1912, doi:10.5194/acp-15-1901-2015, 2015.
- Gros, V., Bräunlich, M., Röckmann, T., Jöckel, P., Bergamaschi, P., Brenninkmeijer, C. A. M., Rom, W., Kutschera, W., Kaiser, A., Scheel, H. E., Mandl, M., van der Plicht, J. and Possnert, G.: Detailed analysis of the isotopic composition of CO and characterization of the air masses arriving at Mount Sonnblick (Austrian Alps), *J. Geophys. Res. Atmos.*, 106(D3), 3179–3193, doi:10.1029/2000JD900509, 2001.
- Gunson, M. R., Abbas, M. M., Abrams, M. C., Allen, M., Brown, L. R., Brown, T. L., Chang, A. Y., Goldman, A., Irion, F. W., Lowes, L. L., Mahieu, E., Manney, G. L., Michelsen, H. A., Newchurch, M. J., Rinsland, C. P., Salawitch, R. J., Stiller, G. P., Toon, G. C., Yung, Y. L. and Zander, R.: The Atmospheric Trace Molecule Spectroscopy (ATMOS) Experiment: Deployment on the ATLAS space shuttle missions, *Geophys. Res. Lett.*, 23(17), 2333–2336, doi:10.1029/96GL01569, 1996.
- Haan, D. and Raynaud, D.: Ice core record of CO variations during the last two millennia: atmospheric implications and chemical interactions within the Greenland ice, *Tellus B*, 50(3), 253–262, doi:10.1034/j.1600-0889.1998.t01-2-00004.x, 1998.
- Haan, D., Martinerie, P. and Raynaud, D.: Ice core data of atmospheric carbon monoxide over Antarctica and Greenland during the last 200 years, *Geophys. Res. Lett.*, 23(17), 2235–2238, doi:10.1029/96GL02137, 1996.
- Hall, M., McKemy, D. and Lee, A.: Coriolis Effect, [online] Available from: <http://climate.ncsu.edu/edu/k12/.coriolis> (Accessed 1 May 2017), 2013.
- Hartmann, D. L., Tank, A. M. G. K., Rusticucc, M., Alexander, L. V., Brönnimann, S., Charabi, Y., Dentener, F. J., Dlugokencky, E. J., Easterling, D. R., Kaplan, A., Soden, B. J., Thorne, P. W., Wild, M. and Zhai, P. M.: Observations: Atmosphere and Surface, in *Climate Change 2013: The Physical Science Basis*, edited by T.

- F. Stocker, D. Qin, G.-K. Plattner, M. Tignor, S. K. Allen, J. Boschung, A. Nauels, Y. Xia, V. Bex, and P. M. Midgley, pp. 159–254, Cambridge University Press, Cambridge, United Kingdom., 2013.
- Haverd, V., Toon, G. C. and Griffith, D. W. T.: Evidence for altitude-dependent photolysis-induced  $^{18}\text{O}$  isotopic fractionation in stratospheric ozone, *Geophys. Res. Lett.*, 32(22), L22808, doi:10.1029/2005GL024049, 2005.
- Jacob, D. J.: Introduction to Atmospheric Chemistry, Princeton University Press, Princeton, NJ., 2000.
- Jacob, D. J.: Models of Atmospheric Transport and Chemistry. [online] Available from: <http://acmg.seas.harvard.edu/education.html>, 2007.
- Kaidor: Earth Global Circulation, [online] Available from: [https://commons.wikimedia.org/wiki/File:Earth\\_Global\\_Circulation\\_-\\_en.svg](https://commons.wikimedia.org/wiki/File:Earth_Global_Circulation_-_en.svg) (Accessed 1 May 2017), 2015.
- Kaiser, J.: Complete and accurate mass spectrometric isotope analysis of tropospheric nitrous oxide, *J. Geophys. Res.*, 108(D15), 4476, doi:10.1029/2003JD003613, 2003.
- Kaiser, J. and Brenninkmeijer, C. A. M.: Intramolecular  $^{15}\text{N}$  and  $^{18}\text{O}$  fractionation in the reaction of  $\text{N}_2\text{O}$  with  $\text{O}(^1\text{D})$  and its implications for the stratospheric  $\text{N}_2\text{O}$  isotope signature, *J. Geophys. Res.*, 107(D14), 4214, doi:10.1029/2001JD001506, 2002.
- Kaiser, J., Engel, A., Borchers, R. and Röckmann, T.: Probing stratospheric transport and chemistry with new balloon and aircraft observations of the meridional and vertical  $\text{N}_2\text{O}$  isotope distribution, *Atmos. Chem. Phys.*, 6(11), 3535–3556, doi:10.5194/acp-6-3535-2006, 2006.
- Kasai, Y., Sagawa, H., Kreyling, D., Dupuy, E., Baron, P., Mendrok, J., Suzuki, K., Sato, T. O., Nishibori, T., Mizobuchi, S., Kikuchi, K., Manabe, T., Ozeki, H., Sugita, T., Fujiwara, M., Irimajiri, Y., Walker, K. A., Bernath, P. F., Boone, C., Stiller, G., von Clarmann, T., Orphal, J., Urban, J., Murtagh, D., Llewellyn, E. J., Degenstein, D., Bourassa, A. E., Lloyd, N. D., Froidevaux, L., Birk, M., Wagner, G., Schreier, F., Xu, J., Vogt, P., Trautmann, T. and Yasui, M.: Validation of stratospheric and mesospheric ozone observed by SMILES from International Space Station, *Atmos. Meas. Tech.*, 6(9), 2311–2338, doi:10.5194/amt-6-2311-

2013, 2013.

- Kato, S., Kajii, Y., Akimoto, H., Bräunlich, M., Röckmann, T. and Brenninkmeijer, C. A. M.: Observed and modeled seasonal variation of  $^{13}\text{C}$ ,  $^{18}\text{O}$ , and  $^{14}\text{C}$  of atmospheric CO at Happo, a remote site in Japan, and a comparison with other records, *J. Geophys. Res. Atmos.*, 105(D7), 8891–8900, doi:10.1029/1999JD901144, 2000.
- Kawagucci, S., Tsunogai, U., Kudo, S., Nakagawa, F., Honda, H., Aoki, S., Nakazawa, T., Tsutsumi, M. and Gamo, T.: Long-term observation of mass-independent oxygen isotope anomaly in stratospheric CO<sub>2</sub>, *Atmos. Chem. Phys.*, 8(20), 6189–6197, doi:10.5194/acp-8-6189-2008, 2008.
- Keeling, C. D.: The concentration and isotopic abundances of atmospheric carbon dioxide in rural areas, *Geochim. Cosmochim. Acta*, 13(4), 322–334, doi:10.1016/0016-7037(58)90033-4, 1958.
- C. D. Keeling, S. C. Piper, R. B. Bacastow, M. Wahlen, T. P. Whorf, M. Heimann, and H. A. Meijer, Exchanges of atmospheric CO<sub>2</sub> and  $^{13}\text{CO}_2$  with the terrestrial biosphere and oceans from 1978 to 2000. I. Global aspects, SIO Reference Series, No. 01-06, Scripps Institution of Oceanography, San Diego, 88 pages, 2001.
- Khalil, M. A. K. and Rasmussen, R. A.: Carbon Monoxide in the Earth's Atmosphere: Increasing Trend, *Science*, 224(4644), 54–56, doi:10.1126/science.224.4644.54, 1984.
- Khalil, M. A. K. and Rasmussen, R. A.: Global decrease in atmospheric carbon monoxide concentration, *Nature*, 370(6491), 639–641, doi:10.1038/370639a0, 1994.
- Komhyr, W. D., Harris, T. B., Waterman, L. S., Chin, J. F. S. and Thoning, K. W.: Atmospheric carbon dioxide at Mauna Loa Observatory: 1. NOAA global monitoring for climatic change measurements with a nondispersive infrared analyzer, 1974–1985, *J. Geophys. Res. Atmos.*, 94(D6), 8533–8547, doi:10.1029/JD094iD06p08533, 1989.
- Kramer, H. J.: *Observation of the Earth and its Environment - Survey of Missions and Sensors*, 4th Editio., Springer Verlag., 2002.
- Krankowsky, D., Lämmerzahl, P. and Mauersberger, K.: Isotopic measurements of

- stratospheric ozone, *Geophys. Res. Lett.*, 27(17), 2593–2595, doi:10.1029/2000GL011812, 2000.
- Krankowsky, D., Lämmerzahl, P., Mauersberger, K., Janssen, C., Tuzson, B. and Röckmann, T.: Stratospheric ozone isotope fractionations derived from collected samples, *J. Geophys. Res.*, 112(D8), D08301, doi:10.1029/2006JD007855, 2007.
- Kyrölä, E., Tamminen, J., Leppelmeier, G. W., Sofieva, V., Hassinen, S., Bertaux, J. L., Hauchecorne, A., Dalaudier, F., Cot, C., Korablev, O., Fanton d'Andon, O., Barrot, G., Mangin, A., Théodore, B., Guirlet, M., Etanchaud, F., Snoeij, P., Koopman, R., Saavedra, L., Fraise, R., Fussen, D. and Vanhellefont, F.: GOMOS on Envisat: An overview, *Adv. Sp. Res.*, 33(7), 1020–1028, doi:10.1016/S0273-1177(03)00590-8, 2004.
- de Laat, A. T. J., Gloudemans, A. M. S., Schrijver, H., van den Broek, M. M. P., Meirink, J. F., Aben, I. and Krol, M.: Quantitative analysis of SCIAMACHY carbon monoxide total column measurements, *Geophys. Res. Lett.*, 33(7), L07807, doi:10.1029/2005GL025530, 2006.
- Lamarque, J.-F., Bond, T. C., Eyring, V., Granier, C., Heil, A., Klimont, Z., Lee, D., Liousse, C., Mieville, A., Owen, B., Schultz, M. G., Shindell, D., Smith, S. J., Stehfest, E., Van Aardenne, J., Cooper, O. R., Kainuma, M., Mahowald, N., McConnell, J. R., Naik, V., Riahi, K. and van Vuuren, D. P.: Historical (1850–2000) gridded anthropogenic and biomass burning emissions of reactive gases and aerosols: methodology and application, *Atmos. Chem. Phys.*, 10(15), 7017–7039, doi:10.5194/acp-10-7017-2010, 2010.
- Lämmerzahl, P.: Oxygen isotope composition of stratospheric carbon dioxide, *Geophys. Res. Lett.*, 29(12), 1582, doi:10.1029/2001GL014343, 2002.
- Lassey, K. R., Allan, W. and Fletcher, S. E. M.: Seasonal inter-relationships in atmospheric methane and companion  $\delta^{13}\text{C}$  values: Effects of sinks and sources, *Tellus, Ser. B Chem. Phys. Meteorol.*, 63(3), 287–301, doi:10.1111/j.1600-0889.2011.00535.x, 2011.
- Laštovička, J., Akmaev, R. A., Beig, G., Bremer, J., Emmert, J. T., Jacobi, C., Jarvis, M. J., Nedoluha, G., Portnyagin, Y. I. and Ulich, T.: Emerging pattern of global change in the upper atmosphere and ionosphere, *Ann. Geophys.*, 26(5), 1255–



1268, doi:10.5194/angeo-26-1255-2008, 2008.

- Lee, A. Y. T., Yung, Y. L., Cheng, B.-M., Bahou, M., Chung, C.-Y. and Lee, Y.-P.: Enhancement of Deuterated Ethane on Jupiter, *Astrophys. J.*, 551(1), L93–L96, doi:10.1086/319827, 2001.
- Liang, M.-C., Irion, F. W., Weibel, J. D., Miller, C. E., Blake, G. a. and Yung, Y. L.: Isotopic composition of stratospheric ozone, *J. Geophys. Res.*, 111(D2), D02302, doi:10.1029/2005JD006342, 2006.
- López-Puertas, M., López-Valverde, M. Á., Garcia, R. R. and Roble, R. G.: A review of CO<sub>2</sub> and CO abundances in the middle atmosphere, in *Atmospheric Science across the Stratopause*, vol. mixi, pp. 83–100., 2000.
- MacFarling Meure, C., Etheridge, D., Trudinger, C., Steele, P., Langenfelds, R., van Ommen, T., Smith, A. and Elkins, J.: Law Dome CO<sub>2</sub>, CH<sub>4</sub> and N<sub>2</sub>O ice core records extended to 2000 years BP, *Geophys. Res. Lett.*, 33(14), L14810, doi:10.1029/2006GL026152, 2006.
- Mak, J. E.: The seasonally varying isotopic composition of the sources of carbon monoxide at Barbados, West Indies, *J. Geophys. Res.*, 108(D20), 4635, doi:10.1029/2003JD003419, 2003.
- Manney, G. L., Daffer, W. H., Zawodny, J. M., Bernath, P. F., Hoppel, K. W., Walker, K. A., Knosp, B. W., Boone, C., Remsberg, E. E., Santee, M. L., Harvey, V. L., Pawson, S., Jackson, D. R., Deaver, L., McElroy, C. T., McLinden, C. A., Drummond, J. R., Pumphrey, H. C., Lambert, A., Schwartz, M. J., Froidevaux, L., McLeod, S., Takacs, L. L., Suarez, M. J., Trepte, C. R., Cuddy, D. C., Livesey, N. J., Harwood, R. S. and Waters, J. W.: Solar occultation satellite data and derived meteorological products: Sampling issues and comparisons with Aura Microwave Limb Sounder, *J. Geophys. Res.*, 112(D24), D24S50, doi:10.1029/2007JD008709, 2007.
- Mauersberger, K.: Ozone isotope measurements in the stratosphere, *Geophys. Res. Lett.*, 14(1), 80–83, doi:10.1029/GL014i001p00080, 1987.
- Mauersberger, K., Lämmerzahl, P. and Krankowsky, D.: Stratospheric ozone isotope enrichments-Revisited, *Geophys. Res. Lett.*, 28(16), 3155–3158, doi:10.1029/2001GL013439, 2001.
- Met Office: High and low pressure, [online] Available from:

<http://www.metoffice.gov.uk/learning/learn-about-the-weather/how-weather-works/highs-and-lows/pressure> (Accessed 1 May 2017), 2013.

- Michelsen, H. A., Manney, G. L., Gunson, M. R., Rinsland, C. P. and Zander, R.: Correlations of stratospheric abundances of CH<sub>4</sub> and N<sub>2</sub>O derived from ATMOS measurements, *Geophys. Res. Lett.*, 25(15), 2777–2780, doi:10.1029/98GL01977, 1998.
- Miller, C. E., Onorato, R. M., Liang, M.-C. and Yung, Y. L.: Extraordinary isotopic fractionation in ozone photolysis, *Geophys. Res. Lett.*, 32(14), doi:10.1029/2005GL023160, 2005.
- Minschwaner, K. and Manney, G. L.: Derived methane in the stratosphere and lower mesosphere from Aura Microwave Limb Sounder measurements of nitrous oxide, water vapor, and carbon monoxide, *J. Atmos. Chem.*, 71(4), 253–267, doi:10.1007/s10874-015-9299-z, 2014.
- Minschwaner, K., Salawitch, R. J. and McElroy, M. B.: Absorption of solar radiation by O<sub>2</sub>: Implications for O<sub>3</sub> and lifetimes of N<sub>2</sub>O, CFCI<sub>3</sub>, and CF<sub>2</sub>Cl<sub>2</sub>, *J. Geophys. Res.*, 98(D6), 10543, doi:10.1029/93JD00223, 1993.
- Mohn, J., Wolf, B., Toyoda, S., Lin, C.-T., Liang, M.-C., Brüggemann, N., Wissel, H., Steiker, A. E., Dyckmans, J., Szwec, L., Ostrom, N. E., Casciotti, K. L., Forbes, M., Gieseemann, A., Well, R., Doucett, R. R., Yarnes, C. T., Ridley, A. R., Kaiser, J. and Yoshida, N.: Interlaboratory assessment of nitrous oxide isotopomer analysis by isotope ratio mass spectrometry and laser spectroscopy: current status and perspectives, *Rapid Commun. Mass Spectrom.*, 28(18), 1995–2007, doi:10.1002/rcm.6982, 2014.
- Myhre, G., Shindell, D., Bréon, F.-M., Collins, W., Fuglestvedt, J., Huang, J., Koch, D., Lamarque, J.-F., Lee, D., Mendoza, B., Nakajima, T., Robock, A., Stephens, G., Takemura, T. and Zhang, H.: Anthropogenic and Natural Radiative Forcing, in *Climate Change 2013: The Physical Science Basis*, edited by T. F. Stocker, D. Qin, G.-K. Plattner, M. Tignor, S. K. Allen, J. Boschung, A. Nauels, Y. Xia, V. Bex, and P. M. Midgley, pp. 659–740, Cambridge University Press, Cambridge, United Kingdom., 2013.
- Nair, H., Summers, M., Miller, C. and Yung, Y.: Isotopic fractionation of methane in the martian atmosphere, *Icarus*, 175(1), 32–35,

doi:10.1016/j.icarus.2004.10.018, 2005.

NASA: Studying Earth's Environment From Space, Stratospheric Ozone An Electronic Textbook. [online] Available from:

<http://www.ccpo.odu.edu/SEES/index.html> (Accessed 1 January 2017), 2000.

Neale, R. B., Gettelman, A., Park, S., Chen, C., Lauritzen, P. H., Williamson, D. L., Conley, A. J., Kinnison, D., Marsh, D., Smith, A. K., Vitt, F., Garcia, R., Lamarque, J., Mills, M., Tilmes, S., Morrison, H., Cameron-Smith, P., Collins, W. D., Iacono, M. J., Easter, R. C., Liu, X., Ghan, S. J., Rasch, P. J. and Taylor, M. A: Description of the NCAR Community Atmosphere Model (CAM 5.0). NCAR Technical Notes., 2012.

Novelli, P. C., Masarie, K. A., Tans, P. P. and Lang, P. M.: Recent Changes in Atmospheric Carbon Monoxide, *Science*, 263(5153), 1587–1590, doi:10.1126/science.263.5153.1587, 1994.

Oberlander, E. a.: Trace gas measurements along the Trans-Siberian railroad: The TROICA 5 expedition, *J. Geophys. Res.*, 107(D14), 4206, doi:10.1029/2001JD000953, 2002.

Park, K., Wang, Z., Emmons, L. K. and Mak, J. E.: Variation of atmospheric CO,  $\delta^{13}\text{C}$ , and  $\delta^{18}\text{O}$  at high northern latitude during 2004-2009: Observations and model simulations, *J. Geophys. Res. Atmos.*, 120(20), 11,024-11,036, doi:10.1002/2015JD023191, 2015.

Park, M.: Seasonal variation of methane, water vapor, and nitrogen oxides near the tropopause: Satellite observations and model simulations, *J. Geophys. Res.*, 109(D3), D03302, doi:10.1029/2003JD003706, 2004a.

Park, S.: Measurements of N<sub>2</sub>O isotopologues in the stratosphere: Influence of transport on the apparent enrichment factors and the isotopologue fluxes to the troposphere, *J. Geophys. Res.*, 109(D1), D01305, doi:10.1029/2003JD003731, 2004b.

Payan, S., Camy-Peyret, C., Oelhaf, H., Wetzell, G., Maucher, G., Keim, C., Pirre, M., Huret, N., Engel, A., Volk, M. C., Kuellmann, H., Kuttippurath, J., Cortesi, U., Bianchini, G., Mencaraglia, F., Raspollini, P., Redaelli, G., Vigouroux, C., De Mazière, M., Mikuteit, S., Blumenstock, T., Velazco, V., Notholt, J., Mahieu, E., Duchatelet, P., Smale, D., Wood, S., Jones, N., Piccolo, C., Payne, V., Bracher,

- A., Glatthor, N., Stiller, G., Grunow, K., Jeseck, P., Te, Y. and Butz, A.: Validation of version-4.61 methane and nitrous oxide observed by MIPAS, *Atmos. Chem. Phys.*, 9(2), 413–442, doi:10.5194/acp-9-413-2009, 2009.
- Plieninger, J., von Clarmann, T., Stiller, G. P., Grabowski, U., Glatthor, N., Kellmann, S., Linden, A., Haenel, F., Kiefer, M., Höpfner, M., Laeng, A. and Lossow, S.: Methane and nitrous oxide retrievals from MIPAS-ENVISAT, *Atmos. Meas. Tech.*, 8(11), 4657–4670, doi:10.5194/amt-8-4657-2015, 2015.
- Prasad, S. S. and Zipf, E. C.: Atmospheric production of nitrous oxide from excited ozone and its potentially important implications for global change studies, *J. Geophys. Res.*, 113(D15), D15307, doi:10.1029/2007JD009447, 2008.
- Prather, M. J., Penner, J. E., Fuglestedt, J. S., Kurosawa, A., Lowe, J. A., Höhne, N., Jain, A. K., Andronova, N., Pinguelli, L., Pires de Campos, C., Raper, S. C. B., Skeie, R. B., Stott, P. A., van Aardenne, J. and Wagner, F.: Tracking uncertainties in the causal chain from human activities to climate, *Geophys. Res. Lett.*, 36(5), L05707, doi:10.1029/2008GL036474, 2009.
- Prather, M. J., Hsu, J., DeLuca, N. M., Jackman, C. H., Oman, L. D., Douglass, A. R., Fleming, E. L., Strahan, S. E., Steenrod, S. D., Søvdø, O. A., Isaksen, I. S. A., Froidevaux, L. and Funke, B.: Measuring and modeling the lifetime of nitrous oxide including its variability, *J. Geophys. Res. Atmos.*, 120(11), 5693–5705, doi:10.1002/2015JD023267, 2015.
- Ravishankara, A. R., Daniel, J. S. and Portmann, R. W.: Nitrous Oxide (N<sub>2</sub>O): The Dominant Ozone-Depleting Substance Emitted in the 21st Century, *Science*, 326(5949), 123–125, doi:10.1126/science.1176985, 2009.
- Remsberg, E. E.: Methane as a diagnostic tracer of changes in the Brewer–Dobson circulation of the stratosphere, *Atmos. Chem. Phys.*, 15(7), 3739–3754, doi:10.5194/acp-15-3739-2015, 2015.
- Ricaud, P., Alexandre, D., Barret, B., Le Flochmoën, E., Motte, E., Berthet, G., Lefèvre, F. and Murtagh, D.: Measurements of mid-stratospheric formaldehyde from the Odin/SMR instrument, *J. Quant. Spectrosc. Radiat. Transf.*, 107(1), 91–104, doi:10.1016/j.jqsrt.2007.01.058, 2007.
- Rice, A. L., Tyler, S. C., McCarthy, M. C., Boering, K. A. and Atlas, A.: Carbon and hydrogen isotopic compositions of stratospheric methane: 1. High-precision

- observations from the NASA ER-2 aircraft, *J. Geophys. Res.*, 108(D15), 4460, doi:10.1029/2002JD003042, 2003.
- Rigby, M., Manning, A. J. and Prinn, R. G.: The value of high-frequency, high-precision methane isotopologue measurements for source and sink estimation, *J. Geophys. Res. Atmos.*, 117(D12), doi:10.1029/2011JD017384, 2012.
- Roble, R. G. and Dickinson, R. E.: How will changes in carbon dioxide and methane modify the mean structure of the mesosphere and thermosphere?, *Geophys. Res. Lett.*, 16(12), 1441–1444, doi:10.1029/GL016i012p01441, 1989.
- Roche, A. E., Kumer, J. B., Nightingale, R. W., Mergenthaler, J. L., Ely, G. A., Bailey, P. L., Massie, S. T., Gille, J. C., Edwards, D. P., Gunson, M. R., Abrams, M. C., Toon, G. C., Webster, C. R., Traub, W. A., Jucks, K. W., Johnson, D. G., Murcray, D. G., Murcray, F. H., Goldman, A. and Zipf, E. C.: Validation of CH<sub>4</sub> and N<sub>2</sub>O measurements by the cryogenic limb array etalon spectrometer instrument on the Upper Atmosphere Research Satellite, *J. Geophys. Res. Atmos.*, 101(D6), 9679–9710, doi:10.1029/95JD03442, 1996.
- Röckmann, T. and Levin, I.: High-precision determination of the changing isotopic composition of atmospheric N<sub>2</sub>O from 1990 to 2002, *J. Geophys. Res.*, 110(D21), D21304, doi:10.1029/2005JD006066, 2005.
- Röckmann, T., Brenninkmeijer, C. A. M., Saueressig, G., Bergamaschi, P., Crowley, J. N., Fischer, H. and Crutzen, P. J.: Mass-Independent Oxygen Isotope Fractionation in Atmospheric CO as a Result of the Reaction CO + OH, *Science*, 281(5376), 544–546, doi:10.1126/science.281.5376.544, 1998.
- Röckmann, T., Kaiser, J., Brenninkmeijer, C. A. M., Crowley, J. N., Borchers, R., Brand, W. A. and Crutzen, P. J.: Isotopic enrichment of nitrous oxide (<sup>15</sup>N<sup>14</sup>NO, <sup>14</sup>N<sup>15</sup>NO, <sup>14</sup>N<sup>14</sup>N<sup>18</sup>O) in the stratosphere and in the laboratory, *J. Geophys. Res. Atmos.*, 106(D10), 10403–10410, doi:10.1029/2000JD900822, 2001a.
- Röckmann, T., Kaiser, J., Crowley, J. N., Brenninkmeijer, C. A. M. and Crutzen, P. J.: The origin of the anomalous or “mass-independent” oxygen isotope fractionation in tropospheric N<sub>2</sub>O, *Geophys. Res. Lett.*, 28(3), 503–506, doi:10.1029/2000GL012295, 2001b.
- Röckmann, T., Jöckel, P., Gros, V., Bräunlich, M., Possnert, G. and Brenninkmeijer, C. A. M.: Using <sup>14</sup>C, <sup>13</sup>C, <sup>18</sup>O and <sup>17</sup>O isotopic variations to provide insights into

- the high northern latitude surface CO inventory, *Atmos. Chem. Phys.*, 2(2), 147–159, doi:10.5194/acp-2-147-2002, 2002.
- Röckmann, T., Brass, M., Borchers, R. and Engel, A.: The isotopic composition of methane in the stratosphere: high-altitude balloon sample measurements, *Atmos. Chem. Phys.*, 11(24), 13287–13304, doi:10.5194/acp-11-13287-2011, 2011.
- Rothman, L. S., Jacquemart, D., Barbe, A., Chris Benner, D., Birk, M., Brown, L. R., Carleer, M. R., Chackerian, C., Chance, K., Coudert, L. H., Dana, V., Devi, V. M., Flaud, J.-M., Gamache, R. R., Goldman, A., Hartmann, J.-M., Jucks, K. W., Maki, A. G., Mandin, J.-Y., Massie, S. T., Orphal, J., Perrin, A., Rinsland, C. P., Smith, M. A. H., Tennyson, J., Tolchenov, R. N., Toth, R. A., Vander Auwera, J., Varanasi, P. and Wagner, G.: The HITRAN 2004 molecular spectroscopic database, *J. Quant. Spectrosc. Radiat. Transf.*, 96(2), 139–204, doi:10.1016/j.jqsrt.2004.10.008, 2005.
- Russell, J. M., Gordley, L. L., Park, J. H., Drayson, S. R., Hesketh, W. D., Cicerone, R. J., Tuck, A. F., Frederick, J. E., Harries, J. E. and Crutzen, P. J.: The Halogen Occultation Experiment, *J. Geophys. Res.*, 98(D6), 10777, doi:10.1029/93JD00799, 1993.
- Sander, S. P., Friedl, R. R., Golden, D. M., Kurylo, M. J., Moortgat, G. K., Wine, P. H., Ravishankara, a R., Kolb, C. E., Molina, M. J., Diego, S., Jolla, L., Huie, R. E. and Orkin, V. L.: Chemical Kinetics and Photochemical Data for Use in Atmospheric Studies Evaluation Number 15, JPL Publ., 6–2(Eval. 15) [online] Available from: <http://jpldataeval.jpl.nasa.gov/>, 2006.
- Saueressig, G., Crowley, J. N., Bergamaschi, P., Brühl, C., Brenninkmeijer, C. A. M. and Fischer, H.: Carbon 13 and D kinetic isotope effects in the reactions of CH<sub>4</sub> with O(<sup>1</sup>D) and OH: New laboratory measurements and their implications for the isotopic composition of stratospheric methane, *J. Geophys. Res.*, 106(D19), 23127, doi:10.1029/2000JD000120, 2001.
- Schmidt, J. A., Johnson, M. S. and Schinke, R.: Carbon dioxide photolysis from 150 to 210 nm: singlet and triplet channel dynamics, UV-spectrum, and isotope effects., *Proc. Natl. Acad. Sci. U. S. A.*, 110(44), 17691–6, doi:10.1073/pnas.1213083110, 2013.

- Schmidt, J. A., Johnson, M. S. and Schinke, R.: Isotope effects in N<sub>2</sub>O photolysis from first principles, *Atmos. Chem. Phys.*, 11(17), 8965–8975, doi:10.5194/acp-11-8965-2011, 2011.
- Schneising, O., Buchwitz, M., Burrows, J. P., Bovensmann, H., Bergamaschi, P. and Peters, W.: Three years of greenhouse gas column-averaged dry air mole fractions retrieved from satellite – Part 2: Methane, *Atmos. Chem. Phys.*, 9(2), 443–465, doi:10.5194/acp-9-443-2009, 2009.
- Schoeberl, M. R., Douglass, A. R., Hilsenrath, E., Bhartia, P. K., Beer, R., Waters, J. W., Gunson, M. R., Froidevaux, L., Gille, J. C., Barnett, J. J., Levelt, P. F. and DeCola, P.: Overview of the EOS-Aura mission, *IEEE Trans. Geosci. Remote Sens.*, 44(5), 1066–1072, doi:10.1109/TGRS.2005.861950, 2006.
- Semeniuk, K., McConnell, J. C., Jin, J. J., Jarosz, J. R., Boone, C. D. and Bernath, P. F.: N<sub>2</sub>O production by high energy auroral electron precipitation, *J. Geophys. Res.*, 113(D16), D16302, doi:10.1029/2007JD009690, 2008.
- Shaheen, R., Janssen, C. and Röckmann, T.: Investigations of the photochemical isotope equilibrium between O<sub>2</sub>, CO<sub>2</sub> and O<sub>3</sub>, *Atmos. Chem. Phys.*, 7(2), 495–509, doi:10.5194/acp-7-495-2007, 2007.
- Sheese, P. E., Boone, C. D. and Walker, K. A.: Detecting physically unrealistic outliers in ACE-FTS atmospheric measurements, *Atmos. Meas. Tech.*, 8(2), 741–750, doi:10.5194/amt-8-741-2015, 2015.
- Sheese, P. E., Walker, K. A., Boone, C. D., Bernath, P. F. and Funke, B.: Nitrous oxide in the atmosphere: First measurements of a lower thermospheric source, *Geophys. Res. Lett.*, 43(6), 2866–2872, doi:10.1002/2015GL067353, 2016.
- Shine, K. P., Derwent, R. G., Wuebbles, D. J. and Morcrette, J. J.: Radiative Forcing of Climate, in *Climate Change: The IPCC Scientific Assessment*, edited by J. T. Houghton, G. J. Jenkins, and J. J. Ephraums, pp. 41–68, Cambridge University Press, Cambridge, United Kingdom., 1990.
- Slater, C., Preston, T. and Weaver, L. T.: Stable isotopes and the international system of units., *Rapid Commun. Mass Spectrom.*, 15(15), 1270–3, doi:10.1002/rcm.328, 2001.
- Snider, D. M., Venkiteswaran, J. J., Schiff, S. L. and Spoelstra, J.: From the Ground Up: Global Nitrous Oxide Sources are Constrained by Stable Isotope Values,

- edited by S. Hu, PLoS One, 10(3), e0118954,  
doi:10.1371/journal.pone.0118954, 2015.
- Stark, H. R., Möller, H. L., Courrèges-lacoste, G. B., Koopman, R. and Veihelmann, B.: the Sentinel-4 Mission and Its Implementation, [online] Available from: [http://www.eumetsat.int/website/wcm/idc/idcplg?IdcService=GET\\_FILE&dDocName=PDF\\_CONF\\_P\\_S1\\_10\\_STARK\\_V&RevisionSelectionMethod=LatestReleased&Rendition=Web](http://www.eumetsat.int/website/wcm/idc/idcplg?IdcService=GET_FILE&dDocName=PDF_CONF_P_S1_10_STARK_V&RevisionSelectionMethod=LatestReleased&Rendition=Web), 2013.
- Stevens, C. M. and Krout, L.: Method for the determination of the concentration and of the carbon and oxygen isotopic composition of atmospheric carbon monoxide, *Int. J. Mass Spectrom. Ion Phys.*, 8(4), 265–275, doi:10.1016/0020-7381(72)83017-1, 1972.
- Sugawara, S., Nakazawa, T., Shirakawa, Y., Kawamura, K., Aoki, S., Machida, T. and Honda, H.: Vertical profile of the carbon isotopic ratio of stratospheric methane over Japan, *Geophys. Res. Lett.*, 24(23), 2989–2992, doi:10.1029/97GL03044, 1997.
- Sutka, R. L., Ostrom, N. E., Ostrom, P. H., Breznak, J. A., Gandhi, H., Pitt, A. J. and Li, F.: Distinguishing Nitrous Oxide Production from Nitrification and Denitrification on the Basis of Isotopomer Abundances, *Appl. Environ. Microbiol.*, 72(1), 638–644, doi:10.1128/AEM.72.1.638-644.2006, 2006.
- Tarasova, O. A., Brenninkmeijer, C. A. M., Assonov, S. S., Elansky, N. F., Röckmann, T. and Sofiev, M. A.: Atmospheric CO along the Trans-Siberian Railroad and River Ob: source identification using isotope analysis, *J. Atmos. Chem.*, 57(2), 135–152, doi:10.1007/s10874-007-9066-x, 2007.
- Terao, Y., Mukai, H., Nojiri, Y., Machida, T., Tohjima, Y., Saeki, T. and Maksyutov, S.: Interannual variability and trends in atmospheric methane over the western Pacific from 1994 to 2010, *J. Geophys. Res. Atmos.*, 116(14), 1–13, doi:10.1029/2010JD015467, 2011.
- Thiemens, M. H. and Heidenreich, J. E.: The Mass-Independent Fractionation of Oxygen: A Novel Isotope Effect and Its Possible Cosmochemical Implications, *Science*, 219(4588), 1073–1075, doi:10.1126/science.219.4588.1073, 1983.
- Thiemens, M. H., Jackson, T., Mauersberger, K., Schueler, B. and Morton, J.: Oxygen isotope fractionation in stratospheric CO<sub>2</sub>, *Geophys. Res. Lett.*, 18(4),



- 669–672, doi:10.1029/91GL00121, 1991.
- Thiemens, M. H., Jackson, T., Zipf, E. C., Erdman, P. W. and van Egmond, C.: Carbon Dioxide and Oxygen Isotope Anomalies in the Mesosphere and Stratosphere, *Science*, 270(5238), 969–972, doi:10.1126/science.270.5238.969, 1995.
- Toyoda, S.: Temporal and latitudinal distributions of stratospheric N<sub>2</sub>O isotopomers, *J. Geophys. Res.*, 109(D8), D08308, doi:10.1029/2003JD004316, 2004.
- Toyoda, S., Yoshida, N., Urabe, T., Aoki, S., Nakazawa, T., Sugawara, S. and Honda, H.: Fractionation of N<sub>2</sub>O isotopomers in the stratosphere, *J. Geophys. Res.*, 106(D7), 7515, doi:10.1029/2000JD900680, 2001.
- Toyoda, S., Kuroki, N., Yoshida, N., Ishijima, K., Tohjima, Y. and Machida, T.: Decadal time series of tropospheric abundance of N<sub>2</sub>O isotopomers and isotopologues in the Northern Hemisphere obtained by the long-term observation at Hateruma Island, Japan, *J. Geophys. Res. Atmos.*, 118(8), 3369–3381, doi:10.1002/jgrd.50221, 2013.
- Umezawa, T., Machida, T., Ishijima, K., Matsueda, H., Sawa, Y., Patra, P. K., Aoki, S. and Nakazawa, T.: Carbon and hydrogen isotopic ratios of atmospheric methane in the upper troposphere over the Western Pacific, *Atmos. Chem. Phys.*, 12, 8095–81113, doi:10.5194/acp-12-8095-2012, 2012.
- Vigouroux, C., Hendrick, F., Stavrakou, T., Dils, B., De Smedt, I., Hermans, C., Merlaud, A., Scolas, F., Senten, C., Vanhaelewyn, G., Fally, S., Carleer, M., Metzger, J.-M., Müller, J.-F., Van Roozendaal, M. and De Mazière, M.: Ground-based FTIR and MAX-DOAS observations of formaldehyde at Réunion Island and comparisons with satellite and model data, *Atmos. Chem. Phys.*, 9(24), 9523–9544, doi:10.5194/acp-9-9523-2009, 2009.
- Vincent, R. A.: The dynamics of the mesosphere and lower thermosphere: a brief review, *Prog. Earth Planet. Sci.*, 2(1), 4, doi:10.1186/s40645-015-0035-8, 2015.
- Walkty, I. and Kohut, K.: SCISAT-1 Spacecraft, in *The Atmospheric Chemistry Experiment: ACE at 10*, edited by P. F. Bernath, pp. 43–52, A. Deepak Publishing, Hampton, VA., 2013.
- Washington, W. M., Buja, L. and Craig, A.: The computational future for climate and

- Earth system models: on the path to petaflop and beyond, *Philos. Trans. R. Soc. A Math. Phys. Eng. Sci.*, 367(1890), 833–846, doi:10.1098/rsta.2008.0219, 2009.
- Wecht, K. J., Jacob, D. J., Wofsy, S. C., Kort, E. a., Worden, J. R., Kulawik, S. S., Henze, D. K., Kopacz, M. and Payne, V. H.: Validation of TES methane with HIPPO aircraft observations: implications for inverse modeling of methane sources, *Atmos. Chem. Phys.*, 12(4), 1823–1832, doi:10.5194/acp-12-1823-2012, 2012.
- Wiegel, A. A., Cole, A. S., Hoag, K. J., Atlas, E. L., Schauffler, S. M. and Boering, K. A.: Unexpected variations in the triple oxygen isotope composition of stratospheric carbon dioxide, *Proc. Natl. Acad. Sci.*, 110(44), 17680–17685, doi:10.1073/pnas.1213082110, 2013.
- Wild, O. and Prather, M. J.: Excitation of the primary tropospheric chemical mode in a global three-dimensional model, *J. Geophys. Res.*, 105(D20), 24647, doi:10.1029/2000JD900399, 2000.
- Xiong, X., Barnet, C., Maddy, E. S., Gambacorta, A., King, T. S. and Wofsy, S. C.: Mid-upper tropospheric methane retrieval from IASI and its validation, *Atmos. Meas. Tech.*, 6(9), 2255–2265, doi:10.5194/amt-6-2255-2013, 2013.
- Xiong, X., Maddy, E. S., Barnet, C., Gambacorta, A., Patra, P. K., Sun, F. and Goldberg, M.: Retrieval of nitrous oxide from Atmospheric Infrared Sounder: Characterization and validation, *J. Geophys. Res. Atmos.*, 119(14), 9107–9122, doi:10.1002/2013JD021406, 2014.
- Yokota, T., Yoshida, Y., Eguchi, N., Ota, Y., Tanaka, T., Watanabe, H. and Maksyutov, S.: Global Concentrations of CO<sub>2</sub> and CH<sub>4</sub> Retrieved from GOSAT: First Preliminary Results, *Sci. Online Lett. Atmos.*, 5, 160–163, doi:10.2151/sola.2009-041, 2009.
- Yoshida, N. and Toyoda, S.: Constraining the atmospheric N<sub>2</sub>O budget from the intramolecular site preference in N<sub>2</sub>O isotopomers, *Nature*, 405(6784), 330–334, doi:10.1038/35012558, 2000.
- Yoshino, K., Esmond, J. R., Sun, Y., Parkinson, W. H., Ito, K. and Matsui, T.: Absorption cross section measurements of carbon dioxide in the wavelength

- region 118.7–175.5 nm and the temperature dependence, *J. Quant. Spectrosc. Radiat. Transf.*, 55(1), 53–60, doi:10.1016/0022-4073(95)00135-2, 1996.
- Yung, Y. L. and Miller, C. E.: Isotopic Fractionation of Stratospheric Nitrous Oxide, *Science*, 278(5344), 1778–1780, doi:10.1126/science.278.5344.1778, 1997.
- Yung, Y. L., DeMore, W. B. and Pinto, J. P.: Isotopic exchange between carbon dioxide and ozone via O(<sup>1</sup>D) in the stratosphere, *Geophys. Res. Lett.*, 18(1), 13–16, doi:10.1029/90GL02478, 1991.
- Yung, Y. L., Lee, A. Y. T., Demore, B. and Wen, J.: Carbon dioxide in the atmosphere : Isotopic exchange with ozone and its use as a tracer in the middle atmosphere, *J. Geophys. Res.*, 102(1), 857–866, doi:10.1029/97JD00528, 1997.
- Zipf, E. C. and Prasad, S. S.: A mesospheric source of nitrous oxide, *Nature*, 295(5845), 133–135, doi:10.1038/295133a0, 1982.

## APPENDIX

Table 13: Microwindow list for CH<sub>4</sub>

Center Frequency (cm <sup>-1</sup> )	Microwindow Width (cm <sup>-1</sup> )	Lower Altitude (km)	Upper Altitude (km)
1245.14	0.35	40	55
1270.70	0.35	40	60
1283.55	0.4	45	75
1287.80	0.4	55	75
1302.10	0.4	45	75
1302.85	0.4	45	75
1303.65	0.4	45	75
1311.40	0.45	50	75
1316.85	0.5	45	75
1322.15	0.5	45	75
1327.25	0.7	40	75
1332.40	0.9	40	75
1341.80	0.6	40	75
1342.80	0.6	45	75
1364.65	0.4	30	45
1439.43	0.35	15	25
1672.42	0.3	35	45
1876.62	0.35	15	35
2610.20	0.35	10	25
2614.02	0.65	10	30
2614.85	0.5	20	30
2618.27	0.35	25	40
2620.84	0.5	10	20
2644.72	0.35	15	30
2650.67	0.4	5	20
2652.95	0.3	5	20
2653.85	0.4	5	20
2658.65	0.35	10	20
2664.50	0.35	15	30
2667.19	0.3	15	30
2667.85	0.45	5	20
2669.27	0.55	5	20
2670.28	0.4	5	20
2671.60	0.3	5	20

Table 13 Continued

Center Frequency ( $\text{cm}^{-1}$ )	Microwindow Width ( $\text{cm}^{-1}$ )	Lower Altitude (km)	Upper Altitude (km)
2698.90	0.3	5	15
2700.28	0.35	5	15
2809.02	0.3	25	40
2820.80	0.35	25	40
2822.69	0.3	30	45
2825.05	0.3	30	40
2828.17	0.4	30	45
2835.61	0.35	20	30
2841.22	0.35	15	30
2847.73	0.35	30	45
2849.25	0.4	25	35
2857.50	0.35	15	25
2861.00	0.45	13	22
2867.10	0.4	30	40
2900.10	0.26	35	45
2958.13	0.45	50	75
2978.83	0.6	55	75
2988.92	0.5	50	75
3028.70	0.5	55	75
3038.50	0.4	65	75
3048.15	0.4	60	75
3057.70	0.45	65	75
3067.30	0.45	65	75
3076.63	0.45	55	75
3085.97	0.6	55	75

Table 14: Microwindow list for  $\text{CH}_3\text{D}$ 

Center Frequency ( $\text{cm}^{-1}$ )	Microwindow Width ( $\text{cm}^{-1}$ )	Lower Altitude (km)	Upper Altitude (km)
923.16	0.8	6	22
1109.60	0.5	6	15
1113.88	0.4	6	20
1118.97	0.5	6	22
1122.90	0.4	6	20
1123.50	0.4	6	15
1126.60	0.4	6	20
1130.84	0.4	6	20
1134.80	0.35	8	20

Table 14 Continued

Center Frequency ( $\text{cm}^{-1}$ )	Microwindow Width ( $\text{cm}^{-1}$ )	Lower Altitude (km)	Upper Altitude (km)
1139.15	0.4	6	20
1143.35	0.35	6	20
1157.77	0.3	6	15
1159.39	0.28	6	12
1167.95	0.4	6	15
1171.90	0.32	5-8	15
1176.99	0.3	10	20
1181.34	0.26	5-8	15
1183.15	0.3	6	15
1188.70	0.4	6	25
1194.45	0.3	6	12
1200.22	0.6	5-8	20
1201.99	0.35	6	22
1204.38	0.3	6	20
1206.90	0.3	5-9	20
1231.13	0.3	6	25
1231.37	0.5	6	25
1480.25	0.5	10-14	22
1950.10	0.35	6	20
1950.70	0.5	20	30-35
1986.09	0.3	6-7	22
2623.87	0.9	6-7	10-14
2950.70	0.5	20	30-35
2972.20	0.5	25	30-35
2972.40	0.4	10	25
2980.30	0.4	25	30-35
2987.93	0.55	17	30-35
3061.30	0.6	20	30-35
3063.35	0.4	12	30-35
3069.05	0.5	25	30-35
3072.66	0.6	15	30-35
3082.00	0.6	15	30-35
3083.80	0.4	30	30-35
3089.60	0.45	25	30-35
3091.30	0.55	25	30-35
3096.95	0.4	20	30-35

Table 15: Microwindow list for  $^{13}\text{CH}_4$ 

Center Frequency ( $\text{cm}^{-1}$ )	Microwindow Width ( $\text{cm}^{-1}$ )	Lower Altitude (km)	Upper Altitude (km)
1202.85	0.6	7	20
1219.17	0.35	12	25
1231.37	0.45	5	35
1234.25	0.5	5	35
1234.50	1.6	10	25-40
1235.05	0.3	15	30
1239.12	0.35	15	30
1244.43	0.35	15	25
1260.70	0.5	30	50
1263.40	0.4	40	50
1274.15	0.4	25	40
1275.55	0.6	40	50
1275.90	0.4	25	40
1280.20	0.4	25	50
1294.30	0.4	30	50
1295.85	0.3	25	50
1298.15	0.4	30	50
1318.80	0.6	35	50
1324.05	0.6	35	50
1329.43	1.1	35	50
1332.90	0.6	35	50
1334.10	0.6	20	50
1338.50	0.6	35	50
1339.17	0.55	17	30
1950.70	0.5	19-25	34-45
2566.22	0.26	7	22
2617.51	0.3	5-8	20
2623.87	0.9	5-7	20
2688.80	0.4	5	20
2700.00	0.45	5	15
2703.33	0.35	5	20
2733.10	0.6	5-8	25
2748.47	0.35	5	25
2817.50	0.3	5	25
2896.55	0.3	15	30
2938.90	0.4	15	30

Table 16: Microwindow list for CO

Center Frequency ( $\text{cm}^{-1}$ )	Microwindow Width ( $\text{cm}^{-1}$ )	Lower Altitude (km)	Upper Altitude (km)
1950.10	0.35	7	15
1986.09	0.3	6-7	22
2033.08	0.3	5	8
2046.29	0.24	8	25
2050.90	0.3	20	45
2081.88	0.48	13-15	100
2083.05	0.7	5	15
2086.36	0.4	15	100
2094.76	0.4	70	110
2098.97	0.5	40	110
2107.46	0.4	60	110
2115.50	0.6	40	110
2119.70	0.5	70	110
2131.65	0.5	18	105
2135.40	1	14-16	105
2139.35	1	13-15	105
2140.00	1.25	5	22
2140.80	0.6	5	22
2146.75	1	5	22
2147.05	0.9	13-15	105
2149.75	0.6	5	15
2150.90	0.7	16-17	105
2154.65	0.8	17-18	110
2158.30	0.5	19	110
2161.95	0.5	20	110
2164.00	0.5	10	20
2165.48	0.55	20	110
2169.13	0.55	20	110
2172.68	0.5	50	110
2176.25	0.45	20	110
2179.85	0.4	60	110
2183.20	0.4	40	110
2186.60	0.4	60	110
4209.38	0.4	5	15
4222.90	0.45	5	15
4227.37	0.7	5	15
4236.01	0.45	5	15
4248.34	0.4	5	15
4274.77	0.3	5	15
4285.10	0.55	5	15



Table 17: Microwindow list for  $^{13}\text{CO}$ 

Center Frequency ( $\text{cm}^{-1}$ )	Microwindow Width ( $\text{cm}^{-1}$ )	Lower Altitude (km)	Upper Altitude (km)
1446.5	0.35	30	50
1649.34	0.3	20	30
1950.1	0.35	5-7	20
1977.66	0.6	5-7	22
1986.09	0.3	5-7	22
2020.9	0.4	5-8	12
2024.9	0.4	5	12
2033.37	0.3	5	15
2045.67	0.35	12	20
2045.9	0.4	50	85
2049.42	1	50	85
2049.92	0.4	12	50
2053.74	0.4	50	85
2057.8	0.3	15	50
2058.05	0.5	50	90
2061.57	0.7	50	90
2061.87	0.35	12	50
2065.82	0.4	50	90
2069.6	0.26	20	90
2073.38	0.55	50	90
2077.45	0.5	60	90
2081.6	1	45	90
2084.98	0.4	10	90
2088.77	0.4	45	90
2092.43	0.3	12	20
2103.32	0.4	45	90
2107.15	0.7	55	90
2111	1.25	50	90
2113.95	0.4	50	90
2117.35	0.35	55	90
2120.9	0.35	55	90
2124	0.8	60	90
2127.65	0.3	60	90
2131.34	1	40	90
2134.35	0.35	45	90
2137.6	0.3	5-9	85
2140.8	0.6	5	40
2144.1	0.4	5	45
2147.1	0.4	20	40
2153.28	0.45	5	12
2159.6	0.4	5-7	12

Table 18: Microwindow list for CO<sub>2</sub>

Center Frequency (cm <sup>-1</sup> )	Microwindow Width (cm <sup>-1</sup> )	Lower Altitude (km)	Upper Altitude (km)
927.00	0.35	30	45
929.00	0.35	30	45
931.00	0.35	30	45
932.96	0.30	25	45
934.82	0.45	15	45
936.80	0.35	15	45
940.52	0.80	15	45
942.40	0.35	15	45
946.00	0.35	20	45
947.70	0.40	20	45
1899.17	0.30	30	58
1902.05	0.30	30	60
1905.16	0.40	35	45
1905.26	0.22	25	35
1906.48	0.30	30	65
1911.02	0.35	35	68
1911.12	0.30	30	35
1912.52	0.35	45	68
1914.12	0.30	30	70
1915.48	0.30	30	70
1917.06	0.35	30	70
1920.11	0.35	30	70
1924.71	0.35	40	65
1929.45	0.30	25	45
1930.90	0.27	15	45
1933.98	0.24	25	60
1934.78	0.24	22	45
1935.24	0.28	15	50
1936.44	0.30	25	50
1941.03	0.35	15	45
1950.68	0.30	15	45
1962.08	0.30	35	45
1968.64	0.30	35	45
1970.12	0.30	20	45
1975.10	0.30	15	40
2044.50	0.30	50	70
2045.97	0.30	53	73
2047.53	0.40	55	73
2049.05	0.40	53	75

Table 18 Continued

Center Frequency ( $\text{cm}^{-1}$ )	Microwindow Width ( $\text{cm}^{-1}$ )	Lower Altitude (km)	Upper Altitude (km)
2050.55	0.40	55	78
2052.10	0.30	50	79
2053.66	0.30	55	80
2055.11	0.35	60	80
2056.72	0.30	55	85
2058.24	0.40	55	85
2061.33	0.35	60	85
2062.87	0.35	60	85
2066.03	0.35	60	85
2067.52	0.35	60	83
2070.65	0.40	62	80
2072.23	0.30	57	80
2289.20	0.35	105	125
2291.50	0.30	110	125
2293.90	0.35	78	125
2296.06	0.30	110	125
2298.24	0.30	105	125
2300.40	0.30	90	125
2306.85	0.30	95	125
2313.10	0.35	95	125
2319.14	0.26	90	125
2332.37	0.30	95	125
2354.37	0.26	90	125
2361.45	0.30	90	125
2364.10	0.30	90	125
2366.63	0.30	90	125
2367.88	0.30	90	125
2369.10	0.30	90	125
2370.27	0.35	90	125
2371.43	0.30	90	125
2372.56	0.30	90	125
2373.67	0.35	90	125
2374.23	0.28	50	65
2374.75	0.40	90	125
2375.40	0.28	50	60
2375.80	0.35	90	125
2376.84	0.35	90	125
2377.85	0.35	90	125
2378.83	0.35	75	125

Table 18 Continued

Center Frequency ( $\text{cm}^{-1}$ )	Microwindow Width ( $\text{cm}^{-1}$ )	Lower Altitude (km)	Upper Altitude (km)
2379.78	0.35	90	125
2380.72	0.35	85	125
2381.62	0.35	85	125
2382.48	0.40	82	125
2383.36	0.35	82	125
2384.20	0.35	90	125
2385.02	0.40	75	125
2385.79	0.35	73	125
2386.51	0.35	70	125
2387.26	0.35	65	125
2387.96	0.35	60	80
2388.64	0.35	55	77
2389.29	0.35	50	71
2389.92	0.30	35	68
2390.52	0.35	35	65
2391.13	0.30	22	62
2391.70	0.30	22	60
2392.10	0.30	20	55
2392.62	0.30	20	50
2393.06	0.30	20	50
2399.05	0.24	20	40
2403.00	0.26	20	40
2408.77	0.20	15	46
2412.47	0.30	30	46
2419.60	0.30	35	45
2421.19	0.30	15	46
2422.88	0.30	15	46
2424.60	0.30	25	45
2433.12	0.30	30	40
2434.56	0.28	30	45
2439.00	0.30	35	46
2444.27	0.24	35	46

Table 19: Microwindow list for OC<sup>18</sup>O

Center Frequency (cm <sup>-1</sup> )	Microwindow Width (cm <sup>-1</sup> )	Lower Altitude (km)	Upper Altitude (km)
1371.80	0.3	15	45
1372.52	0.3	20	45
1376.20	0.3	25	45
1379.25	0.3	15	45
1380.70	0.35	15	45
1383.65	0.4	17	45
1384.42	0.45	15	45
1385.28	0.45	30	45
1385.90	0.35	15	45
1950.10	0.35	5-7	21
2276.62	0.3	35	60
2281.08	0.4	35	60
2283.11	0.26	25	40
2283.17	0.4	35	60
2285.15	0.4	35	65
2287.78	0.4	40	60
2292.35	0.75	40	65
2307.63	0.4	55	95
2314.68	0.35	50	95
2316.25	0.4	90	105
2318.85	0.4	90	105
2319.74	0.4	90	105
2320.52	0.3	50	105
2337.05	0.5	55	95
2338.50	0.3	95	105
2340.20	0.3	45	60
2340.50	0.3	60	105
2341.85	0.4	75	105
2342.60	0.5	95	105
2343.08	0.35	60	105
2343.60	0.6	95	105
2344.90	0.35	90	105
2345.55	0.4	60	105
2346.87	0.35	60	105
2348.00	0.4	45	100
2349.30	0.35	45	100
2353.60	0.4	60	95
2354.82	0.3	60	90
2355.22	0.3	60	85

Table 19 Continued

Center Frequency ( $\text{cm}^{-1}$ )	Microwindow Width ( $\text{cm}^{-1}$ )	Lower Altitude (km)	Upper Altitude (km)
2356.37	0.3	60	85
2356.68	0.35	45	85
2357.83	0.3	60	85
2359.45	0.6	60	85
2360.59	0.3	60	80
2604.50	0.8	5	40
2609.80	0.45	5	40
2610.73	0.7	5	35
2611.34	0.4	5	35
2617.20	0.4	5	35
2620.10	0.4	12	40
2620.82	0.4	5	40
2621.50	0.35	15	40
2623.75	0.3	15	40
2623.87	0.9	5	21
2624.45	0.4	15	40
2626.35	0.4	5	40
2627.35	0.5	5	40
2629.48	0.35	12	40
2636.63	0.35	5	35

Table 20: Microwindow list for  $\text{OC}^{17}\text{O}$ 

Center Frequency ( $\text{cm}^{-1}$ )	Microwindow Width ( $\text{cm}^{-1}$ )	Lower Altitude (km)	Upper Altitude (km)
2329.55	0.5	90	100
2329.77	0.45	75	90
2347.05	0.3	90	100
2347.19	0.3	50	90
2348.02	0.4	50	90
2348.13	0.5	90	100
2349.15	0.5	90	100
2349.32	0.35	50	90
2350.64	0.3	50	90
2350.8	0.5	90	100
2351.22	0.3	70	90
2351.38	0.35	90	100
2352.03	0.3	50	90
2352.12	0.45	90	100

Table 20 Continued

Center Frequency ( $\text{cm}^{-1}$ )	Microwindow Width ( $\text{cm}^{-1}$ )	Lower Altitude (km)	Upper Altitude (km)
2353.11	0.45	90	100
2353.25	0.3	60	90
2353.8	0.35	50	90
2354.03	0.45	90	100
2355.15	0.3	50	90
2355.28	0.45	90	100
2359.3	0.3	50	85
2362.09	0.3	50	80
2385.02	0.4	75	92

Table 21: Microwindow list for  $\text{N}_2\text{O}$ 

Center Frequency ( $\text{cm}^{-1}$ )	Microwindow Width ( $\text{cm}^{-1}$ )	Lower Altitude (km)	Upper Altitude (km)
829.03	0.5	5	25
1134.42	0.6	5	20
1139.78	0.6	5	20
1161.57	0.45	20	30
1163.23	0.55	20	30
1164.08	0.5	20	30
1167.93	0.4	5	15
1168.83	0.6	5	25
1169.74	0.5	15	25
1178.25	0.5	20	30
1180.85	0.6	20	30
1181.75	0.4	20	30
1182.60	0.4	20	30
1183.57	0.55	20	30
1186.05	0.5	20	30
1187.90	0.4	20	30
1194.10	0.5	15	25
1195.80	0.4	15	25
1202.05	0.35	5	15
1202.85	0.6	5	20
1203.86	0.8	5	20
1204.70	0.5	5	21
1228.00	0.4	5	20
1264.68	0.35	30	40
1266.65	0.4	30	40

Table 21 Continued

Center Frequency ( $\text{cm}^{-1}$ )	Microwindow Width ( $\text{cm}^{-1}$ )	Lower Altitude (km)	Upper Altitude (km)
1270.10	0.5	30	40
1271.11	0.3	30	40
1272.80	0.4	30	40
1273.77	0.35	30	40
1274.55	0.4	30	40
1277.15	0.4	30	40
1354.15	0.45	20	30
1950.10	0.35	8-10	20
1977.60	0.5	5	21
2140.18	0.35	10	20
2195.00	0.35	20	35
2201.78	0.35	35	50
2203.25	1.2	53	95
2203.66	0.55	35	50
2205.65	0.4	35	53
2208.50	0.4	40	53
2209.05	1.2	53	95
2210.00	1.2	53	95
2210.50	0.45	35	53
2211.50	0.5	35	53
2212.75	1.2	53	95
2214.07	0.45	35	53
2215.20	0.4	40	53
2215.35	0.9	53	95
2216.29	1.25	53	95
2221.23	0.4	30	40
2230.50	0.9	53	70
2231.27	1.2	53	70
2232.90	1.2	53	80
2234.95	0.6	53	95
2235.67	1.2	65	95
2236.27	0.4	40	53
2236.75	1.2	53	95
2237.82	1.2	53	95
2239.20	0.6	53	95
2239.93	1.2	53	95
2241.25	0.8	53	88
2241.97	1.2	53	88
2525.25	0.4	5-7	20
2566.22	0.26	5	10
2623.87	0.9	5	21



Table 22: Microwindow list for N<sup>15</sup>NO (<sup>15</sup>N<sup>0</sup>)

Center Frequency (cm <sup>-1</sup> )	Microwindow Width (cm <sup>-1</sup> )	Lower Altitude (km)	Upper Altitude (km)
933.90	0.3	7	22
1950.10	0.35	5-8	20
2140.24	0.5	10	25
2141.15	0.3	5	25
2143.30	0.6	5	25
2144.25	0.7	8	30
2146.48	0.4	5	35
2148.12	0.65	10	20
2149.70	0.3	10	35
2153.74	0.4	10	35
2155.73	0.45	10	35
2156.70	0.5	20	35
2157.25	0.3	8	20
2158.05	0.9	35	42-45
2158.48	0.6	35	42-45
2159.60	0.45	35	42-45
2160.60	0.3	25	35
2161.70	0.8	35	42-45
2161.95	0.5	20	35
2162.28	0.8	35	42-45
2165.45	0.5	35	42-45
2166.00	1	35	42-45
2169.10	0.4	35	42-45
2169.55	0.9	35	42-45
2187.20	0.4	30	35
2189.10	1	35	42-45
2190.45	1.1	35	42-45
2190.84	0.35	15	35
2191.50	0.4	35	42-45
2192.40	0.4	35	42-45
2193.08	0.35	20	35
2193.35	0.9	35	42-45
2195.40	0.9	35	42-45
2196.80	1	35	42-45
2513.70	0.4	9	20
2524.10	0.3	5-7	15
2527.32	0.4	5-8	20
2528.32	0.4	5-7	22
2543.80	0.35	5-7	20
2560.40	0.26	5	20
2566.22	0.26	5	20

Table 23: Microwindow list for  $^{15}\text{NNO}$  ( $^{15}\text{N}^{\beta}$ )

Center Frequency ( $\text{cm}^{-1}$ )	Microwindow Width ( $\text{cm}^{-1}$ )	Lower Altitude (km)	Upper Altitude (km)
1231.37	0.45	7-9	1231.37
1232.23	0.56	7-9	1232.23
1234.25	0.5	7-9	1234.25
1239.90	1	7-9	1239.90
1241.00	1.3	7-9	1241.00
1242.65	0.65	10	1242.65
1250.65	0.7	10	1250.65
1480.25	0.5	10-14	1480.25
1501.55	0.3	20	1501.55
2160.63	0.75	7-9	2160.63
2163.98	0.5	7-9	2163.98
2174.35	0.45	15	2174.35
2175.45	0.35	15	2175.45
2177.88	1.2	30-35	2177.88
2181.76	1.2	30-35	2181.76
2183.64	1.2	30-35	2183.64
2185.14	0.3	20	2185.14
2187.04	0.4	30-35	2187.04
2187.82	0.4	15	2187.82
2188.02	0.5	30-35	2188.02
2188.80	0.4	15-20	2188.80
2189.50	0.6	30-35	2189.50
2189.72	0.3	20	2189.72
2190.48	0.4	30-35	2190.48
2195.00	0.35	20	2195.00
2195.14	0.6	30-35	2195.14
2210.42	1	30-35	2210.42
2211.15	1	30-35	2211.15
2212.80	0.5	25	2212.80
2214.00	1.1	30-35	2214.00
2216.70	0.9	30-35	2216.70
2218.65	1	30-35	2218.65
2219.48	0.5	30	2219.48
2220.56	1	30-35	2220.56
2220.88	0.3	20	2220.88

Table 24: Microwindow list for N<sub>2</sub><sup>18</sup>O

Center Frequency (cm <sup>-1</sup> )	Microwindow Width (cm <sup>-1</sup> )	Lower Altitude (km)	Upper Altitude (km)
1223.67	0.3	5-7	15
1224.49	0.45	10	20
1226.99	0.45	12	20
1228.00	0.4	5	25
1231.38	0.45	5	25
1232.10	0.4	5	25
1232.82	0.6	5	25
1233.07	0.35	5-8	25
1233.88	0.4	5	25
1234.27	0.45	8	15
1234.70	0.45	5-8	25
1235.50	0.3	5-8	25
1480.25	0.5	10-14	22
1950.10	0.35	7-8	15
1950.70	0.5	15	34-45
2177.88	0.35	12	25
2178.90	0.4	12	25
2185.26	0.3	15	25
2192.83	0.26	15	20
2195.00	0.35	17-20	35
2195.98	0.3	20	35
2197.60	0.6	30	45
2200.48	0.3	25	35
2200.70	0.4	35	45
2201.70	0.6	30	45
2202.85	1.1	35	45
2203.20	0.4	17-20	35
2204.62	1.1	35	45
2205.06	0.3	20	35
2205.75	0.6	30	45
2206.67	0.5	30	45
2210.12	0.3	25	35
2210.98	0.3	17-20	35
2222.80	0.4	30	45
2224.96	0.4	20	45
2226.30	0.5	30	45
2229.83	0.35	20	35
2230.30	0.6	35	45
2333.63	0.35	25	35
2560.40	0.26	5	12

**VITA**

Eric Michael Buzan

Department of Chemistry and Biochemistry  
Old Dominion University  
Norfolk, VA, 23529

**Education**

August 2017 – Ph.D. Chemistry, Old Dominion University, Norfolk, VA  
May 2011 – B.S. Ocean and Earth Sciences, Old Dominion University, Norfolk, VA

**Publications**

- Buzan, E. M., Hargreaves, R. J. & Bernath, P. F. High resolution absorption cross sections for propylene in the 3  $\mu\text{m}$  region at high temperatures. *Mol. Astrophys.* 3–4, 16–20 (2016).
- Buzan, E. M., Beale, C. A., Boone, C. D. & Bernath, P. F. Global stratospheric measurements of the isotopologues of methane from the Atmospheric Chemistry Experiment Fourier transform spectrometer. *Atmos. Meas. Tech.* 9, 1095–1111 (2016).
- Beale, C. A., Buzan, E. M., Boone, C. D. & Bernath, P. F. Near-global distribution of CO isotopic fractionation in the Earth's atmosphere. *J. Mol. Spectrosc.* 323, 59–66 (2016).
- Hargreaves, R. J., Buzan, E. M., Dulick, M. & Bernath, P. F. High-resolution absorption cross sections of  $\text{C}_2\text{H}_6$  at elevated temperatures. *Mol. Astrophys.* 1, 20–25 (2015).